SIMULATION OF 3D WAFER SURFACE RECONSTRUCTION BY WAVEFRONT SENSING METHODS

By

NG YONG HAN

A dissertation submitted to the Department of Electrical and Electronic Engineering, Faculty of Engineering and Science,
Universiti Tunku Abdul Rahman,
in partial fulfillment of the requirements for the degree of
Master of Engineering Science

AUGUST 2013

ABSTRACT

SIMULATION OF 3D WAFER SURFACE RECONSTRUCTION BY WAVEFRONT SENSING METHODS

NG YONG HAN

Surface metrology is required in the process of manufacturing silicon wafers. One of the physical defects that affect the performance of a silicon wafer-based product is warping. Therefore, a non-destructive evaluation of the wafers is done before they are processed into final products, which are integrated circuits. The topologies of the top surface of a material can be measured by most surface metrology methods. An interferometer is capable of measuring both the top surface and the subsurfaces of a material, but it requires an expensive vibration-proof setup. Meanwhile, the ellipsometric and the picoseconds laser acoustics scanning methods do provide the thickness information of a multi-layered material. However, the surface topology of these methods is not acquired. On the other hand, the simulation of the behaviour of a laser pulse in a time-gated wavefront sensor has been done, but only in one dimension and by using algebraic method to compute the individual rays. In this work, the behaviour of the short laser pulse traversing within the material in the proposed system is simulated in Matlab in three dimensions, using vector-based raytracing algorithm and

analytical surfaces. The reflected subsurface wavefront which is obtained from the simulation is then reconstructed and the Singular Value Decomposition (SVD) is used to obtain its Zernike coefficients. It is known that the thickness, refractive index and the surfaces of a material do affect the levels of distortions in the reflected subsurface wavefront.

ACKNOWLEDGEMENTS

First of all, I would like to thank my supervisor, Dr. Chew Kuew Wai for his endless support and helpful guidance on this project. Also, I express my gratitude to Dr. Wang Xin, Dr. Tan Ching Seong, Dr. Lim Wee Keong, and Mr. Chai Tong Yuen for their assistance and discussions on the project. I am also indebted to Mr. Ong Chi Wei for providing me very useful advice on the general methods of wavefront reconstruction. On top of that my credit goes to Dr. Lee Jer Vui and Dr. Yong Thian Kok for their extra assistance and feedback on developing the project. Finally, my sincere thanks goes to my parents, my friends and my brother for their support and encouragement throughout my work.

APPROVAL SHEET

This dissertation entitled "**SIMULATION OF 3D WAFER SURFACE RECONSTRUCTION BY WAVEFRONT SENSING METHODS**" was prepared by NG YONG HAN and submitted as partial fulfillment of the requirement for the degree of Master of Engineering Science at Universiti Tunku Abdul Rahman.

Approved by:

____

(DR CHEW KUEW WAI)
Date:
Associate Professor
Department of Electrical and Electronic Engineering
Faculty of Engineering and Science
Universiti Tunku Abdul Rahman

____

(DR LEE JER VUI)
Date:
Co-supervisor
Department of Mechatronics and BioMedical Engineering
Faculty of Engineering and Science
Universiti Tunku Abdul Rahman

FACULTY OF ENGINEERING AND SCIENCE

UNIVERSITI TUNKU ABDUL RAHMAN

Date: _______________

SUBMISSION OF DISSERTATION

It is hereby certified that **NG YONG HAN** (ID No: **11UEM01666**) has completed this dissertation entitled "**SIMULATION OF 3D WAFER SURFACE RECONSTRUCTION BY WAVEFRONT SENSING METHODS**" under the supervision of **DR. CHEW KUEW WAI** from the Department of Electrical and Electronic Engineering, Faculty of Engineering and Science, and **DR. LEE JER VUI** from the Department of Mechatronics and BioMedical Engineering, Faculty of Engineering and Science.

I understand that the University will upload softcopy of my dissertation in pdf format into UTAR Institutional Repository, which may be made accessible to UTAR community and public.

Yours Truly,

____

NG YONG HAN

DECLARATION

I **NG YONG HAN** hereby declare that the project is based on my original work except for quotations and citations which have been duly acknowledged. I also declare that it has not been previously or concurrently submitted for any other degree at UTAR or other institutions.

NG YONG HAN

30 AUGUST 2013

TABLE OF CONTENTS

	Page
ABSTRACT	**ii**
ACKNOWLEDGMENTS	**iv**
APPROVAL SHEET	**v**
SUBMISSION OF THESIS	**vi**
DECLARATION	**vii**
TABLE OF CONTENTS	**viii**
LIST OF FIGURES	**xi**
LIST OF TABLES	**xvi**
LIST OF ABBREVIATIONS	**xvii**

CHAPTER

1	**INTRODUCTION**		**1**
	1.1	Background	1
	1.2	Problem Statements	5
	1.3	Objective of the Research	6
2	**LITERATURE REVIEW**		**7**
	2.1	Brief History of the Shack-Hartmann Wavefront Sensor	7
	2.2	General Mechanism of the Shack-Hartmann Wavefront Sensor	9
	2.3	General Methods of Wavefront Reconstruction	12
		2.3.1 Zonal Method	12
		2.3.2 Modal Method	14
	2.4	Methods of Surface Metrology	17
		2.4.1 Interferometry	17
		2.4.2 Optical Coherence Tomography (OCT)	19

2.4.3 Spectral Domain OCT: Fourier-Domain and Swept-Source OCT 23
2.4.4 Terahertz Time-Domain Reflectometry 25
2.4.5 Ellipsometry 29
2.4.6 Picosecond Laser Ultrasonics 31
2.5 Gated-Camera 34
2.5.1 Gated-Camera Wavefront Sensor 36

3 MATERIALS AND METHODS 38
3.1 Schematics of the Shack-Hartmann Gated-Camera Setup 38
3.2 Assumptions 40
3.3 Mechanisms of surface and subsurface detection 42
3.4 Simulation of Wavefront by Ray-Tracing (Two Interfaces) 47
3.5 Zernike Decomposition 52
3.5.1 Singular Value Decomposition (SVD) 56

4 RESULTS AND DISCUSSIONS 61
4.1 Identical surfaces (Z_5) with larger coefficients (0.0001) and varying distances 62
4.2 Identical surfaces (Z_5) with larger coefficients (0.0001) and varying refractive indexes 72
4.3 Identical surfaces (Z_5) with different coefficients for the bottom surface 79
4.4 Identical surfaces (Z_5) with both small coefficients (0.000001) and with varying distances 81
4.5 Identical surfaces (Z_5) with both small coefficients (0.000001) and varying refractive indexes 83

4.6 Identical surfaces (Z_5 + Z_7 + Z_8) with both small coefficients (0.000001), with varying distances between interfaces 85

4.7 Identical surfaces (Z_5 + Z_7 + Z_8) with both small coefficients (0.000001), fixed distance but with varying refractive indexes 92

4.8 Different surfaces and its combinations with small coefficients (0.000001) 94

5 CONCLUSIONS AND FURTHER WORK 100

6 REFERENCES 102

7 APPENDICES 113

LIST OF FIGURES

Figure		Page
2.1	Hartmann Test on an Optical Surface.	8
2.2	Behaviour of a Wavefront.	10
2.3	Cross-section of Shack-Hartmann sensor.	10
2.4	Southwell's method of approximating the phase of the wavefront.	13
2.5	A partial list of Zernike Polynomials.	16
2.6	Basic Optical Interferometry.	18
2.7	Optical Coherence Tomography (OCT) in measuring a tissue sample.	20
2.8	Time-Domain Optical Coherence Tomography. (TD-OCT)	21
2.9	Fourier/Spectral-Domain Optical Coherence Tomography.	23
2.10	Swept-Source OCT.	24
2.11	Basic Schematic of a THz-TDR system.	25
2.12	Thickness measurement using Terahertz Time-Domain Reflectometry.	26

2.13	Basic Schematic of a Tomographic Terahertz Imaging System.	27
2.14	Spectroscopic Ellipsometer.	30
2.15	Reflectance change with delay time.	32
2.16	The cross-section of the multilayered films during the test.	33
2.17	Gated camera setup with the delay and pulse generator systems.	35
3.1	Proposed gated-camera wavefront sensing system.	39
3.2	Capturing the wavefront reflected from the surface of the material.	43
3.3	Capturing the wavefront reflected from the subsurface of material.	44
3.4	Cross section of a material with a ray propagating within two interfaces.	48
3.5	Lines L1 and L2 are constructed across the interfaces to find the reflection and refraction points at point B and C.	51
3.6	Zernike decomposition of a surface/wavefront with only $-0.01Z_5$. The resultant chart shows only one peak, exactly at Z_5, with the value of -0.01.	60
4.1	Top and bottom surfaces are Z_5 with large coefficients (0.001) and distance between these surfaces is 0.1 units.	63

4.2	Top and bottom surfaces are Z5 with large coefficients (0.001) and distance between these surfaces are 0.01 units.	65
4.3	Top and bottom surfaces are Z5 with large coefficients (0.001) and distance between these surfaces are 0.001 units.	66
4.4	Top and bottom surfaces are Z5 with large coefficients (0.001) and distance between these surfaces are 0.0001 units.	67
4.5	Top and bottom surfaces are Z5 with large coefficients (0.001) and distance between these surfaces are $1x10^{-5}$ units.	68
4.6	Top and bottom surfaces are Z_5 with large coefficients (0.001) and distance between these surfaces are $1x10^{-6}$ units.	70
4.7	Top and bottom surfaces are Z5 with large coefficients (0.001), distance between the interfaces is fixed at $1x10^{-3}$ units and refractive index of the material is 1.33.	73
4.8	Top and bottom surfaces are Z5 with large coefficients (0.001), distance between the interfaces is fixed at $1x10^{-3}$ units and refractive index of the material is 1.55.	74
4.9	Top and bottom surfaces are Z5 with large coefficients (0.001), distance between the interfaces is fixed at $1x10^{-3}$ units and refractive index of the material is 1.67.	75

4.10	Top and bottom surfaces are Z5 with large coefficients (0.001), distance between the interfaces is fixed at 1×10^{-3} units and refractive index of the material is 2.33.	76
4.11	Top and bottom surfaces are Z5 with large coefficients (0.001), distance between the interfaces is fixed at 1×10^{-3} units and refractive index of the material is 2.67.	77
4.12	Top and bottom surfaces are Z5 with large coefficients (0.001), distance between the interfaces is fixed at 1×10^{-3} units and refractive index of the material is 3.00.	78
4.13	Top and bottom surfaces are Z5 with top surface fixed to 0.000001, while the bottom surface is 0.000002. The refractive index is fixed to 1.55 and the distance is 0.001.	80
4.14	Top and bottom surfaces are Z_5 with coefficients of 0.000001. The refractive index is 1.55 and the distance between the surfaces is 0.1 units.	82
4.15	Both of the surfaces are Z_5 and distance between the surfaces is 1×10^{-3}. The change of refractive indexes does not affect the reflected wavefront.	84
4.16	Both of the surfaces are $Z_5 + Z_7 + Z_8$ and distance between the surfaces is 1×10^{-1}.	86
4.17	Both of the surfaces are $Z_5 + Z_7 + Z_8$ and distance between the surfaces is 1×10^{-2}.	87
4.18	Both of the surfaces are $Z_5 + Z_7 + Z_8$ and distance between the surfaces is 1×10^{-3}.	88

4.19 Both of the surfaces are $Z_5 + Z_7 + Z_8$ and distance between the surfaces is $1x10^{-4}$. 89

4.20 Both of the surfaces are $Z_5 + Z_7 + Z_8$ and distance between the surfaces is $1x10^{-5}$. 90

4.21 Both of the surfaces are $Z_5 + Z_7 + Z_8$ and distance between the surfaces is $1x10^{-6}$. 91

4.22 Both of the surfaces are $Z_5 + Z_7 + Z_8$ and distance between the surfaces is $1x10^{-3}$. The change of refractive indexes does not affect the reflected wavefront. 93

4.23 Top surface is Z_3 while the bottom surface is Z_6. The refractive index is 1.55 and the distance between the surfaces is $1x10^{-3}$ units. 96

4.24 Top surface is Z_6 while the bottom surface is Z_{10}. The refractive index is 1.55 and the distance between the surfaces is $1x10^{-3}$ units. 97

4.25 Top and bottom surfaces are $Z_5 + Z_7$ with coefficients of 0.000001. The refractive index is 1.55 and the distance between the surfaces is $1x10^{-3}$ units. 98

4.26 Top and bottom surfaces are randomly generated surfaces. Distance between the surfaces is $1x10^{-3}$ units and the refractive index is 1.55. 99

LIST OF TABLES

Table		Page
3.1	List of first 10 Zernike Polynomials. The Zernike Polynomials in the figure is in Cartesian form and with derivatives of the polynomials in respect of X and Y coordinates	53
4.1	The eight different parameters which are used in the simulation	61

LIST OF ABBREVIATIONS

CCD	Charged coupled device
d_{PC}	Distance between prism and gated camera
d_{LP}	Distance between pulsed laser module and prism
d_{MMS}	Distance between top surface and bottom surface of the material
d_{PM}	Distance between pulsed laser module and material
FD-OCT	Fourier Domain Optical Coherence Tomography
OCT	Optical Coherence Tomography
SD-OCT	Spectral-Domain Optical Coherence Tomography
SH	Shack-Hartmann
SS-OCT	Swept-Source Optical Coherence Tomography
SVD	Singular Value Decomposition
TD-OCT	Time Domain Optical Coherence Tomography
THz-TDR	Terahertz Time-Domain Reflectometry

CHAPTER 1

INTRODUCTION

1.1 Background

It is known that many material failures such as fatigue, cracks, wears, erosion and others are due to the poor condition of the surface (Blunt and Jiang, 2003). Surface measurement is important for controlling surface textures such as microlens arrays, photo-voltaics, microfluidic channels and biosensors (Leach, 2010).

In semiconductor wafer processing, surface measurement is important as it is a part of a quality control procedure in an integrated circuit or VLSI manufacturing. A defect on the wafer surface is detrimental to the performance of an electronic system (Armitage and Wu, 2006). To prevent semiconductor wafer with defects into further processing and manufacturing, a non-destructive inspection of the wafer surface must be done beforehand. Semiconductor wafers with an acceptable quality will be sent to production of VLSI while the defective ones will be rejected. Subsurface damage in silicon wafers will cause integrity problems in the gate oxide layers during manufacturing (Ogita et al., 1998). On smaller silicon-based semiconductors, surface roughness affects the mobility of the electrons in the material (Nemoto et al., 2007).

For wafer bonding processes, surface morphology is extremely important as the level of roughness on the wafer affects the bonding (Tseng and Park, 2006). Higher roughness on the wafer will contribute to a total small area of contact, therefore causing the bonding to be very ineffective (Gui, Elwenspoek, Tas and Gardenier, 1999). In worst case scenario, poor wafer surface quality will have a higher chance of failed bonding.

Metrology of wafer and its surface is usually performed by certain types of microscopy, which are the Transmission Electron Microscopy (TEM), Scanning Electron Microscopy (SEM) and Atomic Force Microscopy (AFM). Samples must be prepared and deployed prior to evaluation by TEM and SEM systems, in which the samples could be destroyed in this process. (Williams and Carter, 2009; Kang et al., 2010) Partially non-destructive measurement is done by Atomic-Force Microscopy (AFM) on semiconductor wafers for defect analysis and surface roughness evaluation. The forces between the tip of the miniaturized cantilever and the atoms on the surface are measured in the test (Hattori, 1998). However, the tip of the cantilever can be known to damage certain surfaces, despite being ‘non-contact’ (Blunt, 2006).

Most commercially available interferometers have the capability to measure wafer or thin film surface roughness on the first interface. (Jansen, Haitjema and Shellekens, 2004; Hall, Tricard and Dumas, 2007; Tien, Lyu and

Jyu, 2008; Chen and Du, 2009) However, not much is done to measure the roughness of the sub-surface. On bonded multi-layered wafers, voids are being located using the infrared interferometer (Podjue et al., 2010).

Meanwhile, Optical Coherence Tomography (OCT), which is another type of interferometer, can measure roughness up to a few interfaces but it is for evaluation of multilayered cellular samples (Huang et al., 1991). Wafer inspection using OCT are mainly focused on locating defects and not measuring the surface roughness (Kwon, Joo and Kim, 2007).

The ellipsometer detects up to 4 layers but optical models of the respective layers must be provided prior to the testing. Again, there are no topological inspections in these ellipsometric tests (Fujiwara, 2005).

Similarly, picosecond laser acoustic scanning provides thickness information on a particular point of a multilayered material, but there are no surface inspections. Most evaluations are only for measuring thickness variations on a multilayered material (Wright, 1995). Terahertz radiation allows the inspections of thickness variations and oil paintings but there is no surface evaluation done on surfaces of any other materials (Jackson, 2008).

An experimental Gated-Camera system using the Shack-Hartmann sensor to evaluate the surface of the interfaces within the semiconductor wafer is proposed. Compared to the interferometric method, there will be no extra moving parts, diffraction gratings and this method is vibration-invariant (Shaw-McMinn, 2006). In this work, a simulation of wavefront traversing between the interfaces within the material is developed.

1.2 Problem Statements

Current methods of sub-surface inspection of silicon wafers are limited. An interferometer is capable of doing such inspections, but a costly vibration-invariant setup and complicated wavefront reconstruction algorithm is required for more accurate results (Malacara, 2007). Meanwhile, the ellipsometer and the picosecond laser acoustic scanner have the capability of detecting subsurfaces but these are for thickness measurement and not for surface measurement. Simulation and reconstruction of the time-gated subsurface wavefront in three dimensions is not available and only simulation of the wavefront traversing the interfaces is done on a long period of time (Chu and Chaudhuri, 1995). Also, not much is done on the analysis of the reflected subsurface wavefront. The amount of distortions that are present in the wavefront in three dimensions are not currently known.

1.3 Objectives of the Research

The main objective of this project is to simulate the reflection and refraction of the short laser pulse which is traversing between two interfaces in the gated wavefront sensor setup by using a vector-based raytracing algorithm. The gated wavefront sensor emits and captures the short laser pulse which is reflected from a material surface after a specified amount of time is passed. Afterwards, the slope data from the reflected subsurface is obtained through the raytracing process and it is reconstructed into a wavefront. Different parameters in the simulation such as the material thickness, refractive indexes, size of gradients on the surface and the types of surface are explored. Finally, the distortions of the wavefront is analyzed by using Zernike Decomposition method.

CHAPTER 2

LITERATURE REVIEW

2.1 Brief History of the Shack-Hartmann Wavefront Sensor

Johannes Hartmann created the wavefront sensor while he was working with a telescope in Potsdam, Germany. The images produced by the telescope were of poor quality and he had suspected that the one of the optical parts of the telescope contributed to the problem. So, he made a hole array on the aperture of the telescope, as illustrated in Figure 2.1 (Hartmann, 1904). With his diagnostic method, he was able to know which lens is of good or inferior quality, according to the images formed by the array. Finally, he fixed the telescope and a clearer and meaningful image is formed, facilitating the research (Kuria et al., 2012; Hartmann, 1904; Malacara, 2007).

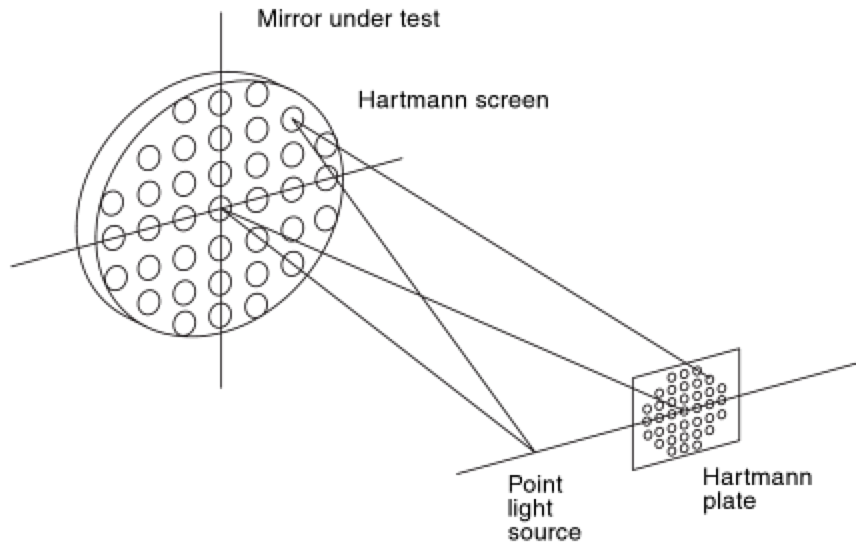

Figure 2.1: **Hartmann Test on an Optical Surface** (Malacara, 2007).

In the late 1960s, the Shack-Hartmann sensor was developed to solve two problems which are: blurry and low-intensity spots. The improvement over the original Hartmann sensor is the lenslet array which replaces the hole array, forming clearer and readable spots. The resultant spots are mapped into the respective grids and each spot is measured through centroiding method to obtain the discrete slope points on a wavefront. Combined with adaptive optics, the sensor is widely used in astronomical applications (Platt, 2001). Later in the early 1990s, this method is also used in measuring aberrations and topography on the cornea. With this method, the surface of the cornea can be corrected through refractive surgery (Schwiegerling and Neal; Neal; Barbosa-Mejia and Malacara-Hernandez, 2001; J., Rao and Rao, 2008).

The usage of this sensor is then extended into metrological applications. Measurements of foil optic surfaces are done with the help of the sensor and the results will determine if the surface meets the particular requirement or not (Forest et al., 2003).

For measuring the surface of the wafer using the wavefront sensor, an instrument named Columbus has been designed. In this method, the reflection of the fiber-coupled beam is captured by the CCD through the sensor. The individual array of dots alongside with its deviation from the centroids are then calculated and approximated to form a surface of the wafer in the computer. This method is vibration-invariant and the results produced by Columbus are comparable to that of the NIST XCALIBIR interferometer (Raymond et al, 2002).

2.2 General Mechanism of the Shack-Hartmann Wavefront Sensor

A wavefront is a collection of individual light rays from a point object, which its surface is actually a complete picture from that particular point (Sagar, 1995; Ghatak, 1995; Yanoff and Duker, 2009), as shown in Figure 2.2. The surface of the wavefront is altered by reflection and refraction. When the wavefront enters the sensor, it is broken into a discrete array of beams which are then captured by the CCD sensor as shown in Figure 2.3. The alignment of the dots (focal spots) represents the individual discrete slopes of the wavefront.

A uniform, planar wavefront forms a regularly spaced grid of spots on the sensor while a distorted, aberrated wavefront forms displaced spots on the sensor.

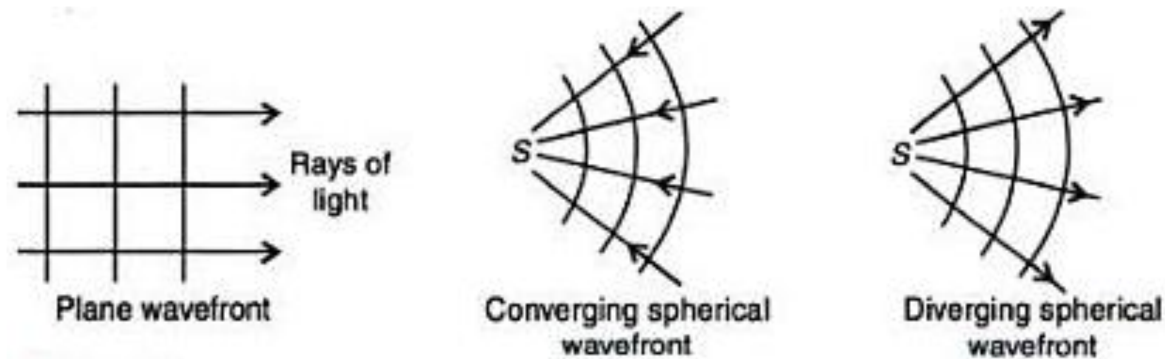

Figure 2.2: **Behaviour of a wavefront** (Sagar, 1996).

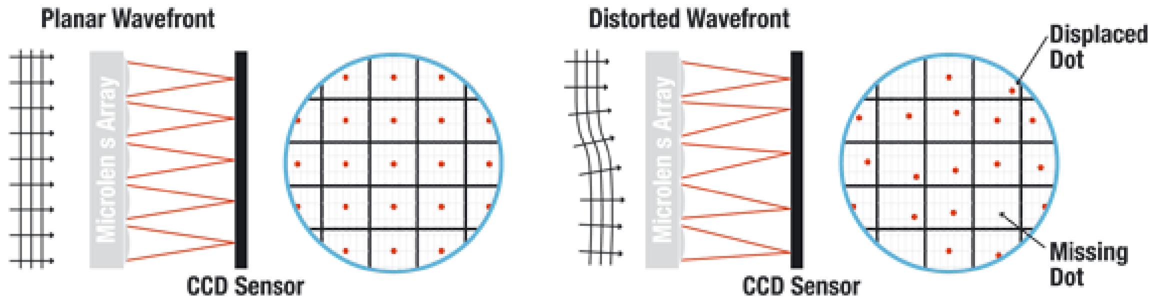

Figure 2.3: **Cross-section of Shack-Hartmann sensor** (Thorlabs, 2013).

The centre of each of the focal points is calculated by centroiding method. The coordinate of the centroid of the focal point is calculated using the general centroid formula (Neal et al., 2002; Török and Kao, 2003):

$$x_{c,k} = \frac{\sum_{i,j\,\in AOI_k} x_{i,j} I_{i,j}}{\sum_{i,j\,\in AOI_k} I_{i,j}} \; and \; y_{c,k} = \frac{\sum_{i,j\,\in AOI_k} y_{i,j} I_{i,j}}{\sum_{i,j\,\in AOI_k} I_{i,j}}$$

where $x_{c,k}$ and $y_{c,k}$ is the coordinate of the centroid of the spot, k is the lenslet number, and the $I_{i,j}$ is the pixel intensities in the lenslet.

Each of the positions of the centroid in the respective lenslet k represents the slope of the particular point on the wavefront. The slopes are only determined by using references, which are coordinates of centres of the lenslets. Therefore, using the actual and reference positions of each lenslet K with the distance between the lens and the detector L_H, the slope of the individual point on a wavefront is obtained. The coordinates of the spots formed by the wavefront tested are x_c, y_c and x_r, y_r are coordinates of the reference spots, as shown in the following equation:

$$\begin{pmatrix} \partial w / \partial x \\ \partial w / \partial y \end{pmatrix}_k = \begin{pmatrix} \beta_x \\ \beta_y \end{pmatrix}_k \approx \frac{1}{L_H} \begin{pmatrix} x_c - x_r \\ y_c - y_r \end{pmatrix}_k$$

Once the individual slope points have been obtained, these are interpolated to form a surface. Various methods are used to form the mentioned surface which will be discussed later in the review.

2.3 General Methods of Wavefront Reconstruction

2.3.1 Zonal Method

Using the discrete slope point obtained in each subapeture/lenslet in the Shack-Hartmann sensor, the wavefront is reconstructed by mathematical integration (Campbell and Greenaway, 2006). Southwell had devised an estimation model of the slope points as shown in Figure 2.4, which is suitable for the results obtained from the Shack-Hartmann sensor (Southwell, 1980). Afterwards, the points are then interpolated using Least Squares Method. On the *x*-direction, the phase is represented in this polynomial:

$$\phi = c_0 + c_1 x + c_2 x^2$$

and differentiating the phase, the slope is $S^x = c_1 + 2c_2 x$.

From the Shack-Hartmann grids, the slopes for the *x*-directions and *y*-directions are:

$$\frac{\left(S^x_{i+1,j} + S^x_{ij}\right)}{2} = \frac{\left(\phi_{i+1,j} - \phi_{ij}\right)}{h} \quad i = 1, N-1, j = 1, N$$

$$\frac{\left(S^y_{i+1,j} + S^y_{ij}\right)}{2} = \frac{\left(\phi_{i,j+1} - \phi_{ij}\right)}{h} \quad i = 1, N, j = 1, N-1$$

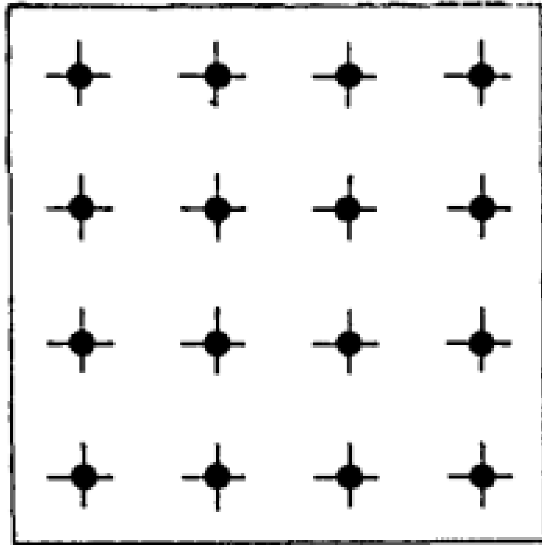

Figure 2.4: **Southwell's method of approximating the phase of the wavefront.** (Southwell, 1980)

2.3.2 Modal Method

The reconstruction of the wavefront from the discrete slope points is also achieved by using modal method. Through the slope data obtained from the Shack-Hartmann sensor, the wavefront is decomposed into a summation of individual polynomials. Each of the polynomial is multiplied by its coefficient (Dai, 2008).

With the polynomials, the wavefront can be described as:

$$\frac{\partial w(x,y)}{\partial x} = \sum_{n} C_n \frac{\partial P_n(x,y)}{\partial x}$$

$$\frac{\partial w(x,y)}{\partial y} = \sum_{n} C_n \frac{\partial P_n(x,y)}{\partial y}$$

Combining the differentiated wavefronts in the respect of x and y for each point into a matrix, the slope matrix is formed. On the right side of the aforementioned equations, combining the sums of n differentiated polynomials in respect of x and y, another matrix is formed. By solving the matrix for the coefficients, the wavefront surface is successfully decomposed into n number of coefficients. The coefficients of the polynomials are used to reconstruct the wavefront (Dai, 1994).

A commonly used modal method is the Zernike decomposition method, which is invented by Frits Zernike. Each Zernike polynomial is unique and closely describe common type aberrations such as defocus, astigmatism and coma (Zernike, 1934). The degrees of such aberrations increase when the number of modes becomes higher.

$$\frac{\partial w(x,y)}{\partial x} = \sum_{n} C_n \frac{\partial Z_n(x,y)}{\partial x}$$

$$\frac{\partial w(x,y)}{\partial y} = \sum_{n} C_n \frac{\partial Z_n(x,y)}{\partial y}$$

The Zernike polynomials are often used because these closely describe the optical aberrations such as defocus, astigmatism and coma (Teare and Restaino, 2006). A partial list of the polynomials are as shown in Figure 2.5. Solving for the coefficients by using Least Squares Method, the magnitude of the coefficients are obtained.

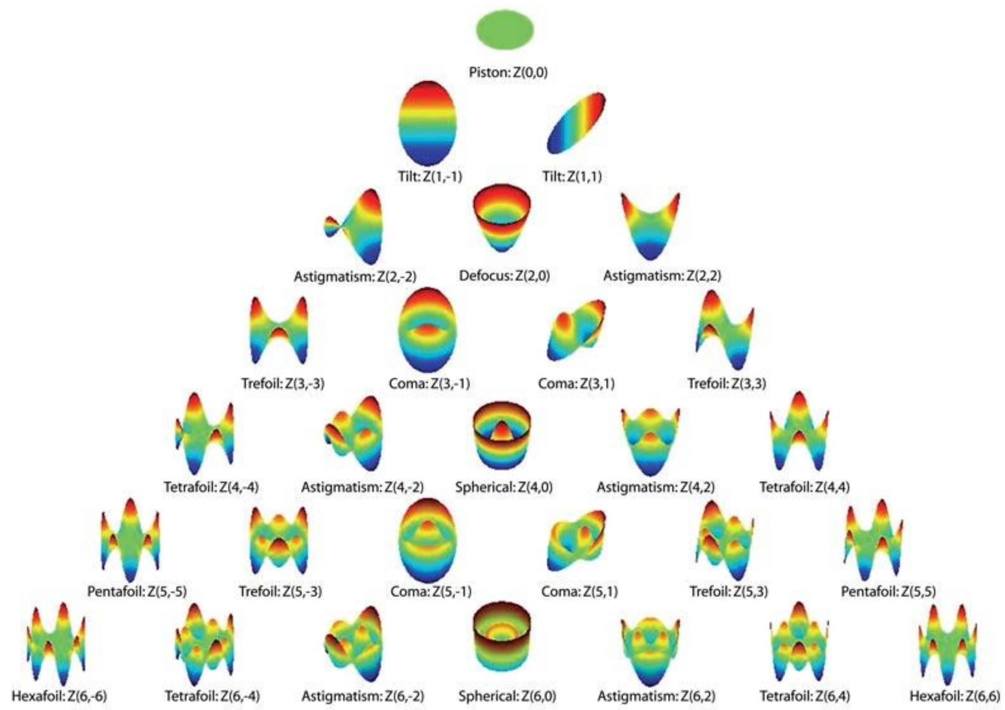

Figure 2.5: A partial list of Zernike Polynomials (Shaw-McMinn, 2006).

2.4 Methods of Surface Metrology

2.4.1 Interferometry

Light is also known to be propagating electromagnetic waves. The superposition of these waves causes interference. The difference of the optical path difference between two materials causes this phenomenon, and as a result, a reflected pattern of light is formed. A study on these patterns or fringes, gives information on the distance between the two materials mentioned. The measurement of optical interferences is known as interferometry (Hariharan, 2007). A diagram of a general interferometer is as shown in Figure 2.6.

Meanwhile, wafer roughness is successfully measured using White-Light Interferometry technique, and the results are comparable to the Atomic-Force Microscopy. Also, there will be less time involved in scanning due to the wider coverage of surface area (Blunt, 2006). Thickness variations on front and back parts of a wafer are also evaluated using another form of interferometry, which uses infrared light source (Schmitz, Davies and Evans, 2003).

Vibration-invariant interferometer for measuring surface roughness is built by using the lateral-shearing interferometer, and preliminary results of the wafer surface area are obtained (Liu and Gao, 2001). However, there are no comparisons of results between the other interferometers.

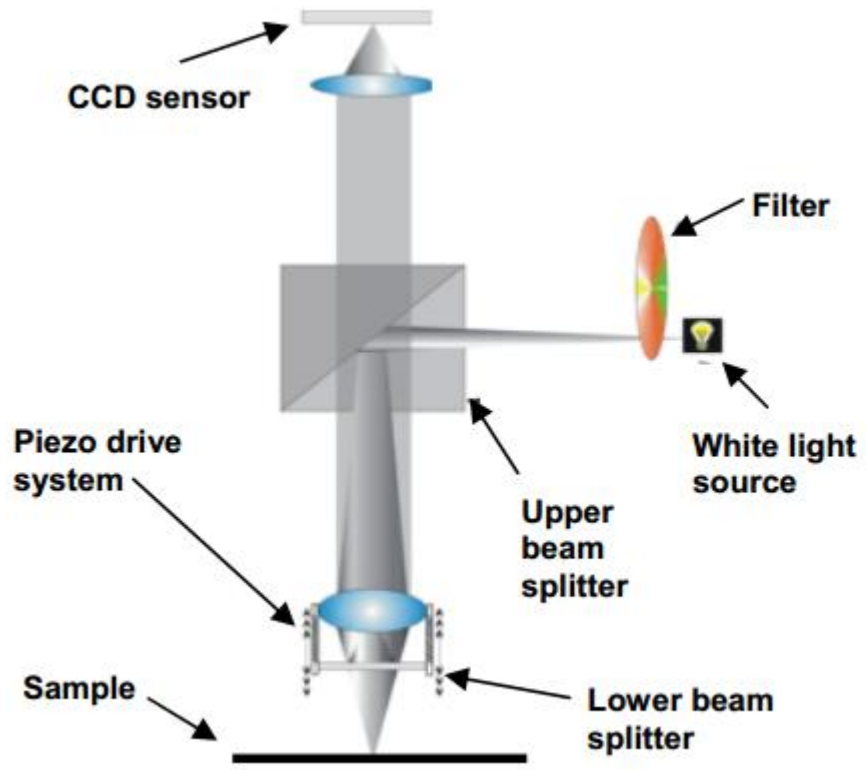

Figure 2.6: **Basic Optical Interferometry** (Blunt, 2006).

2.4.2 Optical Coherence Tomography (OCT)

A combination of interferometry and low-coherence light allows visualization of cross-sectional and tomographic imaging in biological systems (Huang et al., 1991). Retinal layers and blood vessels are mainly examined in the OCT and this provides a better picture of the stratification compared to the ultrasound method (Drexler and Fujimoto, 2008). A few common types of the OCT is discussed too in the literature (Schmitt, 1999; Choma, Hsu and Izatt, 2005; Drexler and Fujimoto, 2008), which are TD-OCT (Time-domain OCT) and SD-OCT (Spectral-Domain OCT). There are two main types of Spectral-Domain OCT which are the FD-OCT (Fourier-domain OCT) and SS-OCT (Swept-Source OCT).

Instead of measuring the time and intensity where the light rays are scattered and returned to the CCD sensor, the OCT measures the interference signals formed. In Figure 2.7, the OCT picks up scattered light which is within the focus, and any other scattered light outside of the focus is rejected. Therefore, a clearer and much accurate picture of within the cell layers is produced (Brezinski, 2006; Innovation, 2011).

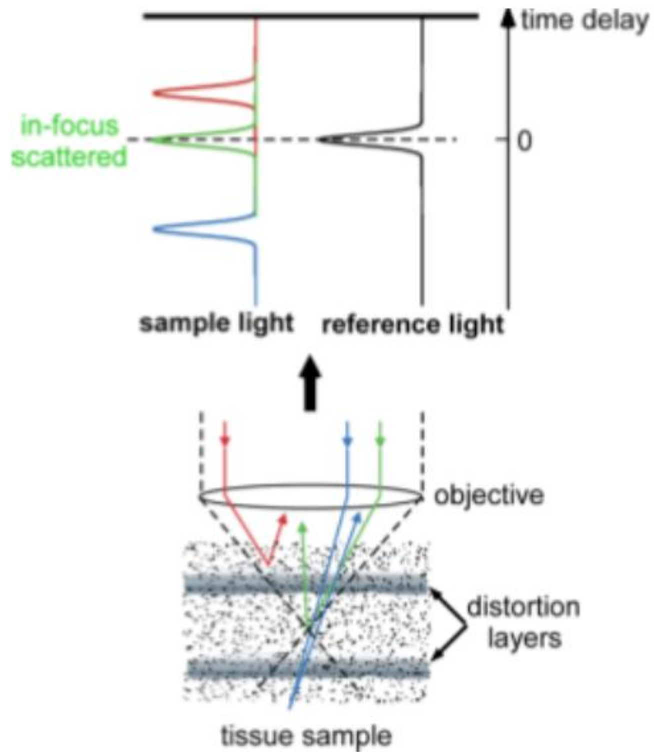

Figure 2.7: **Optical Coherence Tomography (OCT) in measuring a tissue sample** (Innovation, 2011).

In TD-OCT, the reflected light captured by the CCD in the form of amplitude pulses is correlated with the time taken for the light to travel between the interfaces to obtain the layer information, as shown in Figure 2.8. The reference mirror must move constantly to obtain the interference signal for the measurement of these layers.

However, due to the nature of the mechanical moving parts, acquisition time is much slower (Fercher, 2003). The TD-OCT is mainly used in ophthalmic imaging and research (Fercher, 2003; Hermann et al., 2004; Drexler and Fujimoto, 2008). Recently, there are studies conducted to examine silicon integrated circuits by using the technique (Serrels et al., 2010). The apparatus for evaluating the surface of the circuit is a modified TD-OCT. In the paper, only a cross section of two to three interfaces is evaluated. As the specimen is a circuit, it contains metal parts inside alongside with the silicon.

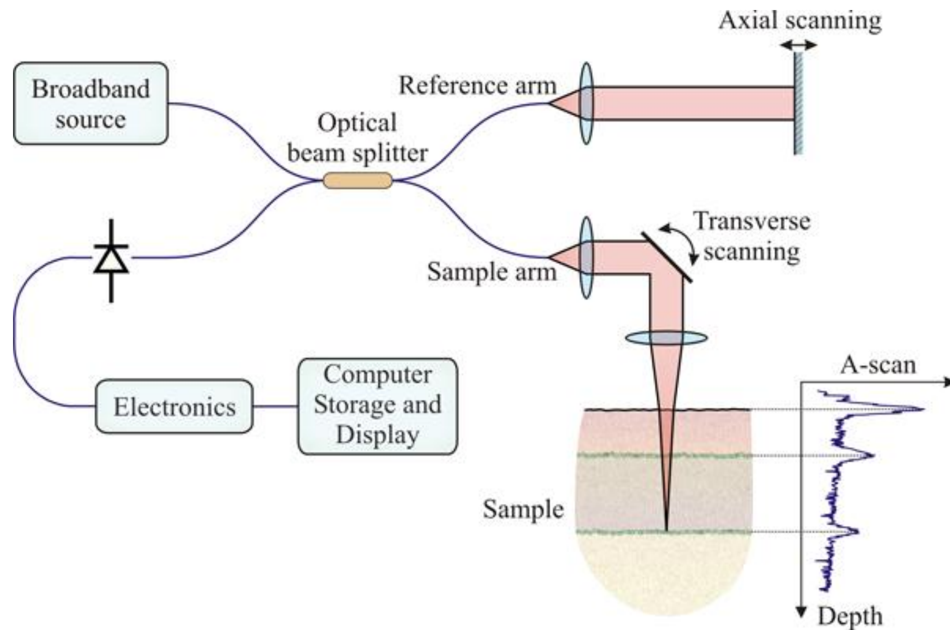

Figure 2.8: **Time-Domain Optical Coherence Tomography (TD-OCT)** (Sampson, 2011).

The test results are promising and it provides robust surface flatness detection with low numerical aperture of the objective lens used. A combination of Shack-Hartmann sensor and Time-Domain OCT is used to obtain depth-resolved wavefront information. A clear and a more enhanced signal is also captured from this method. Plus, unwanted reflections from the Shack-Hartmann sensor can be removed as well (Tuohy and Podoleanu, 2010; Wang and Podoleanu, 2011). However, these methods are only effective on low-scattering samples. Highly scattering samples such as rat brain cells are analyzed using a Linnik Interferometer, but without using the Shack-Hartmann sensor (Wang et al., 2012). Meanwhile, depth-resolved Shack-Hartmann wavefront aberrations can be achieved by combining the sensor with the OCT system. Both the Time and Spectral Domain OCTs are tested with the sensor too. Stray reflections and noise are mostly removed through this method. Unfortunately, there are no discussions or plans on testing the system with a non-organic specimen, such as silicon wafer or any other thin films (Tuohy and Podoleanu, 2010).

2.4.3 Spectral Domain OCT: Fourier-Domain and Swept-Source OCT

Another method which does not involve moving reference mirrors are the FD-OCT and SS-OCT, where only the frequency components of the reflections are analyzed.

On the FD-OCT as shown in Figure 2.9, the CCD is coupled with a diffraction grating to obtain Fourier coefficients from the reflected lights. In the SS-OCT as shown in Figure 2.10, the light source is replaced by a tunable wavelength light source (Chang et al, 2011; Gora et al., 2009). Both of these systems provide a significantly faster scan times than the TD-OCT because no moving parts are present. Plus, the Spectral-Domain OCT has a better Signal-to-Noise Ratio and sensitivity compared to the Time-Domain OCT (Leitgeb et al., 2003; Chang et al., 2011; Yaqoob et al., 2005).

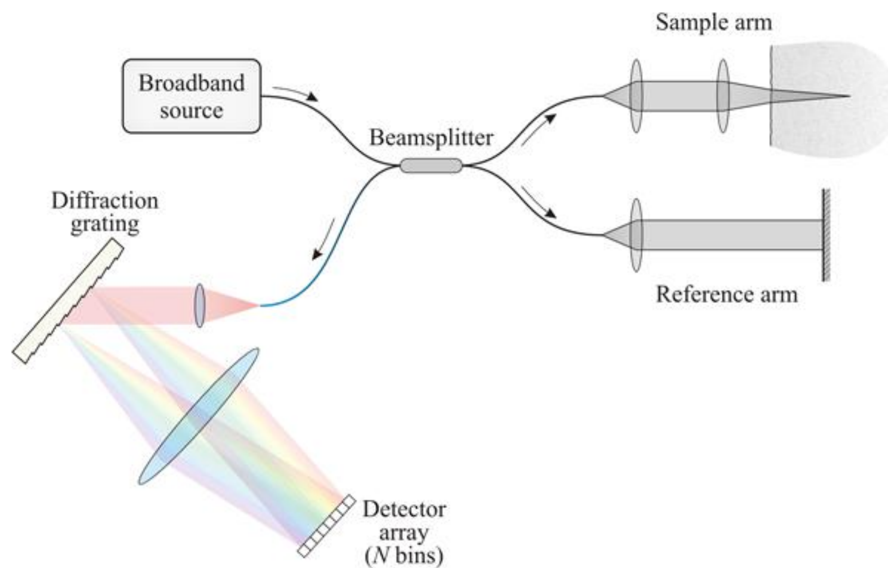

Figure 2.9: **Fourier/Spectral-Domain Optical Coherence Tomography** (Sampson, 2011).

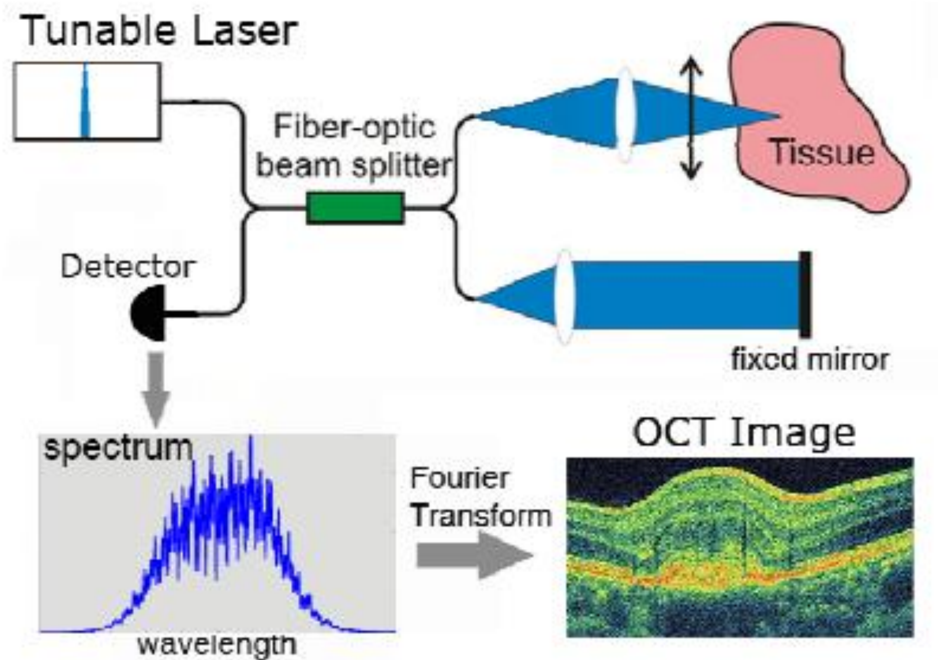

Figure 2.10: **Swept-Source OCT** (Yurtsever and Baets, 2008).

Apart from tissue analysis, the function of the OCT is also extended into metrology. One of them is the quality evaluation of the contact lens. Using the Spectral Domain OCT, thickness information of the contact lens are obtained and the results are almost identical to the cross-sectional measurements of the contact lens. When combined with industrial automation, there will be more improvements in the contact lens manufacturing (Davidson and Barton, 2010). Non-destructive analysis of embedded microchannels are done using OCT as well. Geometrical measurements and features are successfully collected from the OCT images (Su et al., 2012). Measuring of refractive index and changes of refractive index in a surface is done too by using the FD-OCT.

From this method, the properties of drying varnish on a surface are known immediately, without involving complex microscopy and mechanical profilometry (Lawman and Liang, 2009).

2.4.4 Terahertz Time-Domain Reflectometry

The basic schematic of a Terahertz Time-Domain Reflectometer is as shown in Figure 2.11. In this method, short terahertz pulses are emitted towards a material and the time taken for the reflections to be captured are measured, as shown in Figure 2.12. This gives information on the thickness and the depth of a material.

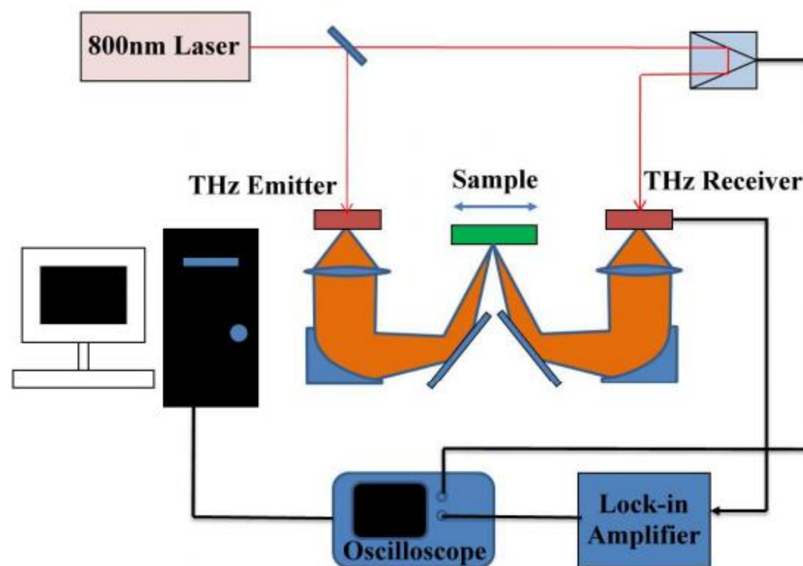

Figure 2.11: **Basic Schematic of a THz-TDR system** (Chen et al., 2010).

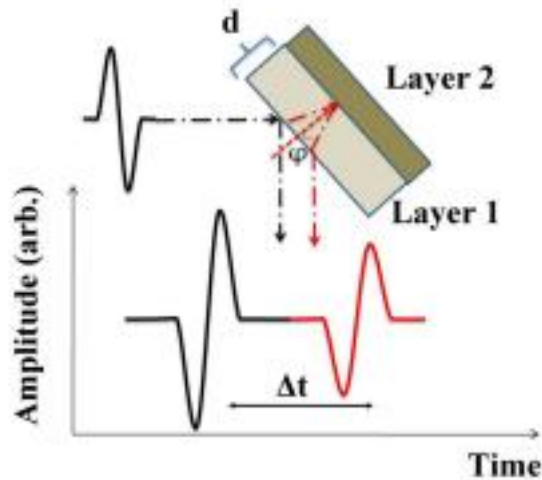

Figure 2.12: **Thickness measurement using Terahertz Time-Domain Reflectometry** (Chen et al., 2010).

When the terahertz pulse impinges the material surface in the figure, reflections of the pulse from the respective interfaces occurs after a time period (Chen, Lee, Pollock and Whitaker, 2010; Mittleman, Jacobsen and Nuss, 1996). *A priori* information of thickness is required if the refractive index of the material is to be determined, and vice versa. The time delay between the pulses can be calculated by the formula:

$$\Delta t = \frac{2n_g d}{c \cos \phi}$$

where Δt is time delay, n_g is the material's refractive index, d is the thickness of the material (or the distance between two interfaces) and ϕ is the reflection angle of the material.

Similarly, tomographic information of a material can be done using THz-TDR too. A general block diagram of a tomographic THz-TDR is as shown in Figure 2.13. The reflections of an object sample of an aluminum block with a hole is taken at different angles, and then reconstructed using filtered back-projection algorithm (Pearce et al., 2005; Withayachumnankul et al., 2007). Due to the highly reflective nature of the aluminum, only the outlines of the block are captured and the hole is not visible.

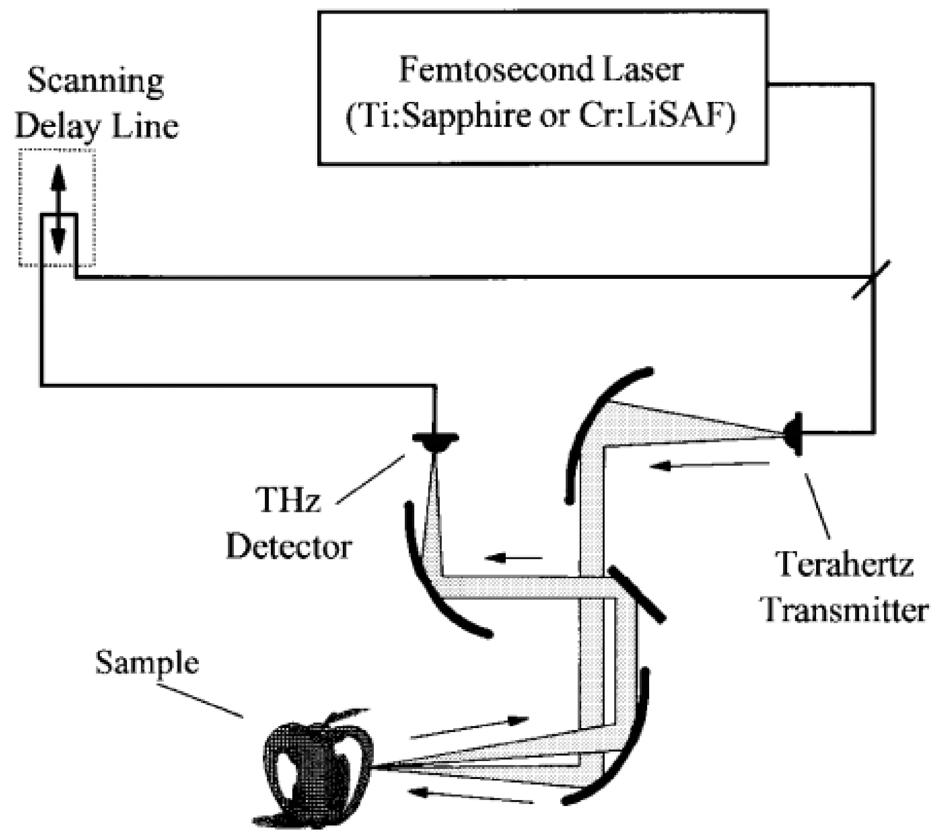

Figure 2.13: **Basic Schematic of a Tomographic Terahertz Imaging System** (Mittleman et al., 1996).

Non-destructive inspections on thermal barrier coatings are done using Terahertz Time-Domain Reflectometry. The reflection times and amplitudes vary on coatings in different conditions. Also, the thickness of these coatings calculated is comparable to the measurements from the SEM microscope (Chen et al., 2010). Non-invasive tree-ring analysis can be done too on the Terahertz Time-Domain Reflectometry. Preliminary results had shown that the outlines of the tree-rings are clear and resolvable (Jackson et al., 2009; Jackson, 2008). Using the same method, Egyptian artifacts are examined in a non-destructive manner. Multilayered papyrus is examined with this method and ink marks can be clearly seen without physically unrolling the papers (Labaune et al., 2010). Also, fabric layers of Egyptian mummies are probed using the imaging method and this can be a complement for X-ray and CT imaging (Fukunaga et al., 2011). Frescos which are obstructed by another painting is successfully examined in this method as well. However, more image processing methods must be involved for a complete image extraction (Jackson, 2008).

2.4.5 Ellipsometry

In the ellipsometric method, the polarization of light reflected from material surface is measured. The amplitude ratio and phase difference between p- and s-polarized light waves are obtained from the reflection and measured. Surfaces of thin films, polymer films, organic layers and coatings are evaluated through this method. However, the surface roughness of surface tested must be small and it has to be measured at an oblique angle, as shown in Figure 2.14 (Fujiwara, 2005). Rougher surfaces are evaluated with a modified ellipsometer with a space filter (Huang et al., 2008).

Also, complex algorithms are needed to estimate the layer's roughness of the material, and *a priori* information of the material such as thickness of the layers and respective refractive indexes must be keyed into the system before testing. On real-time monitoring, optimizations such as Global Error Minimization can be done without knowledge of the dielectric function and the sample structure.

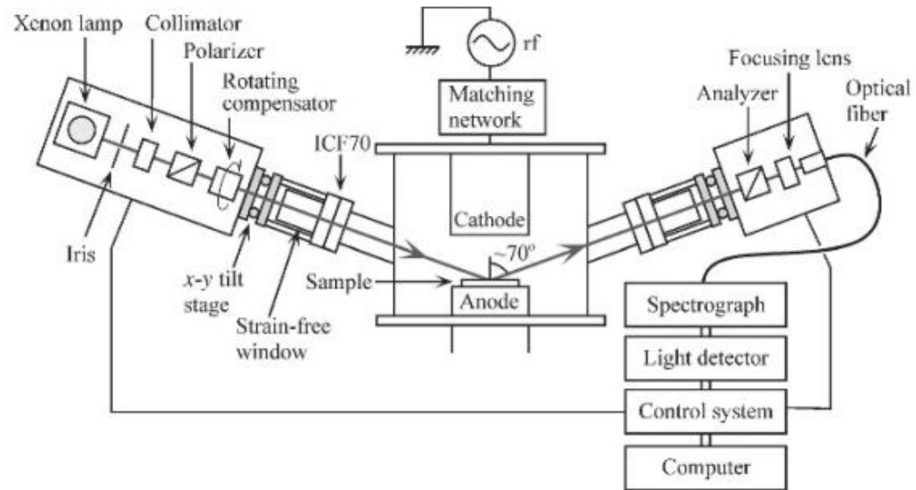

Figure 2.14: **Spectroscopic Ellipsometer** (Fujiwara, 2005).

So far, the ellipsometric method mentioned has the capability of measuring interfaces belonging to the second and third layer, but with preliminary information of the material. Optical models of the respective layers must be formed first, and then optimization is done to get the correct thickness measurements for these layers. Characterisations of thin-film layers in solar cell modules are successfully done in high precision by the usage and development of such optical models (Fujiwara et al., 2012). A focused-beam is used in (Neuschaefer-Rube et al., 2003) and an ellipsometric measurement is done on tilted bulk layers. However, the article did not cover thin-film systems and the authors will perform further research on the topic. Most of the ellipsometric tests are confined to surface characterization and determination of refractive index of the tested material. On top of that, multilayer material thickness is measured too.

2.4.6 Picosecond Laser Ultrasonics

This method measures the acoustic pulses that travel within the interfaces in a material upon absorbing of ultrashort laser pulses. The emitted probe beam picks up the pulses that have been reflected from the interfaces in the material, as shown in Figure 2.14. In Figure 2.15, reflectance changes with time determine the material thickness. The theoretical calculations of the reflectance change in the multilayered material agree well with the experimental results obtained from the method (Wright and Hyoguchi, 1991; Wright, 1995; Matsuda, 2002). However, this method is only used for thickness measurement of multilayered thin films and no topographical/surface information of the material is analyzed. The analytical model of the acoustic reflectance change of a multilayered material is also conceived (Matsuda and Wright, 2004). Meanwhile, wide planar sound waves are used in the evaluation of a sample nanostructure with trenches. With the method, the depths of the trenches in the nanostructure are estimated. Also, minor shape variations of the trenches can be also successfully detected as well. More studies are performed to develop the technique to evaluate sub-100 nm nanostructures (Grimsley et al., 2008).

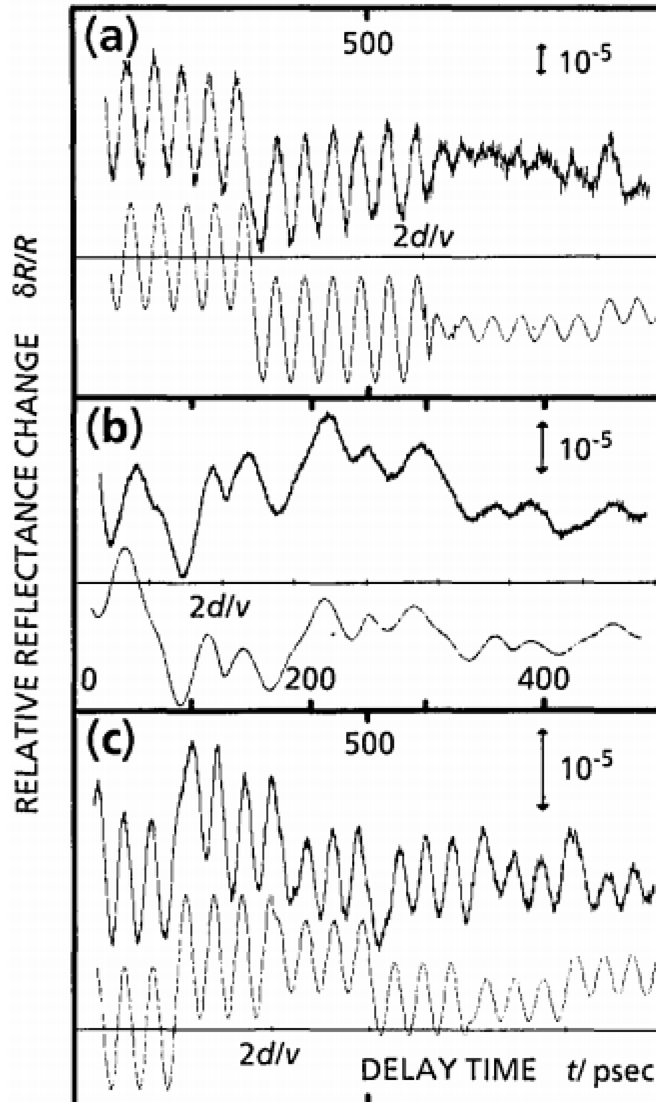

Figure 2.15: **Reflectance change with delay time.**
(a) SiO2 with thickness of 1600nm with another Ge layer, (b) SiO2 with thickness of 250nm with another Cr layer, (c) SiO2 with thickness of 900nm with another Cr layer. The upper curves of (a), (b) and (c) respectively are the experimental results, while the lower curves are the theoretical results.
(Wright and Hyoguchi, 1991)

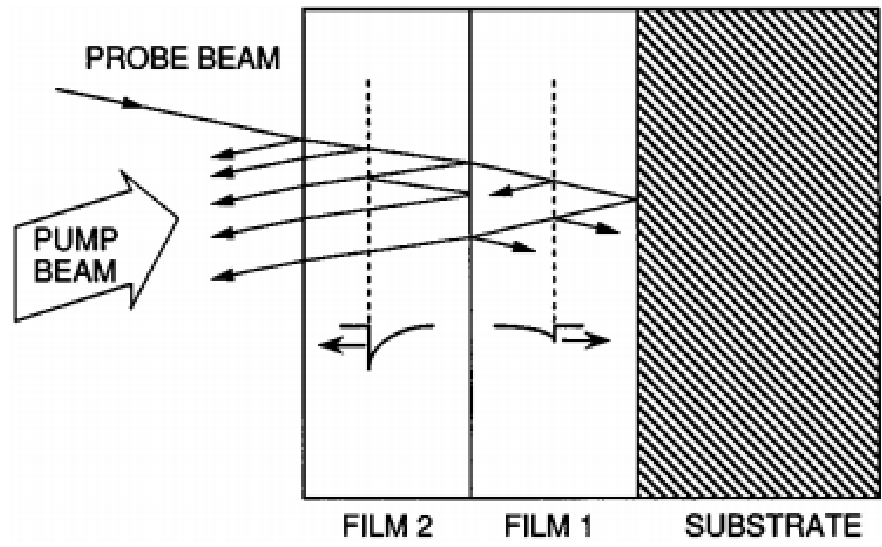

Figure 2.16: **The cross-section of the multilayered films during the test.** (Wright, 1995)

2.5 Gated-Camera

Gated camera is often used to analyze or observe chemical reactions (Leahy-Hoppa et al., 2010; Cessou et al., 2000; Lamb et al., 2000), medical diagnosis (Maddahi et al., 1979; Zevallos et al., 1999; Gayen et al., 2001), surveillance operations (Steinval et al., 1999) and florescence change (Mitchell, 2002).

In the field of surveillance, the gated-camera as shown in Figure 2.17 provides better visibility of objects in harsh weather conditions. This also provides advantages in critical military situations. The same imaging system is also used in turbid medium, with a brief analysis of absorption and backscattering is performed as well (He and Seet, 2001; Chua et al., 2011; Sluzek and Tan, 2004). The evaluation of volume of radioactive-tagged blood pumped by the ventricle of the heart can be done using a gated camera, and the volume of the blood is indirectly measured by the frames obtained from the camera and radiographic equipments. Diagnosis of cellular samples is performed by the gated camera too (Zevallos et al., 1999; Gayen et al., 2001). Normal cell and tumor cell samples can be successfully determined using time gated system too (Lin et al., 2009).

The gating of such camera is controlled by a delay circuitry which is a computer or a delay generator (Bentell et al., 2007). On synchronization of the reflection of laser pulse with the opening of the camera gate, an FPGA system is generally used (Xu, Zhang and Tang, 2011; Yang, Zhou, Fan and Wang, 2011). The implementation of the gating circuitry in the mentioned setup will sample the incoming wavefront every specified number of pico/nanoseconds.

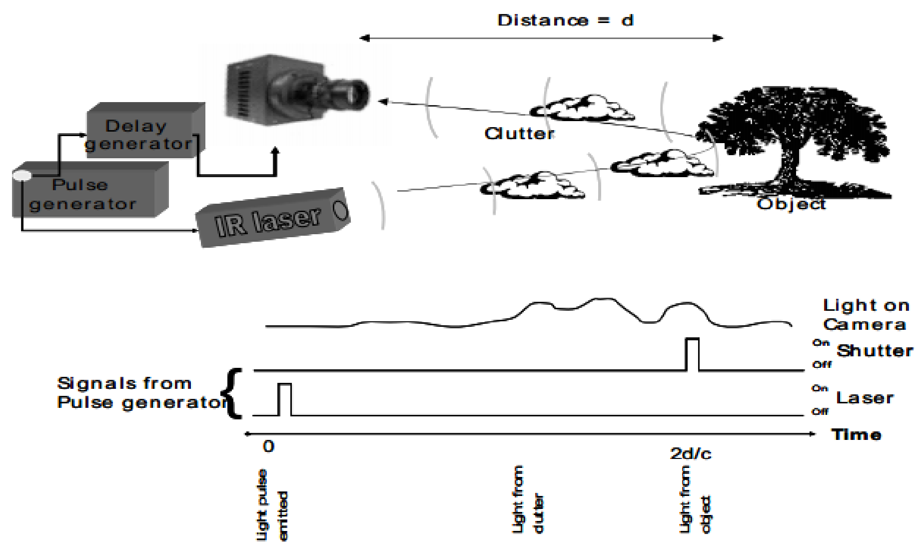

Figure 2.17: **Gated camera setup with the delay and pulse generator systems** (Bentell et al., 2007).

2.5.1 Gated-Camera Wavefront Sensor

A low-cost wavefront sensing in surface measurement is proposed based on the work by Tan, Wang, Ng, Lim et al. (2013) which combines the Shack-Hartmann sensor with the gated camera. The system is based on the design in the papers by Raymond et al. (2002) and Li, Zhao, Fang, Asundi and Yin (2008) but it is coupled with a gated camera/sensor (Schmitt, 1999; Drexler and Fujimoto, 2008; Li et al., 2007; Bentell et al., 2007) to measure the time for light to propagate within the interfaces. A short pulse of laser is emitted towards the material. Since no more interference fringes are measured, only the reflectance change and the time taken for the light waves to travel within the interfaces and back to the camera are obtained instead. A graph of reflectance change vs. time is plotted as the time goes by after the laser has impinged on the material.

On the other hand, the time taken for the reflected light pulse from the respective interfaces to the sensor dictates the thickness of the layer. With the preliminary information of refractive indexes in the stratified material, an optical model is formed. During the transmission and reflection of the light pulse, only a few reflections between the interfaces must be measured. It is because continuous reflections between the interfaces will affect the reflectance change and the results converge.

The intensities of each reflectance change are then compared to the optical model. If the error is below the specified threshold, the coordinate of the point and the gradient is then calculated through the centroiding method.

The process occurs simultaneously for other same light beams which originate from the beam splitter, forming a square array of beams which will impinge onto the surface of the material. The gated camera continuously captures the frame/beam array emitted from the surface of the material for each time step. After the square array of coordinates and gradients are calculated, it is stored in the computer memory. On each interface, the respective coordinates and gradients are then approximated onto a surface by using Southwell wavefront reconstruction method (Southwell, 1980). The process is repeated until the whole area of the material is covered. Stitching of the square arrays is done to finalize the topographies of the interfaces in the material tested.

CHAPTER 3

MATERIALS AND METHODS

3.1 Schematics of Shack-Hartmann Gated-Camera Setup

A proposed gated camera Shack-Hartmann setup in Figure 3.1 consists of a gated intensified CCD camera system, pulsed laser emitter, collimator, prism, filters, adjustable stage, and a Shack-Hartmann sensor (Tan, Wang, Ng, Lim and Chai, 2013). The emission time of the pulse laser emitter and the shutter time of the gated camera are controlled by a delay generator. The images of the resultant array of dots are captured by the gated camera and then saved inside the computer. From there, the computer processes the information of the results and therefore a wavefront is reconstructed.

The gating time of the camera depends on the total distances in the following list:

1.) The distance between the laser pulse emitter and the prism.

2.) The distance between the camera and the prism.

3.) The distance between the prism and the material surface.

4.) The distance between the prism and the material sub-surface.

Dividing the total distance by the speed of light, c, the gating time is obtained to capture the wavefront reflected from the material surface or the subsurface. Any incorrect gating time affects the results and a possibly wrong wavefront is captured.

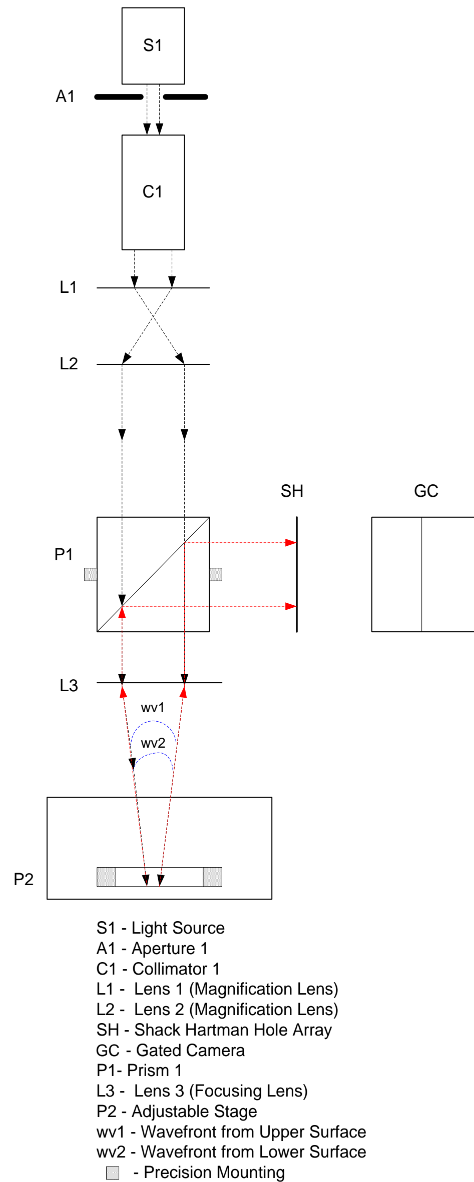

Figure 3.1: Proposed gated-camera wavefront sensing system
(Tan, Wang, Ng, Lim and Chai, 2013).

3.2 Assumptions

The components in the system and the behaviour of the pulsed laser such as the shape and intensity of the pulse are assumed to be ideal in order to facilitate the simulation process. In practice, aberrations in optical components, propagation delays in the gating circuitries and an uneven laser pulse are present in the system. The assumptions made are:

1.) Short laser pulse emerging from the laser emitter is assumed to be flat. In practice the surface of the pulsed laser must be corrected with a deformable mirror prior to impinging the material. The flat wavefront is required in the simulation and in actual hardware because when a distorted wavefront impinges and traverses between the surfaces, further distortions will occur and possibly render the output meaningless. In addition, a flat wavefront is also a reference wavefront to provide a proper slope measurement on the output wavefronts.

2.) The laser pulse is assumed to be very short (10 femtoseconds) to facilitate the process of raytracing simulation. An actual travelling pulsed laser has stacks of wavefronts with undulating intensities.

3.) The reflected wavefront is not continuously sampled for light intensity changes. It is only sampled when the wavefront is captured from the surface, and the subsurface of the material. The refractive index and the thickness of the material are assumed to be known.

3.3 Mechanisms of surface and subsurface detection

Once the laser pulse is emitted towards the material, the shutter in the gated camera opens when the pulse has travelled up to $d_{LP} + 2(d_{PM}) + d_{PC}$ units, as shown in Figure 3.2. Dividing it by the constant of the speed of light, c, the number of seconds required for the shutter to open after the laser pulse is emitted is calculated. The wavefront approaching to the camera is broken down into an array of displaced dots by the Shack-Hartmann sensor, and the opening of the shutter causes the CCD to capture these mentioned dots instantly. The wavefront information of the surface of the material is successfully obtained.

To measure the subsurface (or the second interface) of the material, the distance between the first interface and the subsurface of the material must be considered into the calculation. Therefore, the shutter of the gated camera opens when the pulse has travelled up to $d_{LP} + 2(d_{PM} + d_{MMS}) + d_{PC}$ units. Figure 3.3 illustrates the measurement of the subsurface. Similarly, this is divided by c and the number of seconds required for the shutter to open is then computed.

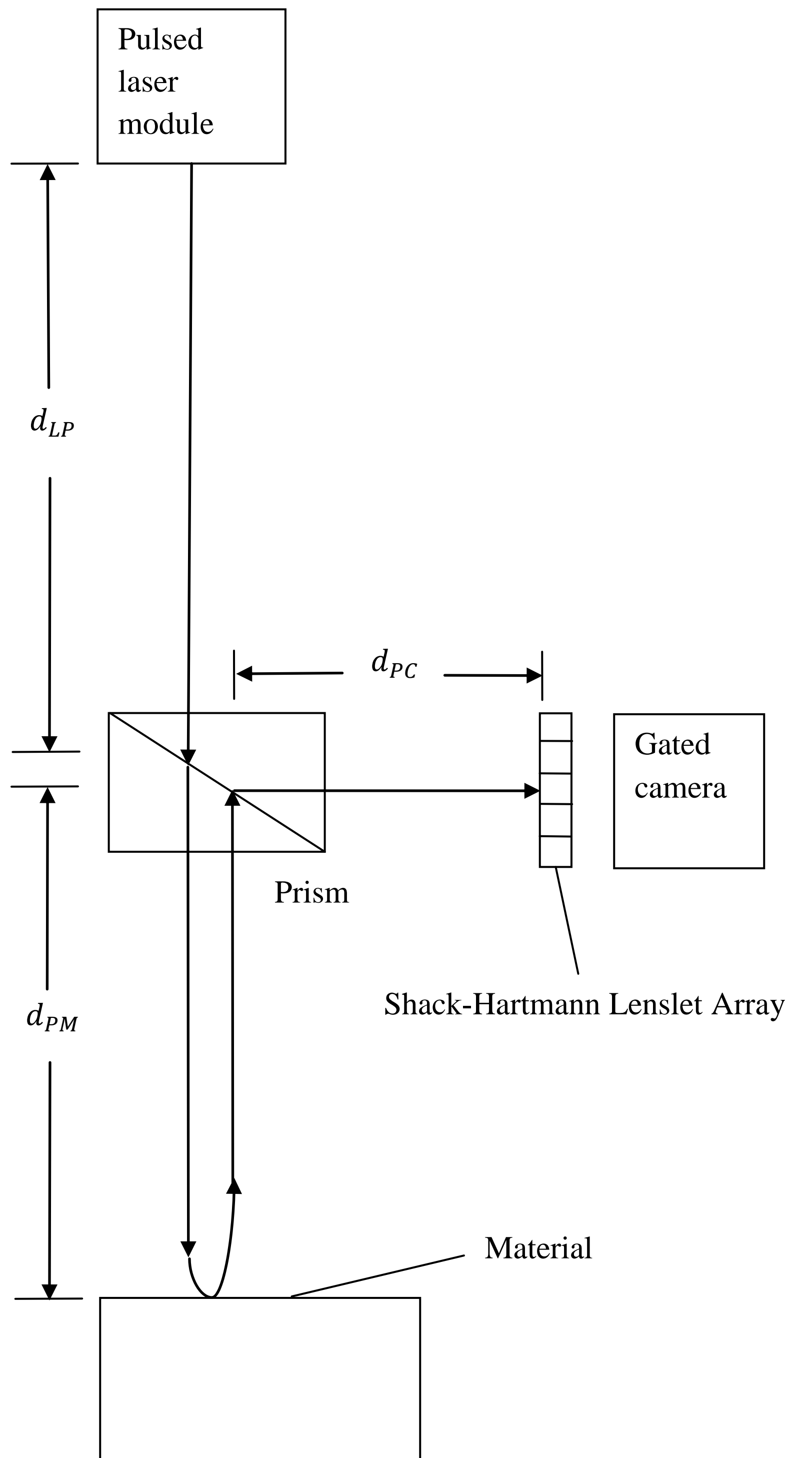

Figure 3.2: Capturing the wavefront reflected from the surface of the material.

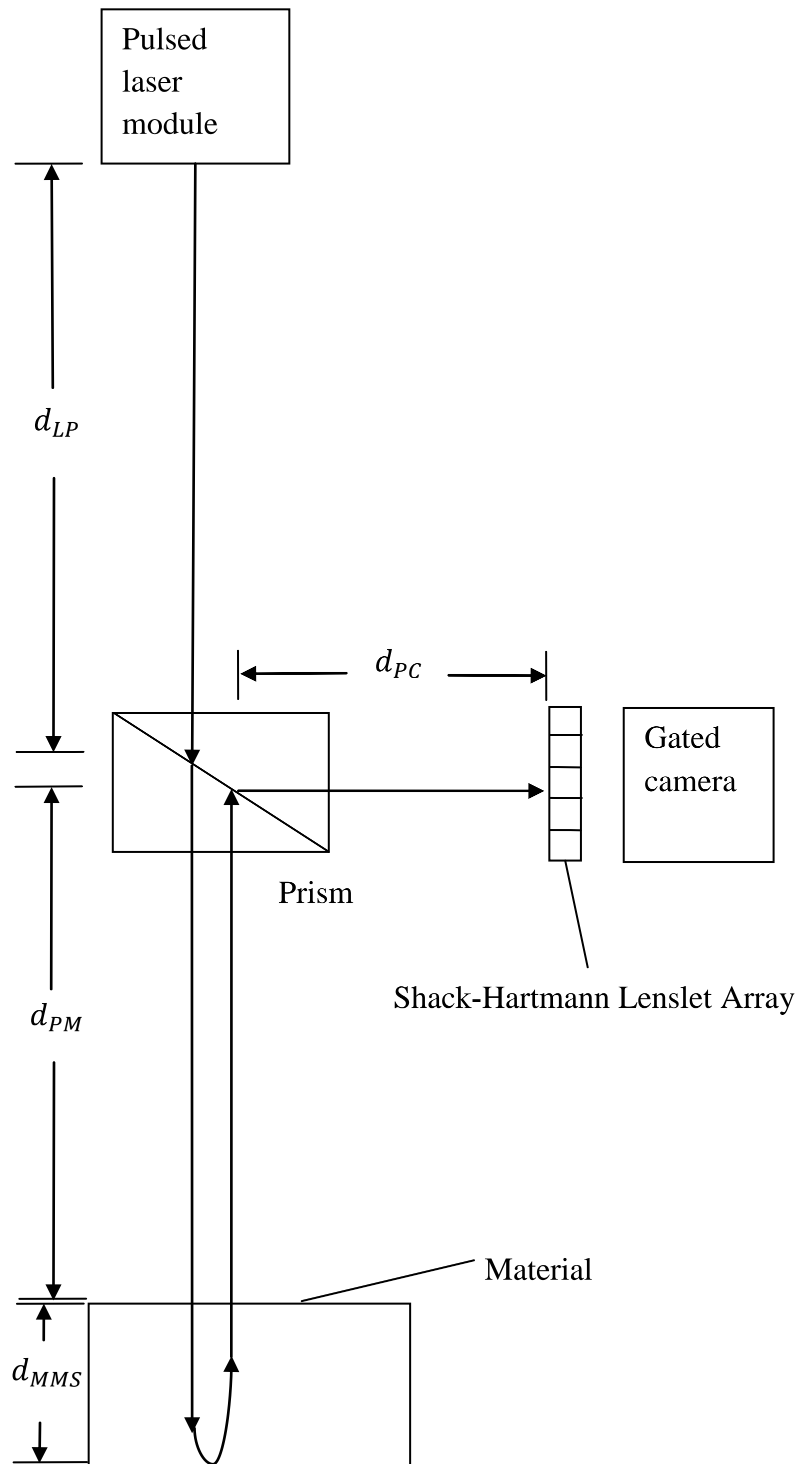

Figure 3.3: Capturing the wavefront reflected from the subsurface of material.

A flat wavefront is impinged onto a surface of a material which results in reflection and transmission. The gated camera catches the first reflection from the surface (first interface) of the material by opening the shutter after a period of time the laser pulse is emitted towards the material. The reflected wavefront goes through the Shack-Hartmann sensor and then into the gated camera, forming a grid of displaced dots. The displacements of the dots represent the slopes/gradients of the reflected wavefront, and a surface is then reconstructed using this information.

Meanwhile on the first interface some of the wavefront has been transmitted into the material by refraction. The refracted wavefront is reflected by the sub-surface (second interface) of the material, and then refracted again by the surface (first interface). Because of the extra time taken for the wavefront to travel between the interfaces, the shutter of the gated camera is only opened a few more nanoseconds after capturing the first wavefront. The shutter of the camera is controlled by a delay generator.

However, the captured wavefront does not match the actual sub-surface profile as it has been distorted by the refraction on the first interface after the wavefront is refracted from the bottom surface. Therefore, the mentioned wavefront cannot be assumed as a second surface.

A simulation of the behaviour of the wavefront is perfomed using Matlab. The flat wavefront is represented by a fixed square array of rays which are projected towards the surface of the material. Ray tracing algorithms are employed to calculate the path of the rays which travel between the interfaces. Two analytical surfaces separated by a distance d are computed to simulate the shape of the material.

3.4 Simulation of Wavefront by Ray-Tracing (Two Interfaces)

A fixed grid of incoming rays in Figure 3.4 which are perpendicular to the surface is reflected from the first surface. Each ray is represented by an incident vector, $\overrightarrow{I_0}$:

$$\overrightarrow{I_0} = x\boldsymbol{i} + y\boldsymbol{j} + \phi\boldsymbol{k}$$

The ray is reflected by the point A on the first surface, $F_1(x, y, \phi)$ (Glassner, 1989). The point of the surface $\vec{N}_0$ is the normal vector:

$$\vec{N}_0 = \frac{\partial F_1}{\partial x}\boldsymbol{i} + \frac{\partial F_1}{\partial y}\boldsymbol{j} + \frac{\partial F_1}{\partial \phi}\boldsymbol{k}$$

With the incoming ray vector and the normal vector of the surface, the reflected ray can be obtained by using the common reflection equation (Glassner, 1989):

$$\hat{\vec{R}}_0 = \hat{\vec{I}}_0 - 2\left(\widehat{\overrightarrow{I_0}} \cdot \widehat{\overrightarrow{N_0}}\right)\hat{\vec{N}}_0$$

Prior to calculating the reflected ray vector, both of the incoming ray vector and the normal vector of the surface must be normalized first:

$$\widehat{\overrightarrow{I_0}} = \frac{\overrightarrow{I_0}}{\|\overrightarrow{I_0}\|} \text{ and } \widehat{\overrightarrow{N_0}} = \frac{\overrightarrow{N_0}}{\|\overrightarrow{N_0}\|}$$

The angle between the vectors $\overrightarrow{I_0}$ and the $\overrightarrow{N_0}$ is computed and then converted into x-y displacement values which are seen in an individual grid in the Shack-Hartmann sensor. The first surface is reconstructed by means of general interpolation methods such as cubic.

Afterwards, in Figure 3.4, a part of the ray is transmitted into the material. Another refracted vector $\vec{T}_0$ is formed by using the refraction equations (Glassner, 1989):

$$cos\theta_i = -\vec{\hat{I}}_0 \cdot \vec{\hat{N}}_0$$

$$\sin^2\theta = \left(\frac{n_1}{n_2}\right)^2 (1 - \cos^2\theta_i)$$

$$\overrightarrow{\hat{T}_0} = \frac{n_1}{n_2}\vec{\hat{I}}_0 - \left(\frac{n_1}{n_2}\cos\theta_i + \sqrt{1-\sin^2\theta_i}\right)\vec{\hat{N}}_0$$

Similarly, the vectors are normalized before calculation. The refractive indexes are between the interface are n_1 and n_2 and the incident angle is θ_i.

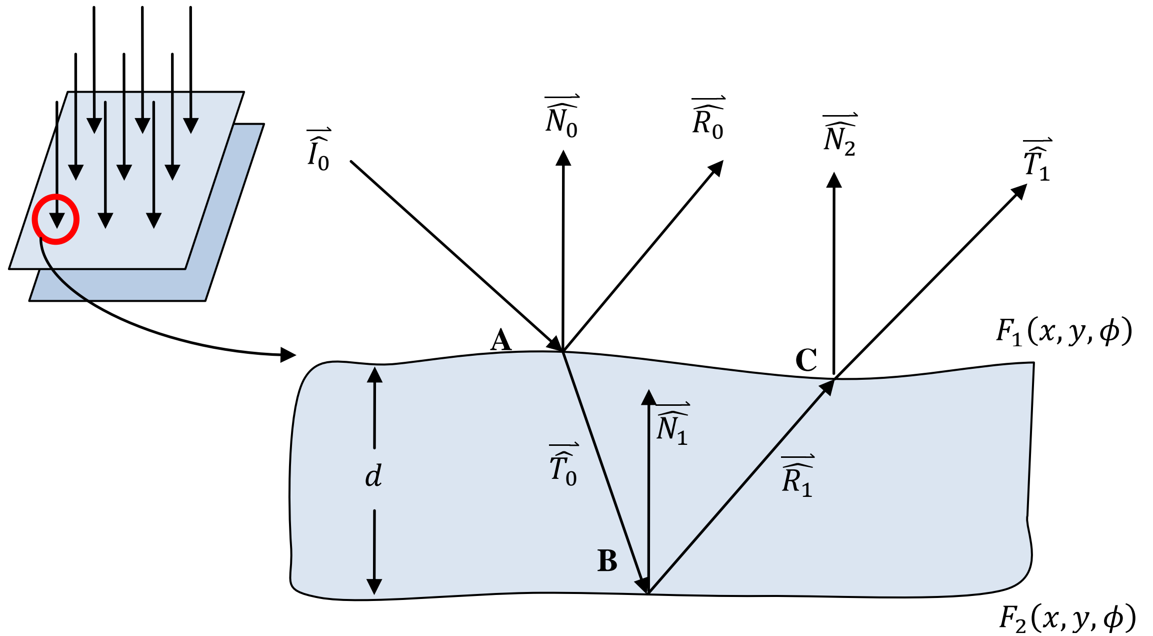

Figure 3.4: Cross section of a material with a ray propagating within two interfaces.

Then in Figure 3.5, using the point A and the vector $\vec{T}_0$, a line is constructed across the two interfaces to find the point B, which is the intersection on the second surface, $F_2(x, y, \phi)$.

The equation of the line is as follows:

$$L_1(x_{L1}, y_{L1}, \phi_{L1}) = A + \lambda_1 \overrightarrow{\hat{T}_0}$$

Substituting each of the components in L_1 into $F_2(x, y, \phi)$ and then solving for $F_2(x_{L1}, y_{L1}, \phi_{L1}) = 0$, one or two λ_1 is obtained. Only the smallest value and its index number are picked because the line and the intersection must be within the sampling area of the wavefront. When a suitable λ_1 is chosen, the intersection on the second surface on point B is calculated.

The normal of the surface on point B is also obtained:

$$\vec{N}_1 = \frac{\partial F_2}{\partial x}\boldsymbol{i} + \frac{\partial F_2}{\partial y}\boldsymbol{j} + \frac{\partial F_2}{\partial \phi}\boldsymbol{k}$$

When the transmitted ray, $\overrightarrow{T_0}$ impinges onto the intersection point of the second surface, B with the normal $\overrightarrow{N_1}$, the ray is reflected from the surface again. Similarly, using the reflection equation, the reflected ray, $\overrightarrow{R_1}$ can be described as:

$$\hat{\vec{R}}_1 = \hat{\vec{T}}_0 - 2\left(\widehat{\overrightarrow{T_0}} \cdot \widehat{\overrightarrow{N_1}}\right)\hat{\vec{N}}_1$$

The vectors must be normalized before $\overrightarrow{R_1}$ is calculated.

Then, to evaluate the ray exiting from the second surface through the first surface, another line equation must be formed by using the following equation:

$$L_2(x_{L2}, y_{L2}, \phi_{L2}) = B + \lambda_2 \overrightarrow{R_1}$$

Solving for λ_2, the intersection point, C on the first surface is calculated. With the intersection, the normal of the surface on point C is obtained:

$$\vec{N}_2 = \frac{\partial F_1}{\partial x}\boldsymbol{i} + \frac{\partial F_1}{\partial y}\boldsymbol{j} + \frac{\partial F_1}{\partial \phi}\boldsymbol{k}$$

To obtain $\overrightarrow{T_1}$, the vector $\overrightarrow{R_1}$ is substituted into the refraction equations.

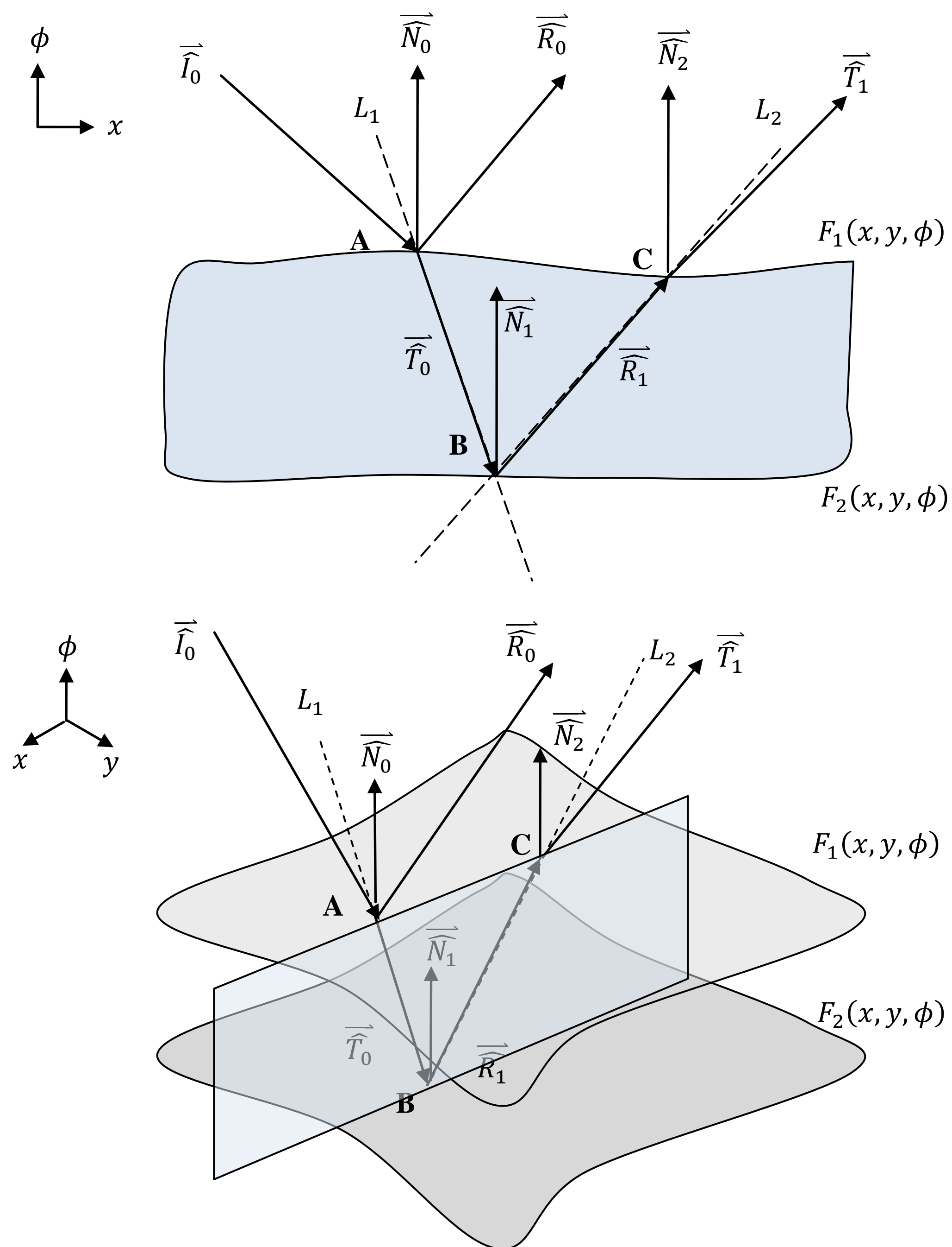

Figure 3.5: **Lines L1 and L2 are constructed across the interfaces to find the reflection and refraction points at point B and C.**

3.5 Zernike Decomposition

Once the wavefronts have been obtained, these are decomposed into a number of Zernike coefficients. In the Zernike decomposition, a wavefront is composed of a sum of Zernike polynomials, and each of these is multiplied by its respective coefficients. The shape of the wavefront is generally determined by the sums of the polynomials, with each of the polynomial are multiplied by its coefficients.

$$F_{surface}(x, y, \phi) = \sum_{n=0}^{N} c_n Z_n$$

where c_n is the *n*th Zernike coefficient, and Z_n is the *n*th Zernike polynomial (Dai, 2008). The first 10 Zernike polynomials in Cartesian form and its derivatives are listed in Table 3.1.

n	$Z_n(X,Y)$	$\frac{\partial Z_n(X,Y)}{dX}$	$\frac{\partial Z_n(X,Y)}{dY}$
1	$2Y$	0	2
2	$2X$	2	0
3	$\sqrt{6}\,2XY$	$\sqrt{6}\,2Y$	$\sqrt{6}\,2X$
4	$\sqrt{3}(2X^2 - 2Y^2 - 1)$	$\sqrt{3}\,4X$	$\sqrt{3}\,4Y$
5	$\sqrt{6}(X^2 - Y^2)$	$\sqrt{6}\,2X$	$\sqrt{6}(-2Y)$
6	$\sqrt{8}(3X^2Y - Y^3)$	$\sqrt{8}\,6XY$	$\sqrt{8}(3X^2 - 3Y^2)$
7	$\sqrt{8}(3X^2Y + 3Y^3 - 2Y)$	$\sqrt{8}\,6XY$	$\sqrt{8}(3X^2 + 9Y^2 - 2)$
8	$\sqrt{8}(3X^3 + 3XY^2 - 2X)$	$\sqrt{8}(9X^2 + 3Y^2 - 2)$	$\sqrt{8}\,6XY$
9	$\sqrt{8}(X^3 - 3XY^2)$	$\sqrt{8}(3X^2 - 3Y^2)$	$\sqrt{8}(-6XY)$
10	$\sqrt{10}(4X^3Y - 4XY^3)$	$\sqrt{10}(12X^2Y - 4Y^3)$	$\sqrt{10}(4X^3 - 12XY^2)$

Table 3.1: List of first 10 Zernike Polynomials. The Zernike Polynomials in the table is in Cartesian form and with derivatives of the polynomials in respect of X and Y coordinates (Schwiegerling, 2011).

Since the output of the Shack-Hartmann sensor is the array of slopes on the wavefront, the equation is now differentiated in respect of *x* and *y* coordinates. The grid number in the Shack-Hartmann sensor is represented by *K*.

$$\left(\frac{\partial F_{surface}}{\partial x}\right)_K = \sum_{i=1}^{N} c_i \left(\frac{\partial Z_i}{\partial x}\right)_K$$

$$\left(\frac{\partial F_{surface}}{\partial y}\right)_K = \sum_{i=1}^{N} c_i \left(\frac{\partial Z_i}{\partial y}\right)_K$$

By combining these arrays of slopes and then lumping them in matrix form, the coefficients are obtained by solving the equation for *c*:

$$\boldsymbol{s} = \boldsymbol{cE}$$

$$\begin{bmatrix} \left(\frac{\partial F}{dx}\right)_1 \\ \left(\frac{\partial F}{dx}\right)_2 \\ \vdots \\ \left(\frac{\partial F}{dx}\right)_K \\ \left(\frac{\partial F}{dy}\right)_1 \\ \left(\frac{\partial F}{dy}\right)_2 \\ \vdots \\ \left(\frac{\partial F}{dy}\right)_K \end{bmatrix} = \begin{bmatrix} c_1 \\ c_2 \\ c_3 \\ \vdots \\ c_N \end{bmatrix} \begin{bmatrix} \left(\frac{\partial Z_1}{dx}\right)_1 & \left(\frac{\partial Z_2}{dx}\right)_1 & \left(\frac{\partial Z_3}{dx}\right)_1 & \cdots & \left(\frac{\partial Z_N}{dx}\right)_1 \\ \left(\frac{\partial Z_1}{dx}\right)_2 & \left(\frac{\partial Z_2}{dx}\right)_2 & \left(\frac{\partial Z_3}{dx}\right)_2 & \cdots & \left(\frac{\partial Z_N}{dx}\right)_2 \\ \vdots & \vdots & \vdots & \ddots & \vdots \\ \left(\frac{\partial Z_1}{dx}\right)_K & \left(\frac{\partial Z_2}{dx}\right)_K & \left(\frac{\partial Z_3}{dx}\right)_K & \cdots & \left(\frac{\partial Z_N}{dx}\right)_K \\ \left(\frac{\partial Z_1}{dy}\right)_1 & \left(\frac{\partial Z_2}{dy}\right)_1 & \left(\frac{\partial Z_3}{dy}\right)_1 & \cdots & \left(\frac{\partial Z_N}{dy}\right)_1 \\ \left(\frac{\partial Z_1}{dy}\right)_2 & \left(\frac{\partial Z_2}{dy}\right)_2 & \left(\frac{\partial Z_3}{dy}\right)_2 & \cdots & \left(\frac{\partial Z_N}{dy}\right)_2 \\ \vdots & \vdots & \vdots & \ddots & \vdots \\ \left(\frac{\partial Z_1}{dy}\right)_K & \left(\frac{\partial Z_2}{dy}\right)_K & \left(\frac{\partial Z_3}{dy}\right)_K & \cdots & \left(\frac{\partial Z_N}{dy}\right)_K \end{bmatrix}$$

where ***s*** is the column matrix which contains all the *x* and *y*-slope information, ***E*** are the derivatives of the Zernike polynomials, and ***c*** are the Zernike coefficients.

Finally, the Zernike coefficients can be obtained by using a generalised least squares solution. Starting with the equation mentioned previously:

$$\boldsymbol{s} = \boldsymbol{cE}$$

Multiplying both sides with $\boldsymbol{E^T}$:

$$\boldsymbol{E^T s} = \boldsymbol{cE}(\boldsymbol{E^T})$$

Solving for $\boldsymbol{c}$:

$$\boldsymbol{c} = \boldsymbol{E^T}(\boldsymbol{E^T E})^{-\mathbf{1}}\boldsymbol{s}$$

$$\boldsymbol{c} = \boldsymbol{E}^{+}\boldsymbol{s}$$

However, the $\boldsymbol{E}^{+}$ could not be computed due to the ill-conditioned nature of the matrix, and the matrix has a determinant of zero. Solving this in Matlab by using the '\' operator does not guarantee an accurate result. So, another approach must be used to tackle the problem, which is by using Singular Value Decomposition (SVD) (Dai, 2008).

3.5.1 Singular Value Decomposition (SVD)

The $\boldsymbol{E}$ matrix is factorized into three simpler and manageable components, which are the $\boldsymbol{U}$, $\boldsymbol{D}$ and $\boldsymbol{V^T}$ (Schlick, 2010):

$$SVD(\boldsymbol{E}) = \boldsymbol{UDV}^T$$

$\boldsymbol{U}$ and $\boldsymbol{V}$ are square orthogonal matrices, and $\boldsymbol{D}$ is the rectangular $(m \times n)$ diagonal matrix.

Starting from $\boldsymbol{E}$, multiplying it by its transpose, $\boldsymbol{E^T}$ and then finding the eigenvalues, the singular values $\sigma_1, \sigma_2, \dots, \sigma_n$ are obtained by square-rooting the eigenvalues. Putting those into the diagonal matrix in the order $\sigma_1 > \sigma_2 > \cdots > \sigma_n$ results to $\boldsymbol{D}$.

$$\det(\boldsymbol{E^T E} - \lambda \boldsymbol{I}) = \lambda_1, \lambda_2, \dots \lambda_n$$

$$\sigma_1 = \sqrt{\lambda_1}, \sigma_2 = \sqrt{\lambda_2}, \dots, \sigma_n = \sqrt{\lambda_n}$$

$$\boldsymbol{D} = \begin{pmatrix} \sigma_1 & 0 & 0 & \cdots & 0 \\ 0 & \sigma_2 & 0 & \cdots & 0 \\ 0 & 0 & \sigma_3 & \cdots & 0 \\ \vdots & \vdots & \vdots & \ddots & \vdots \\ 0 & 0 & 0 & \cdots & \sigma_n \end{pmatrix}$$

After that, for each eigenvalue, the following equation is reduced into row-echelon form:

$$E^T E - \lambda_n I = 0$$

The nullspaces, which are vectors $\overrightarrow{v_1}, \overrightarrow{v_2}, \dots, \overrightarrow{v_n}$ solved from the equation are normalized, and then horizontally concatenated, forming $\boldsymbol{V}$:

$$\boldsymbol{V} = [\overrightarrow{v_1} \quad \overrightarrow{v_2} \quad \dots \quad \overrightarrow{v_n}]$$

Using the information from the calculation of matrices $\boldsymbol{D}$ and $\boldsymbol{V}$, the individual vectors $\overrightarrow{u_1}, \overrightarrow{u_2}, \dots, \overrightarrow{u_n}$ are also calculated:

$$\overrightarrow{u_n} = \frac{1}{\sigma_n} \boldsymbol{E} \overrightarrow{v_n}$$

Similarly, the vectors are concatenated:

$$\boldsymbol{U} = [\overrightarrow{u_1} \quad \overrightarrow{u_2} \quad \dots \quad \overrightarrow{u_n}]$$

To verify that the decomposition is correct and valid, the product of $\boldsymbol{V^T}$, $\boldsymbol{U}$ and $\boldsymbol{D}$ finally results in $\boldsymbol{E}$.

Since the matrices $\boldsymbol{U}$ and $\boldsymbol{V}$ are square matrices and are orthogonal, the inverse of the matrices are equal to the transpose. Therefore, inversing the SVD of $\boldsymbol{E}$ is an extremely simple operation:

$$(\boldsymbol{U}\boldsymbol{D}\boldsymbol{V}^T)^{-1} = \boldsymbol{U}^T \boldsymbol{D}^{-1} \boldsymbol{V}$$

The inverse of $\boldsymbol{D}$ could not be computed because it is not a square matrix, so each diagonal element in $\boldsymbol{D}$ is reciprocated. On instances where there is a zero in the element, it is not reciprocated and the element remains as a zero.

$$\boldsymbol{D}^{+} = \boldsymbol{D}^{-1} = \begin{pmatrix} \frac{1}{\sigma_1} & 0 & 0 & \cdots & 0 \\ 0 & \frac{1}{\sigma_2} & 0 & \cdots & 0 \\ 0 & 0 & \frac{1}{\sigma_3} & \cdots & 0 \\ \vdots & \vdots & \vdots & \ddots & \vdots \\ 0 & 0 & 0 & \cdots & \frac{1}{\sigma_n} \end{pmatrix}$$

Multiplying this to the slope matrix $\boldsymbol{s}$, the coefficients are directly computed.

$$\boldsymbol{c} = \boldsymbol{V}\boldsymbol{D}^{-1}\boldsymbol{U}^{T}\boldsymbol{s}$$

The magnitudes of each coefficient in $\boldsymbol{c}$ in a surface determine the overall shape of the surface (Zernike, 1934).

Solving an ill-conditioned matrix is automatically done in Matlab by using the Singular Value Decomposition (SVD) functions which are already provided as part of the software (Dai, 2008).

As mentioned earlier, a wavefront can be composed of different Zernike polynomials. For an example, in Figure 3.6, if a wavefront contains nothing but only Z_5 with a coefficient of -0.01, the decomposition will result in a chart with a Z_5 peak with the lowest value of -0.01. The Z_5 surface is chosen in the simulation because it resembles a generic deformation pattern which is 'astigmatism' in semiconductor wafer and thin film processing (Zorich, 1991; Peth et al., 2003; Mueller et al., 2008).

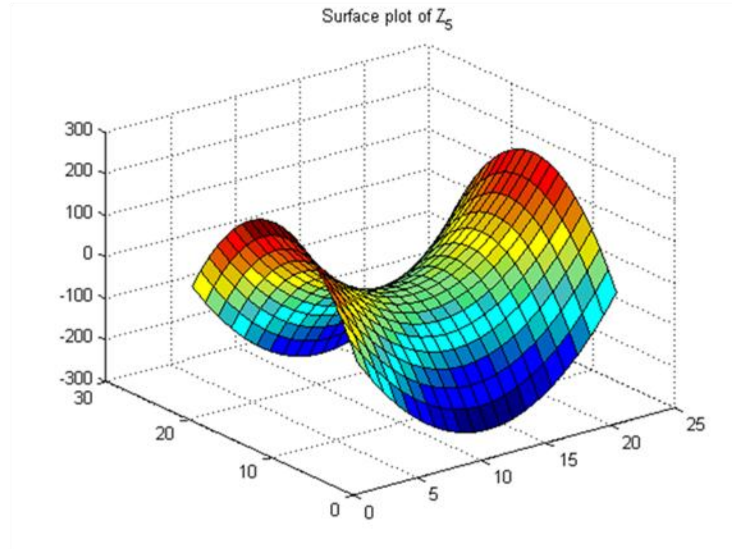

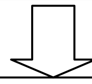

Zernike Decomposition

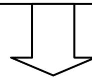

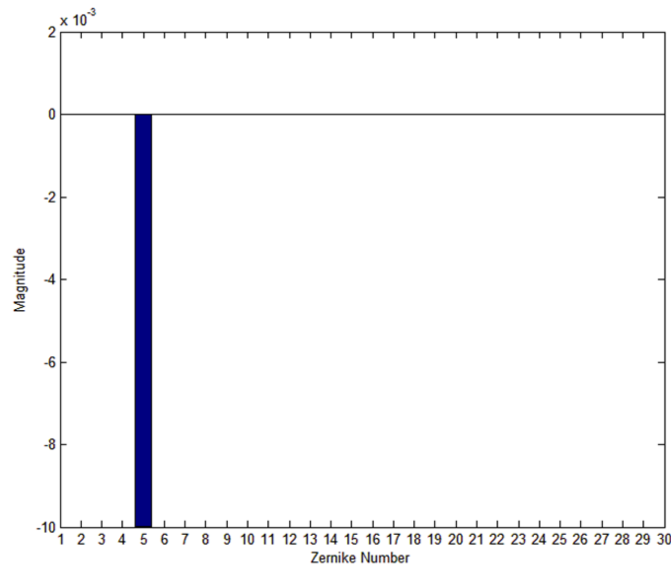

Figure 3.6: Zernike decomposition of a surface/wavefront with only -0.01Z_5. The resultant chart shows only one peak, exactly at Z_5, with the value of -0.01.

CHAPTER 4

RESULTS AND DISCUSSIONS

In this project, eight different sets of parameters from a combination of refractive indexes, material thickness, gradient sizes and type of surface are used to study the parameters which affect the reflected subsurface wavefront. These parameters are summarised in Table 4.1.

Section	Identical surfaces	Coefficients	Refractive indexes	Distances between two interfaces
4.1	Z_5	0.001	Fixed (n = 1.55)	Varying
4.2		0.001	Varying	Fixed (0.001 units)
4.3		Varying	Fixed (n = 1.55)	Fixed (0.001 units)
4.4		0.000001	Fixed (n = 1.55)	Varying
4.5		0.000001	Varying	Fixed (0.001 units)
4.6	$Z_5 + Z_7 + Z_8$	0.000001	Fixed (n = 1.55)	Varying
4.7		0.000001	Varying	Fixed (0.001 units)
4.8	Varying	0.000001	Fixed (n = 1.55)	Fixed (0.001 units)

Table 4.1: The eight different parameters which are used in the simulation.

4.1 Identical surfaces (Z_5) with larger coefficients (0.001) and varying distances between two interfaces.

In Figure 4.1, Z_4, Z_5 and Z_{13} have the highest magnitude, while the other higher order Zernikes are present in relatively smaller magnitudes. Z_4 and Z_5 are mainly predominant in the reflected subsurface wavefront. Ideally, the reflected subsurface wavefront captured has the same shape as the actual subsurface of the material. However, due to the reflection and the refractions between the interfaces, the subsurface wavefront is distorted. The distortion has caused the slight alteration of the mentioned wavefront, where some sagging on its corners is noticed. A small number of higher order Zernikes are responsible for the slight deformation of the mentioned wavefront.

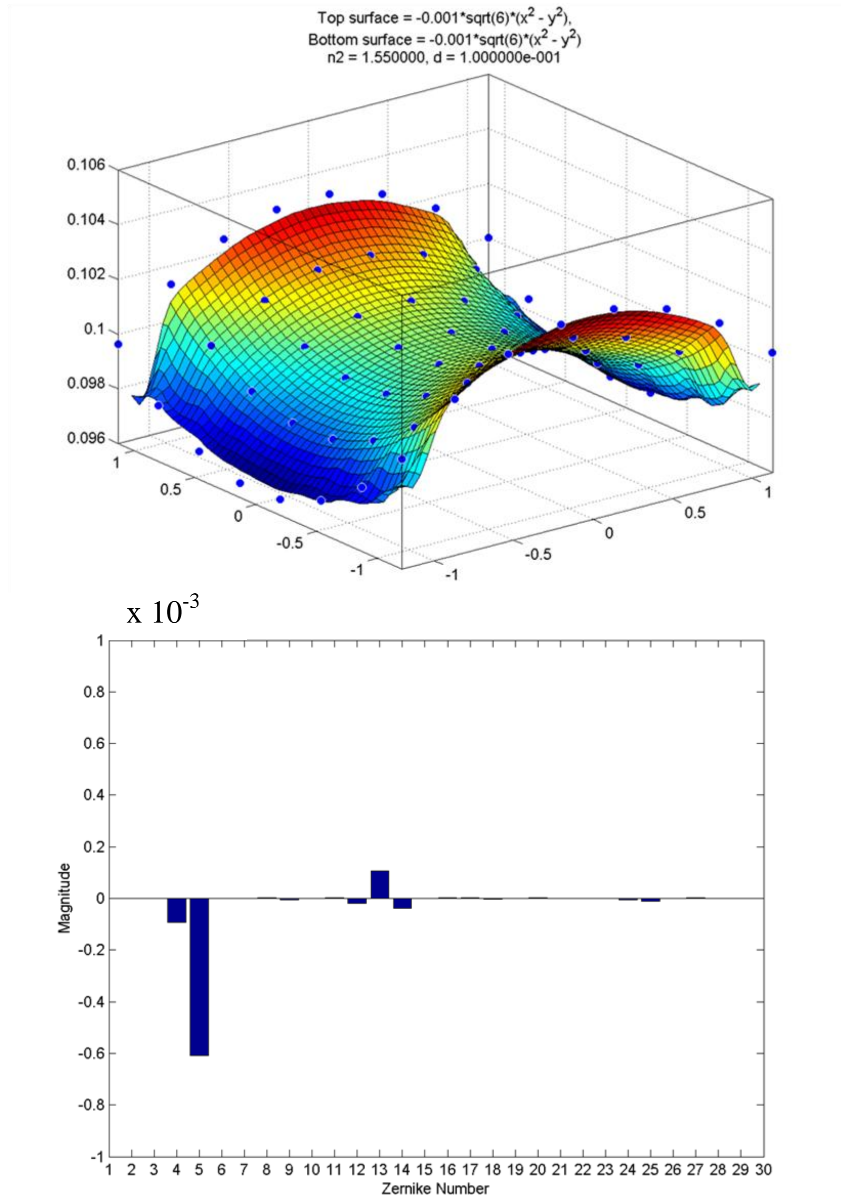

Figure 4.1: **Top and bottom surfaces are Z5 with large coefficients (0.001) and distance between these surfaces is 0.1 units.**

Similarly, in Figures 4.2 to 4.4, changes in the Zernike components are minor in nature. In Figure 4.2, the coefficient of Z_5 is around -0.46×10^{-3}, and the other higher order component such as Z_{13} has slightly increased to around 0.12×10^{-3}. Meanwhile, in Figure 4.3, the magnitude of Z_5 has increased back to around 0.7×10^{-3} and the Z_{13} is increased to 1.6×10^{-4}. The other higher order Zernike components such as Z_{18} to Z_{30} are noticed in the decomposition but in very small magnitudes. Afterwards, on the material thickness of 1×10^{-4} units, the wavefront contains approximately $-0.3 \times 10^{-3} Z_5$ and the Z_{13} is 0.2×10^{-3}, as shown in Figure 4.4. The coefficient of Z_5 and Z_{13} in Figure 4.5 are -0.71×10^{-3} and 0.06×10^{-3}.

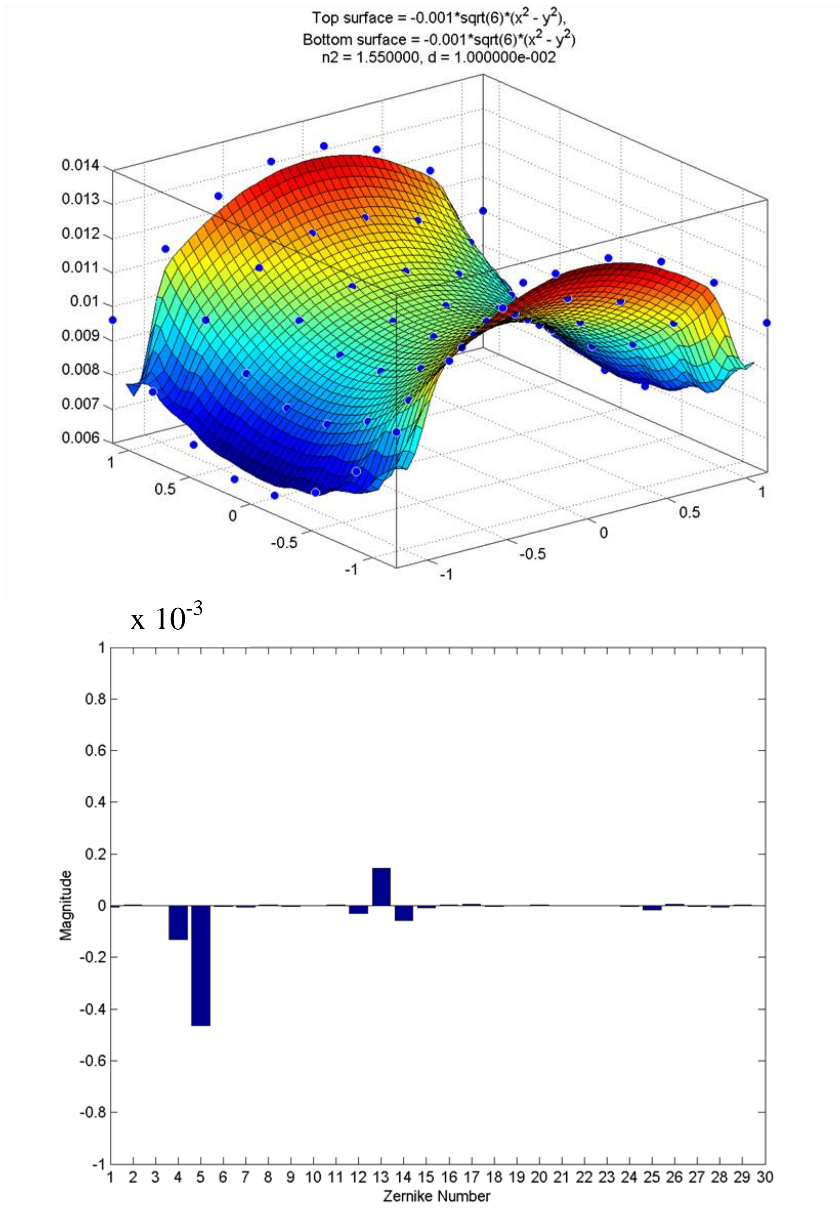

Figure 4.2: Top and bottom surfaces are Z5 with large coefficients (0.001) and distance between these surfaces are 0.01 units.

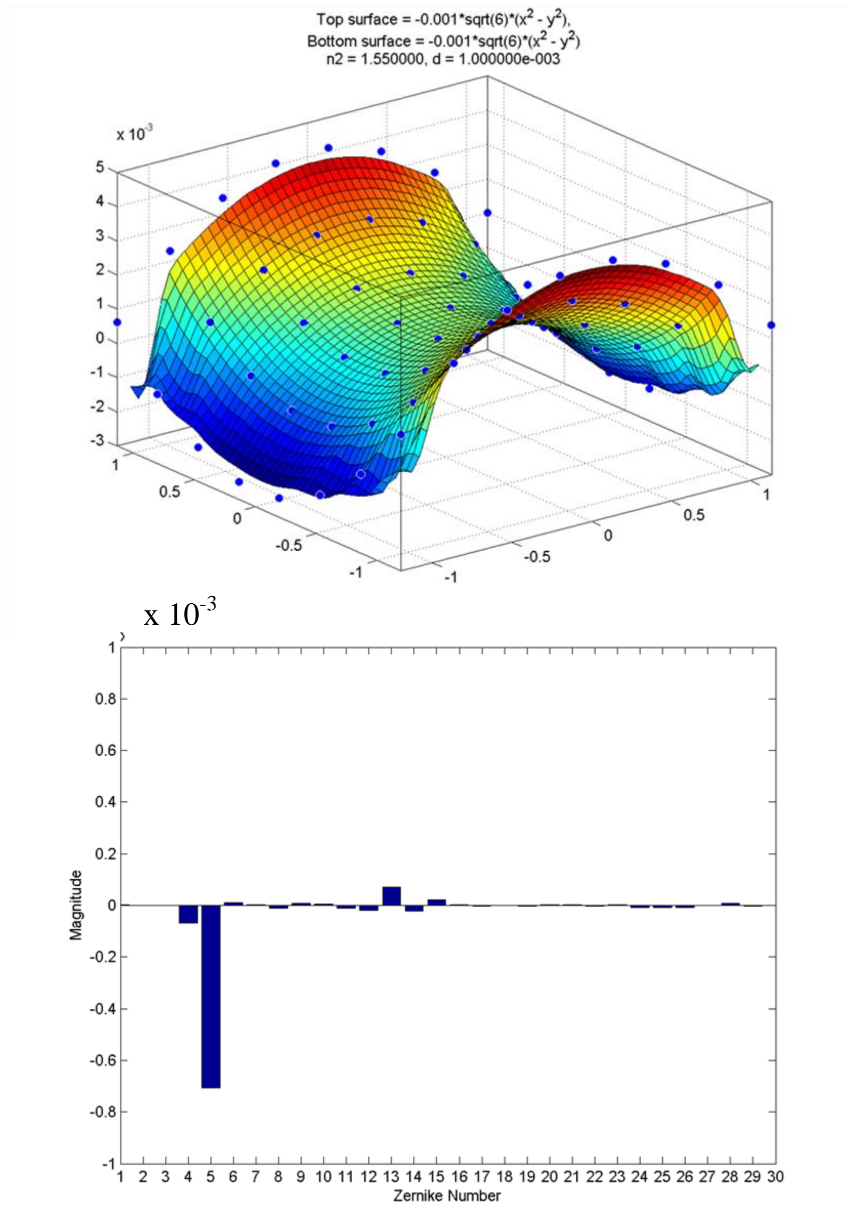

Figure 4.3: Top and bottom surfaces are Z5 with large coefficients (0.001) and distance between these surfaces are 0.001 units.

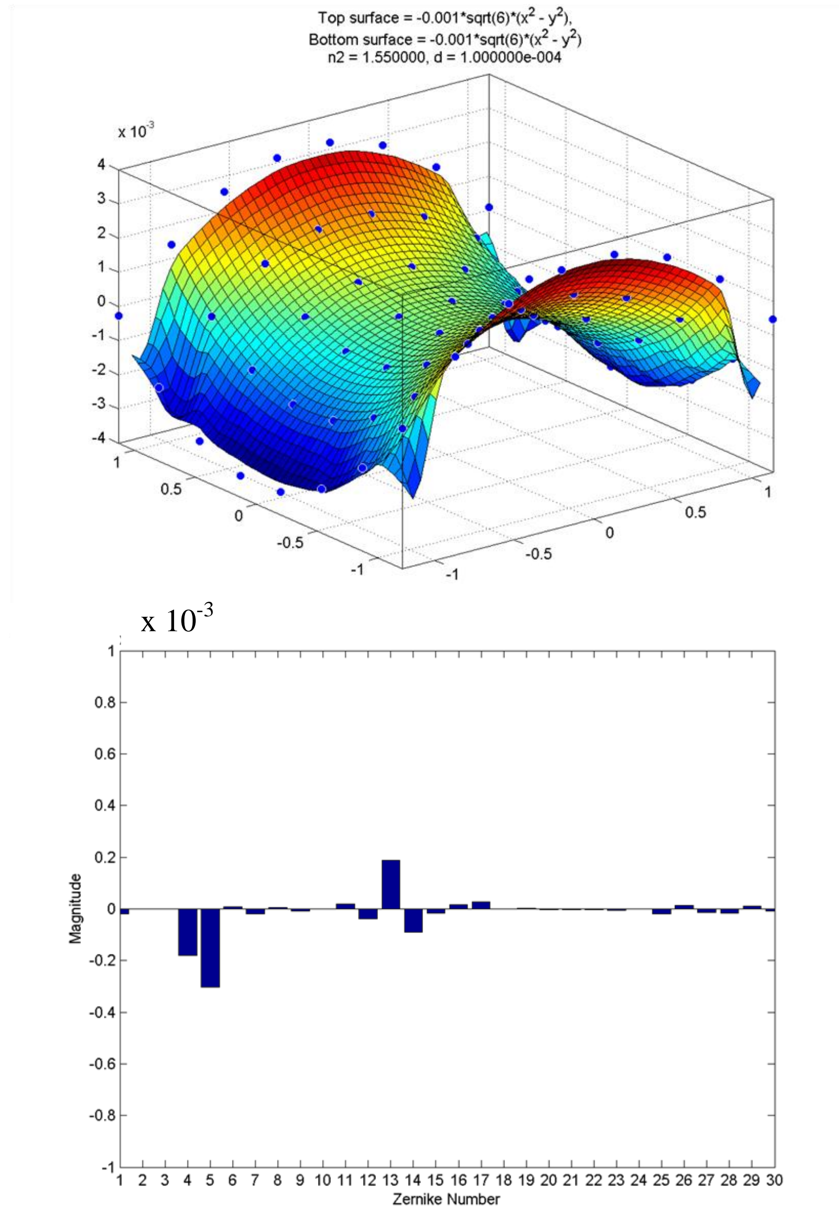

Figure 4.4: **Top and bottom surfaces are Z5 with large coefficients (0.001) and distance between these surfaces are 0.0001 units.**

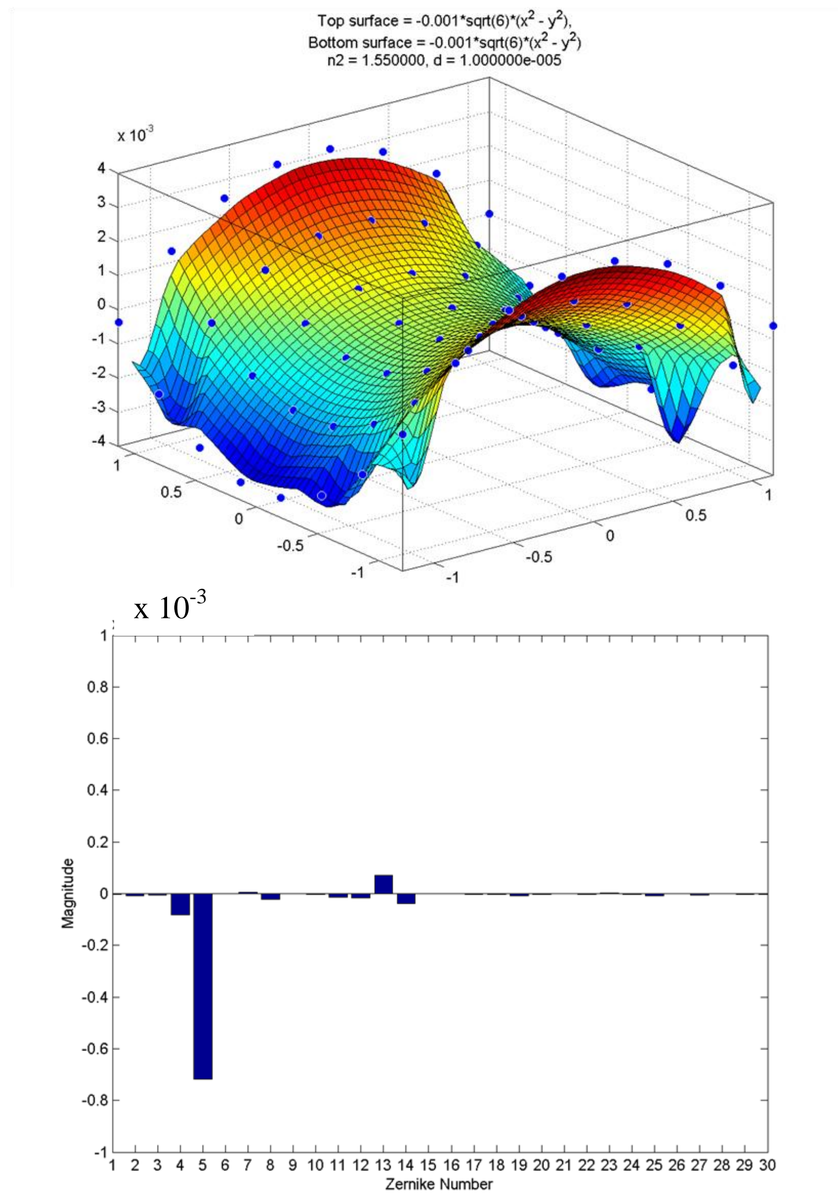

Figure 4.5: Top and bottom surfaces are Z_5 with large coefficients (0.001) and distance between these surfaces are $1x10^{-5}$ units.

Finally, in Figure 4.6, at the smallest thickness of $1x10^{-6}$ units, the magnitude of Z_5 has increased again to approximately $-0.7x10^{-3}$. On the other hand, the magnitude of Z_{13} remains less than $0.1x10^{-3}$.

On both surfaces with larger coefficients (0.001), the deformations of the resultant wavefront have minor changes on every small changes in distances. The extra components which are Z_4, Z_{12}, Z_{13} and Z_{14} appear in each of the results, which slightly affect the shape of the warp. In addition to that, Z_{24}-Z_{27} is also noticed, but with very small magnitudes. It is known that excessive scattering of rays due to higher surface gradients has caused further deviations of the Z_5 in the subsurface wavefront.

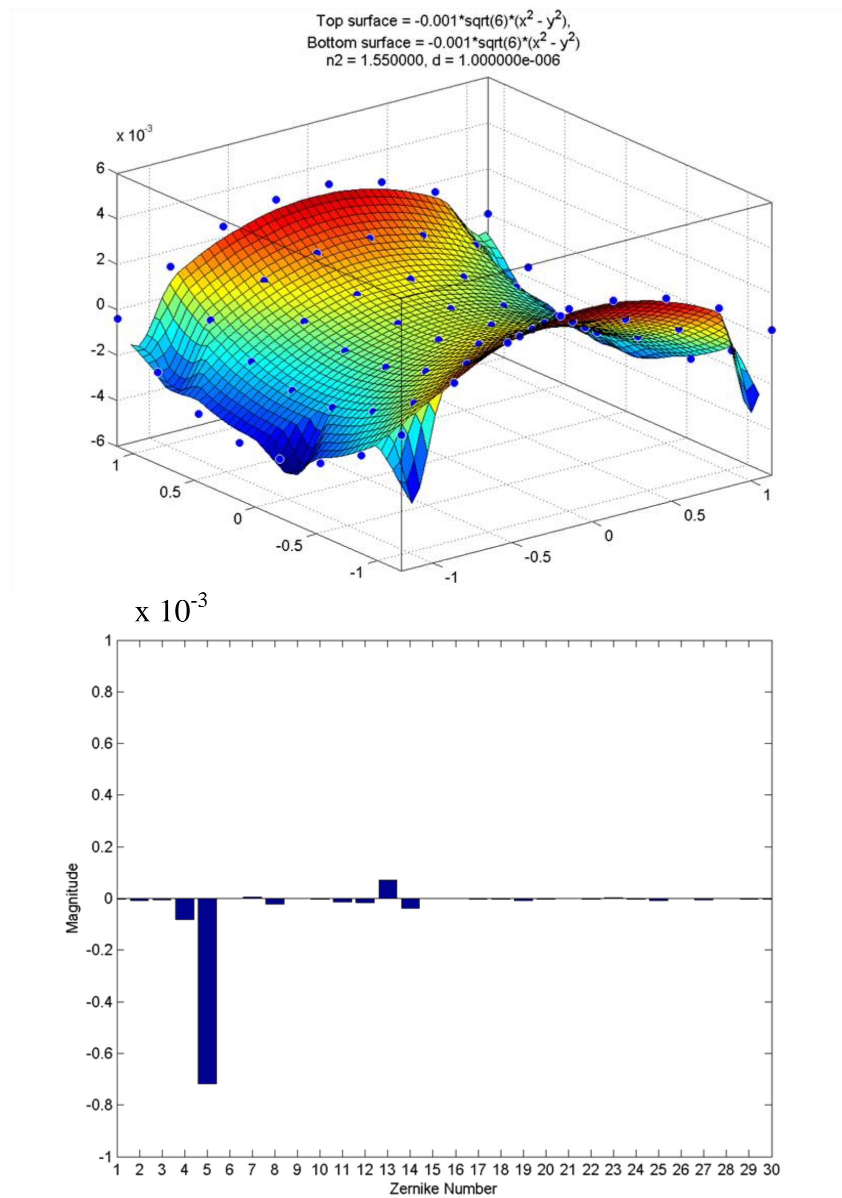

Figure 4.6: Top and bottom surfaces are Z_5 with large coefficients (0.001) and distance between these surfaces are $1x10^{-6}$ units.

The change of distances between the interfaces did affect the Zernikes due to the deviations of the locations of the reflected and refracted rays on the surfaces.

Larger coefficients on surfaces produce larger reflection angles. The reflected ray intersects the top surface much further away from the ray that enters the surface, as mentioned in the following formula. This produces a number of aberrations on lower order Zernikes noticed in the decomposition (Azucena et al., 2010; Kubby, 2013). For example, differentiating the two surfaces $\phi_1 = 0.001Z_5$ and $\phi_2 = 0.000001Z_5$ with respect to x and y, the gradients belonging to ϕ_1 are much greater than the gradients in ϕ_2:

$$\frac{\partial \phi_1}{\partial x} \gg \frac{\partial \phi_2}{\partial x}$$

$$\frac{\partial \phi_1}{\partial y} \gg \frac{\partial \phi_2}{\partial y}$$

Since total internal reflections cannot be computed in this raytracing simulation, the maximum allowable size of the coefficients is up to 0.001 units. As mentioned before, a higher coefficient causes gradients to be larger, and then produces a large angle on the reflected ray. The large angle formed by the reflection coincides with the critical angle, causing the total internal reflection to occur. Therefore, only the coefficients smaller than or equal to 0.001 are chosen in the simulation.

4.2 Identical surfaces (Z_5) with larger coefficients (0.001) and varying refractive indexes

In Figure 4.7 to Figure 4.11, the magnitude of Z_5 increases gradually from $0.5x10^{-3}$ to $0.6x10^{-3}$. Meanwhile the magnitude of Z_{13} decreases in a slow manner, from $0.15x10^{-3}$ to $0.1x10^{-3}$. The magnitude of Z_5 is slightly decreased to $0.58x10^{-3}$ and the magnitude of Z_{13} remains at $0.1x10^{-3}$ which are as shown in Figure 4.12. The rest of the higher order Zernikes from Z_{16} to Z_{30} are with magnitudes less than $0.1x10^{-3}$. In short, the shape of the reflected wavefront does not match the actual shape of the subsurface, for any refractive indexes tested in the simulation

Similarly, as in Section 4.1, larger gradients on surfaces produce larger reflection angles, which results to more scattering on the subsurface. This produces a number of lower order Zernikes noticed in the decomposition. However, the changes of the refractive indexes in the material has provided small linear changes to the distortions in the decomposition. It is because both top and bottom surfaces are identical and the plain surfaces of Z_5 which do not allow the rays to scatter too far ahead between the interfaces.

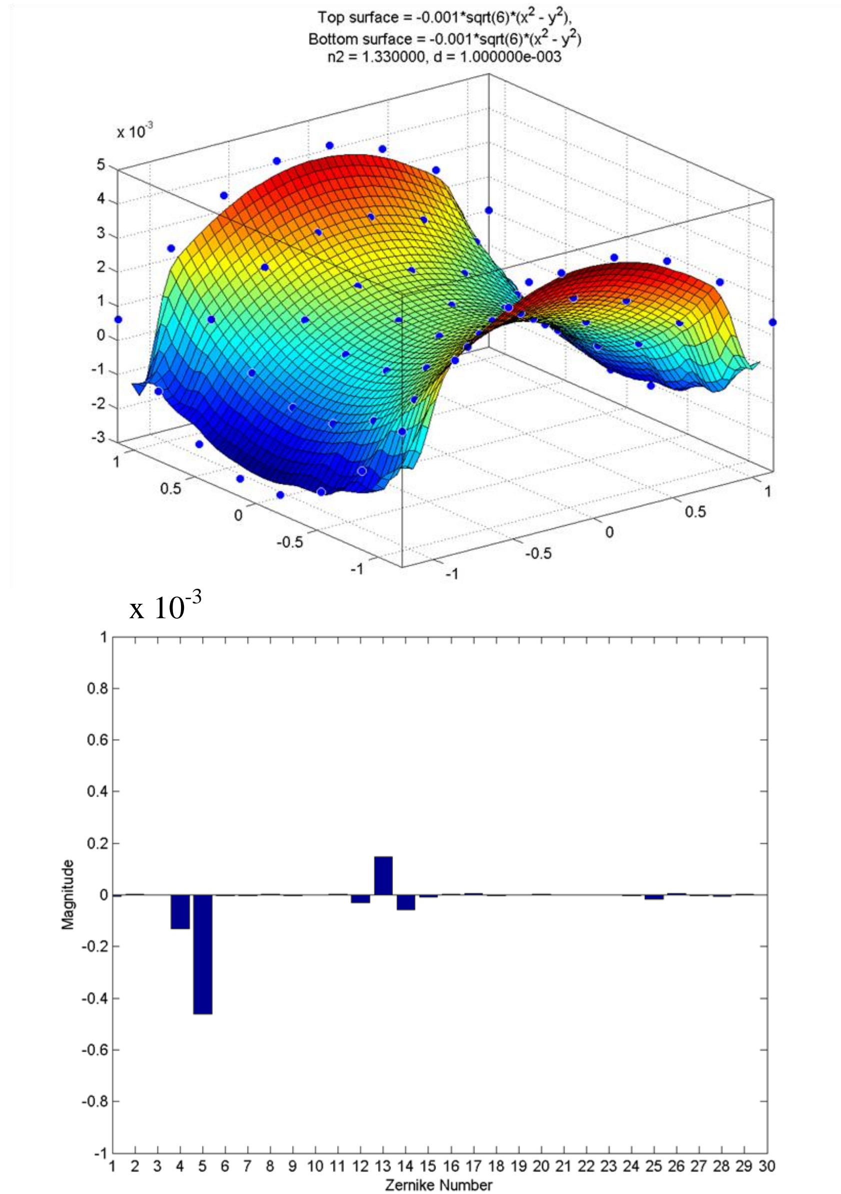

Figure 4.7: Top and bottom surfaces are Z5 with large coefficients (0.001), distance between the interfaces is fixed at $1x10^{-3}$ units and refractive index of the material is 1.33.

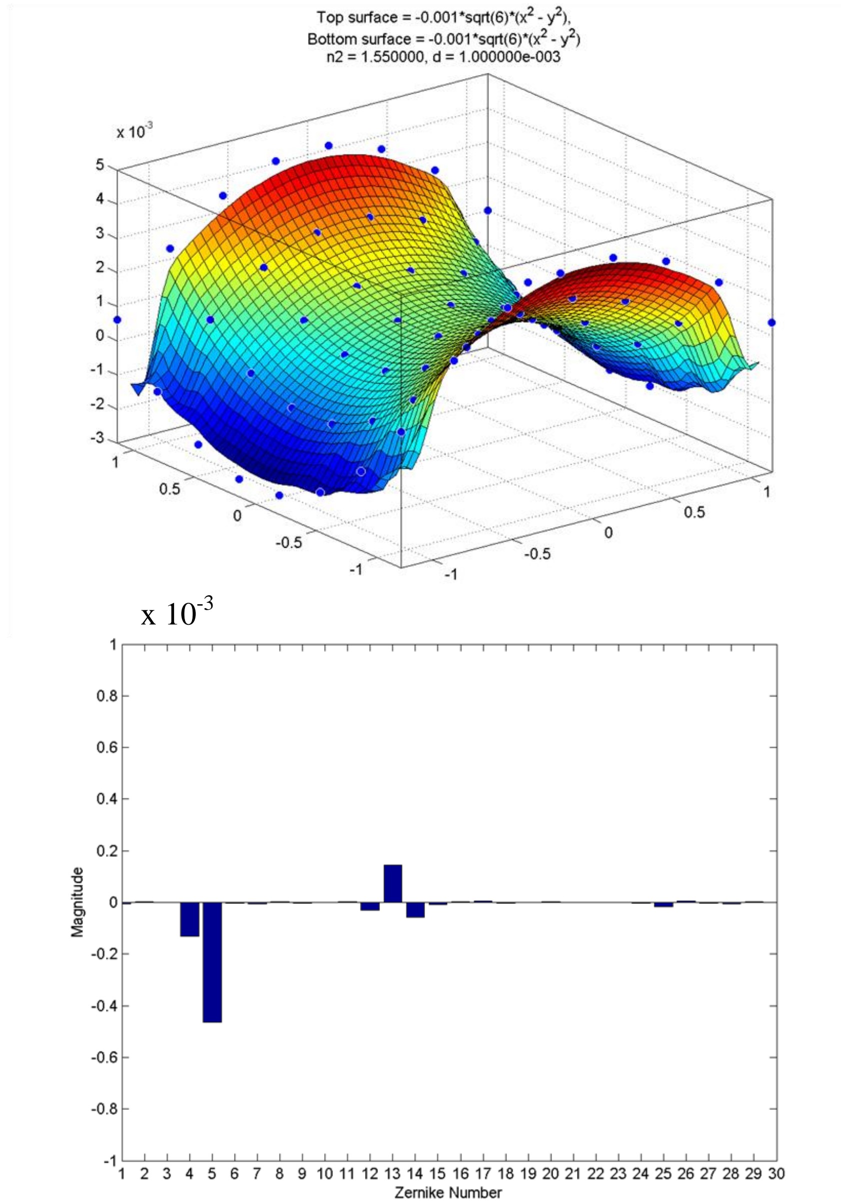

Figure 4.8: Top and bottom surfaces are Z5 with large coefficients (0.001), distance between the interfaces is fixed at $1x10^{-3}$ units and refractive index of the material is 1.55.

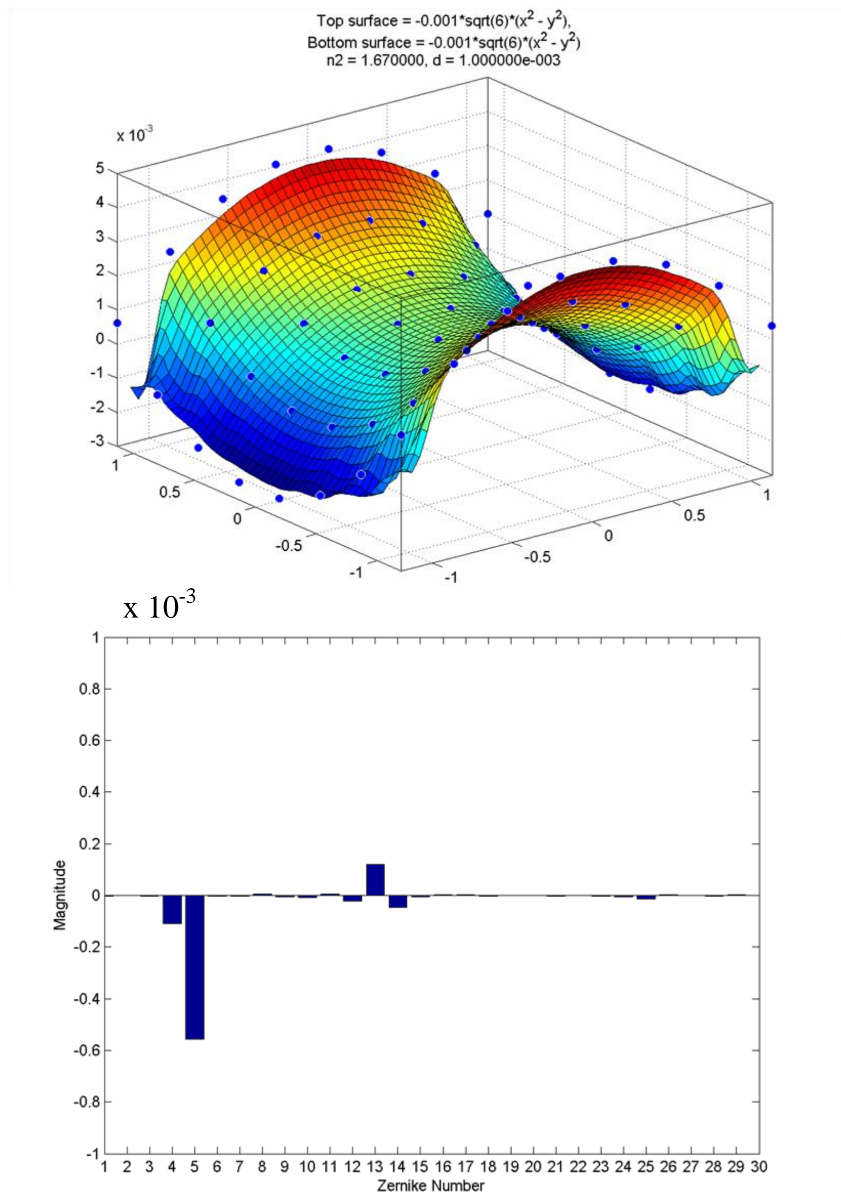

Figure 4.9: Top and bottom surfaces are Z5 with large coefficients (0.001), distance between the interfaces is fixed at $1x10^{-3}$ units and refractive index of the material is 1.67.

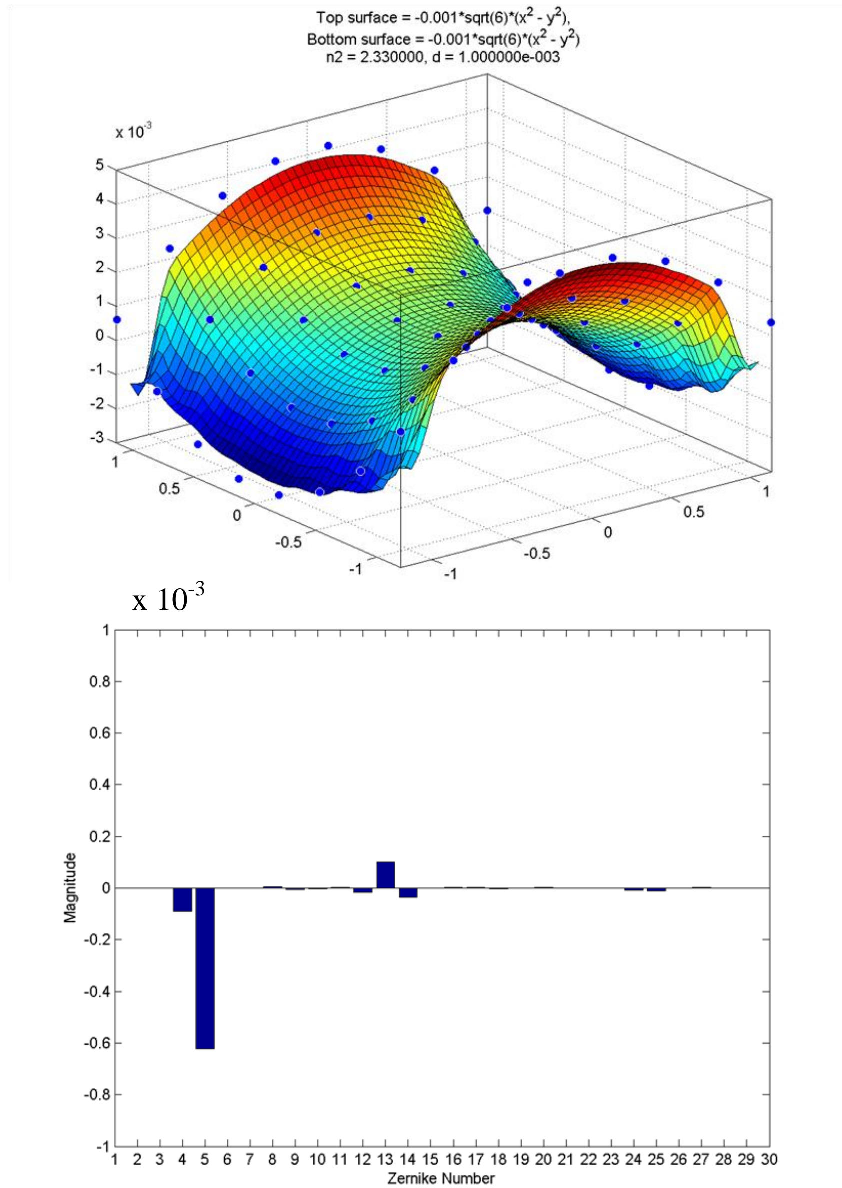

Figure 4.10: Top and bottom surfaces are Z5 with large coefficients (0.001), distance between the interfaces is fixed at $1x10^{-3}$ units and refractive index of the material is 2.33.

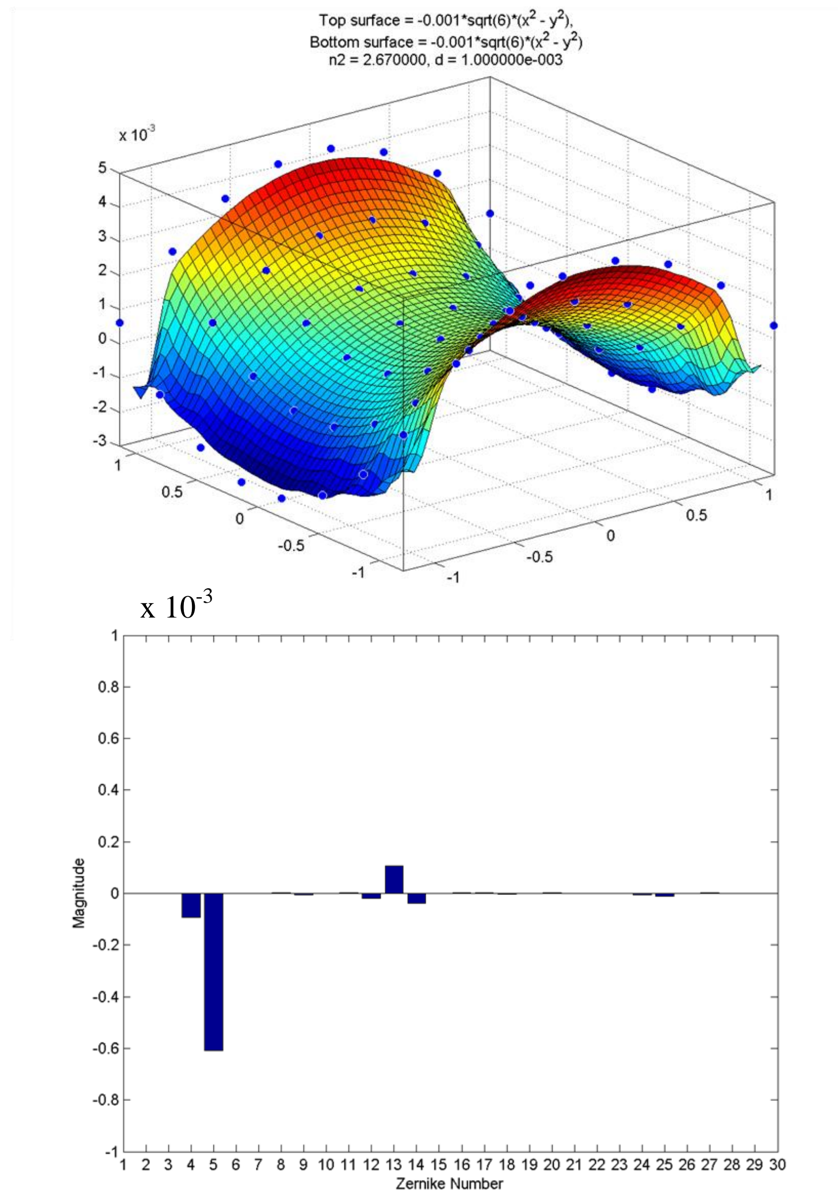

Figure 4.11: Top and bottom surfaces are Z5 with large coefficients (0.001), distance between the interfaces is fixed at $1x10^{-3}$ units and refractive index of the material is 2.67.

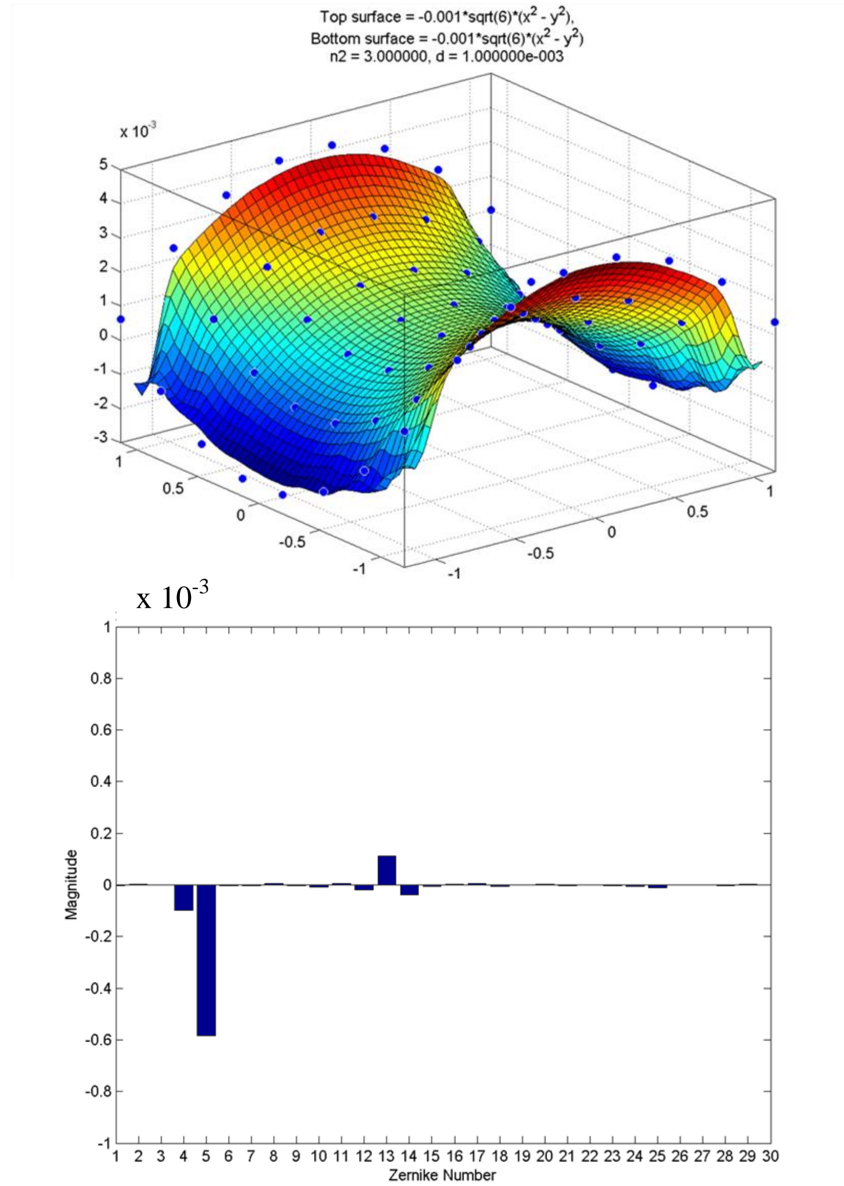

Figure 4.12: Top and bottom surfaces are Z5 with large coefficients (0.001), distance between the interfaces is fixed at 1×10^{-3} units and refractive index of the material is 3.00.

4.3 Identical surfaces (Z_5) with different coefficients for the bottom surface.

On smaller gradients on those surfaces, changes of the coefficients of the bottom surface do only affect the Zernikes coefficients in a very small quantity, as shown in Figure 4.13. However, the reflected wavefront does not match the actual surface, which its magnitude is slightly more than $1x10^{-6}$. Z_4 and Z_{13} exists in very small magnitudes, while the other higher order components are present in minute quantities.

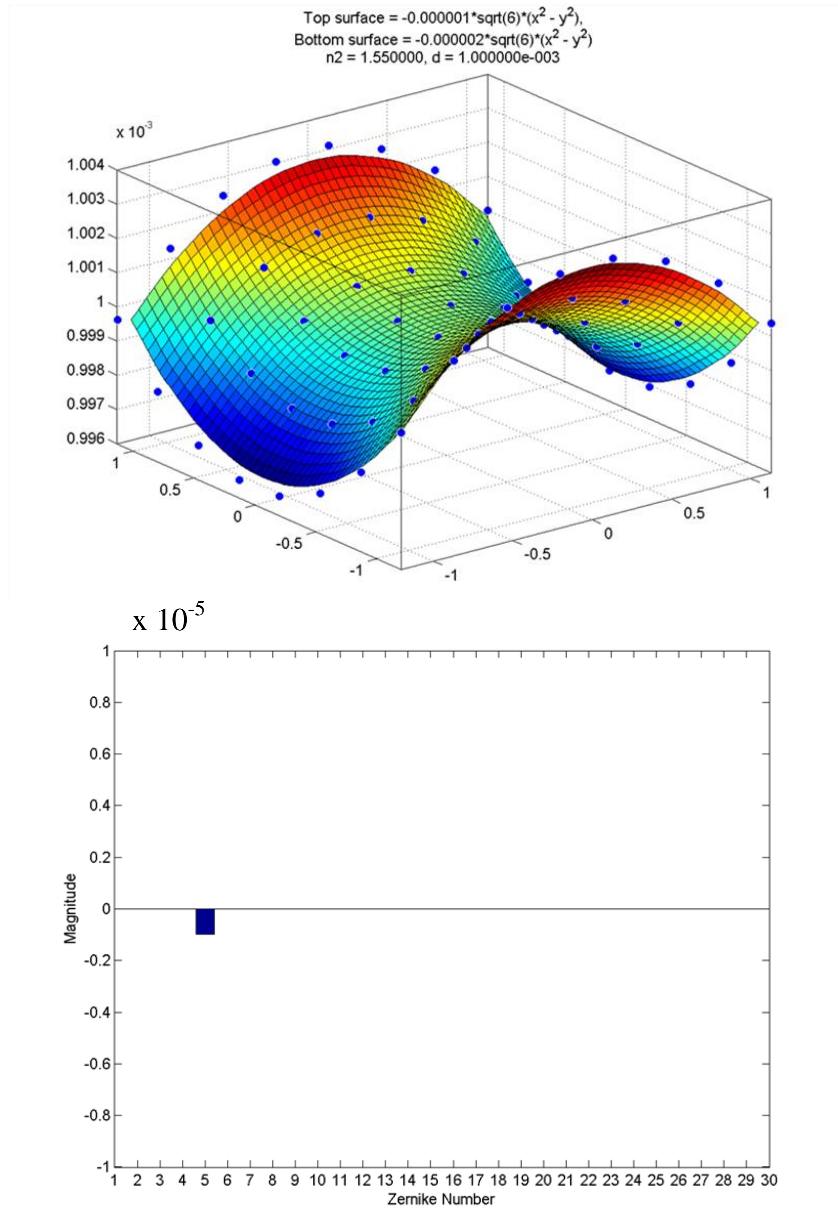

Figure 4.13: Top and bottom surfaces are Z5. Top surface coefficient is 0.000001, while the coefficient of the bottom surface is 0.00002. The refractive index is 1.55 and the distance between the interfaces is 0.001.

4.4 Identical surfaces (Z_5) with both small coefficients (0.000001) and with varying distances.

Similarly, for Figure 4.14, changing the distances between the interfaces do not change much of the shape of the reflected wavefront. However, the wavefront matches the actual subsurface, which is $-1x10^{-6}Z_5$. On a warp with an entirely smooth surface, a very small coefficient does not cause the rays to scatter too far away which leads to further distortion of the reflected subsurface wavefront. In actual rugged surfaces, scattering of rays on these is not uncommon and will result to many traces of lower-order Zernike components to be detected in the decomposition after the wavefront has been reflected from the subsurface.

The very small gradients and the plain surfaces do not cause the rays to scatter excessively and hence the reflected subsurface wavefront is mainly unaltered.

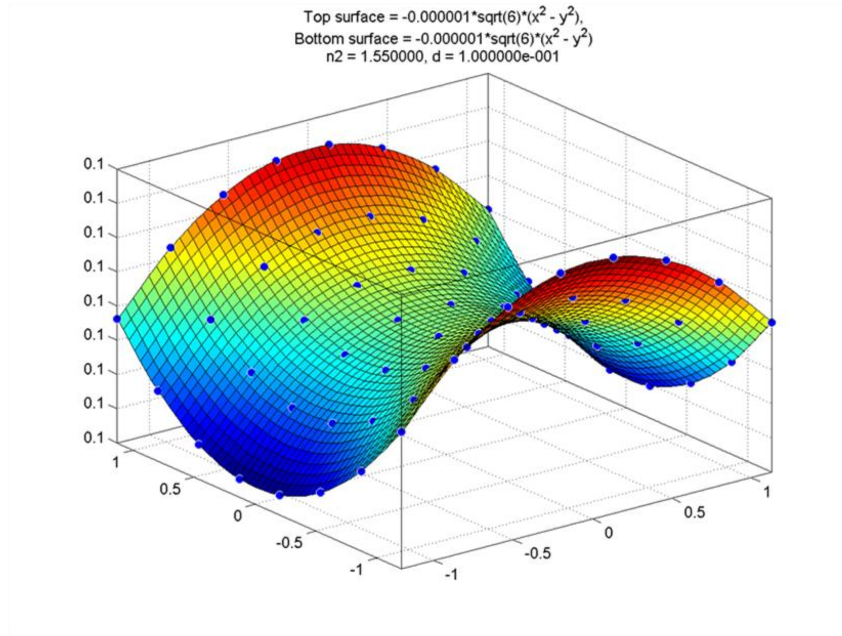

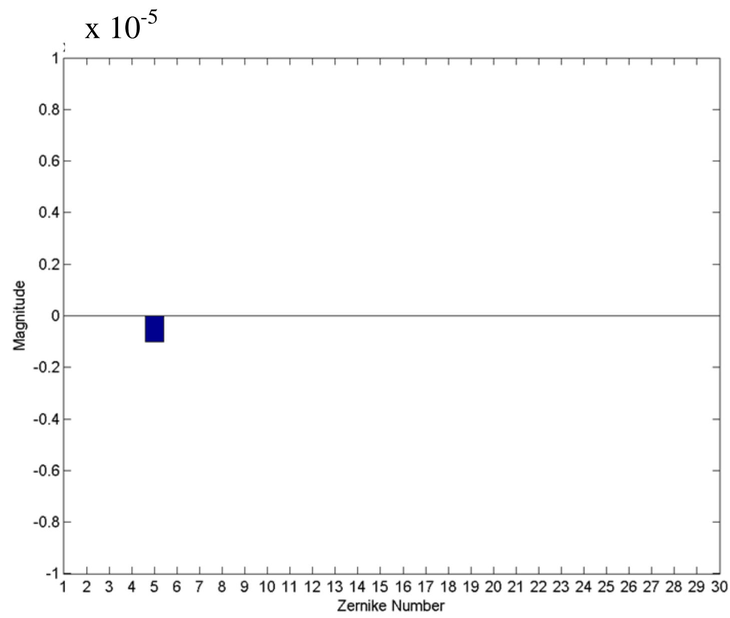

Figure 4.14: Top and bottom surfaces are Z_5 with coefficients of 0.000001. The refractive index is 1.55 and the distance between the surfaces is 0.1 units.

4.5 Identical surfaces (Z_5) with both small coefficients (0.000001), fixed distance but with varying refractive indexes.

In Figure 4.15, changing the refractive indexes with very small coefficients on the surfaces does not affect much of the reflected subsurface wavefront at all. Very small magnitudes of the other higher order Zernike appears together with the peak of Z_5. The magnitude of the peak of Z_5 measured in the decomposition is slightly less than the actual shape of the subsurface. Similarly, more scattering of the rays occurs when the surface measured is rugged in nature.

Similarly, very small gradients do not affect the reflected subsurface wavefront as scattering is at its minimal.

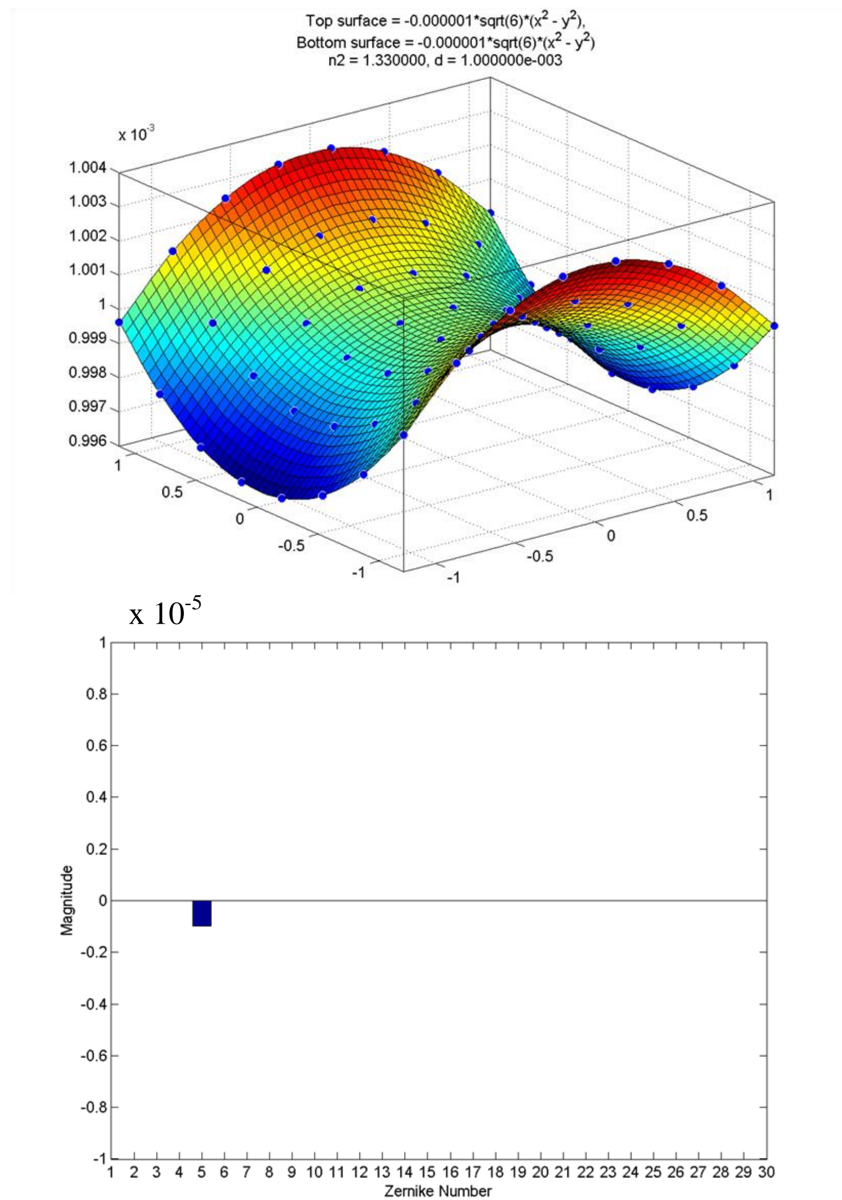

Figure 4.15: Both of the surfaces are Z_5 and distance between the surfaces is $1x10^{-3}$. The change of refractive indexes does not affect the reflected wavefront.

4.6 Identical surfaces ($Z_5 + Z_7 + Z_8$) with both small coefficients (0.000001) with varying distances between interfaces.

In distances between interfaces of $1x10^{-1}$, $1x10^{-2}$ and $1x10^{-3}$ units in Figures 4.16 to 4.18, the changes of the magnitudes of the Zernikes are minimal. However, other extra components occur alongside Z_5, Z_7 and Z_8, and all of these do not match the actual surface. As the distances becomes smaller (from $1x10^{-4}$ units onwards), some of the components have changed magnitudes in a drastic manner, while the magnitudes of the higher order Zernikes have a marginal increase, which are as shown in Figures 4.19 to 4.21.

Distance between the interfaces has influences on the spurious modes formed in the composition due to the reflected subsurface rays intersecting different areas of the top surface. A complex surface may result into more scattering and deviations of rays, which then leads to a more deformed wavefront.

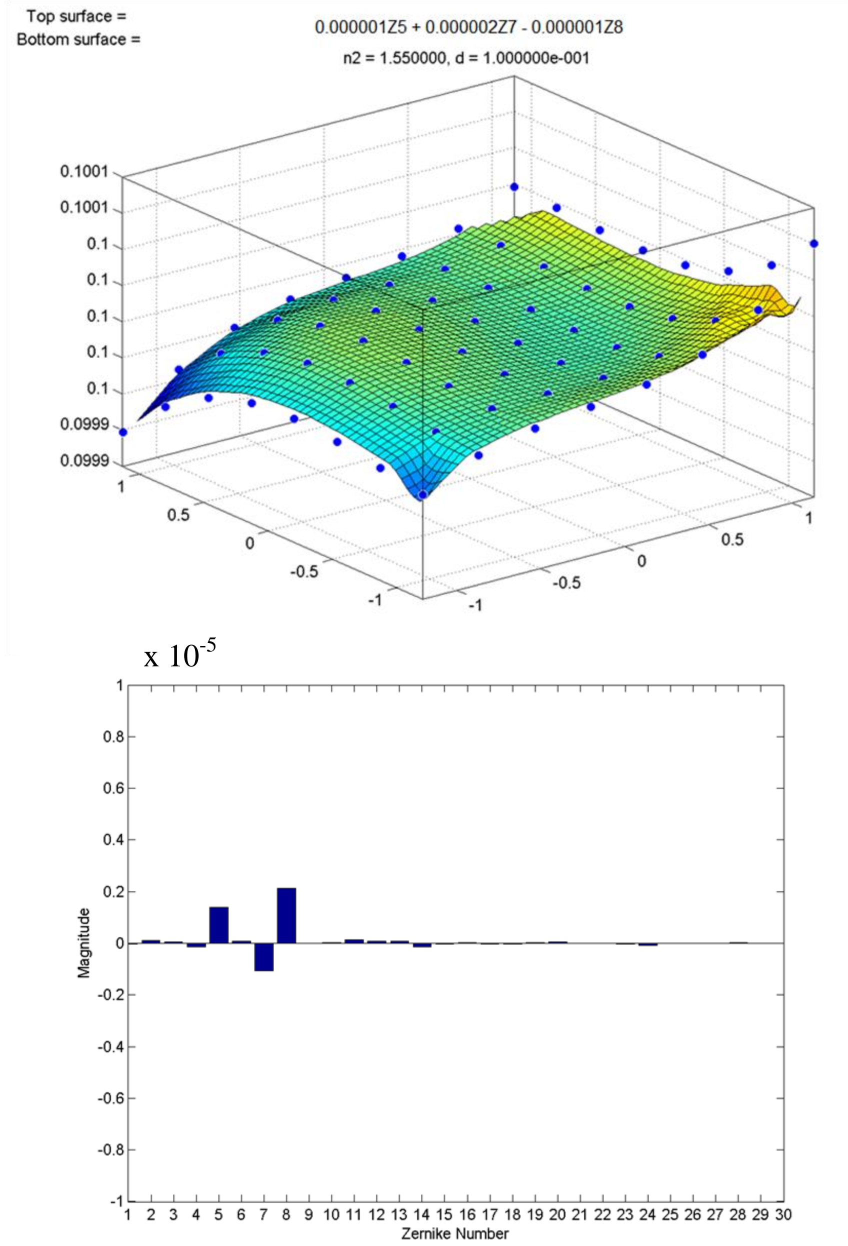

Figure 4.16: Both of the surfaces are $Z_5 + Z_7 + Z_8$ and distance between the surfaces is $1x10^{-1}$.

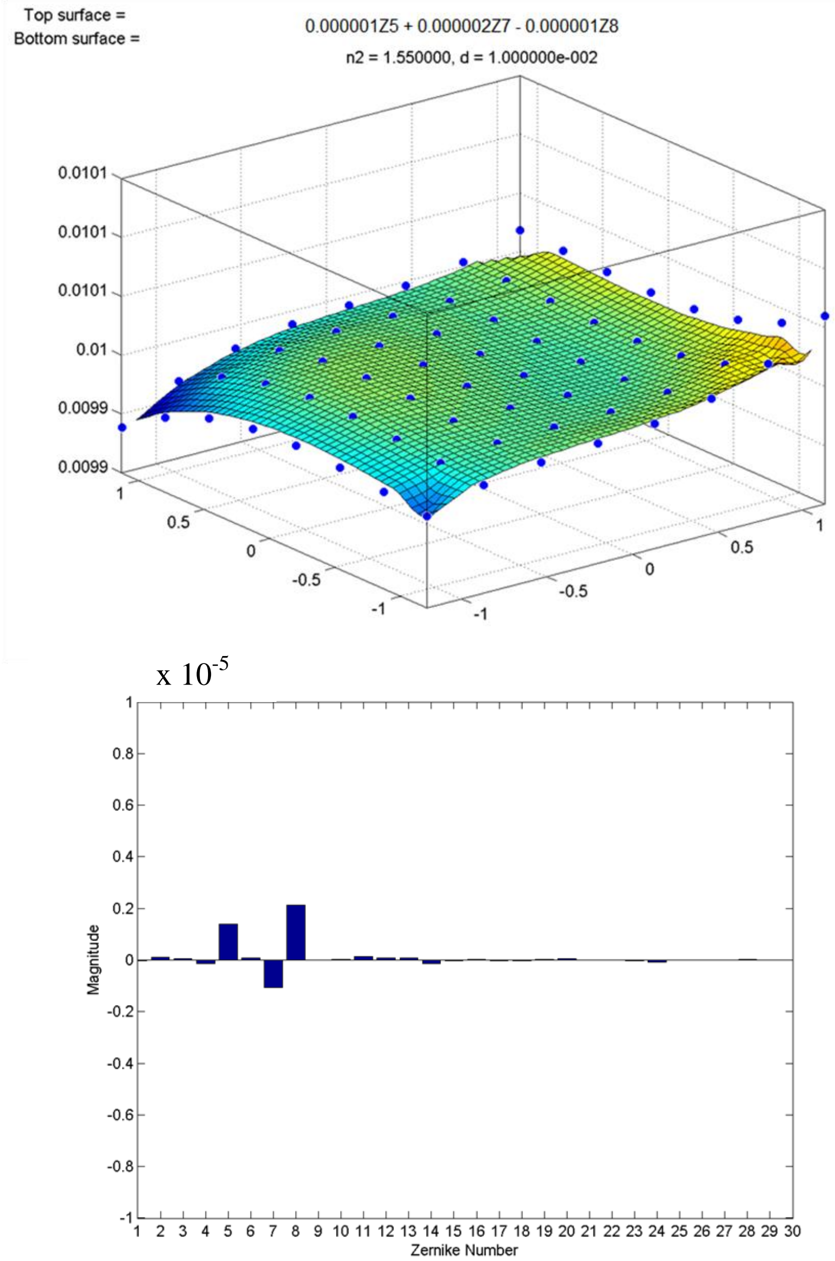

Figure 4.17: Both of the surfaces are $Z_5 + Z_7 + Z_8$ and distance between the surfaces is $1\text{x}10^{-2}$.

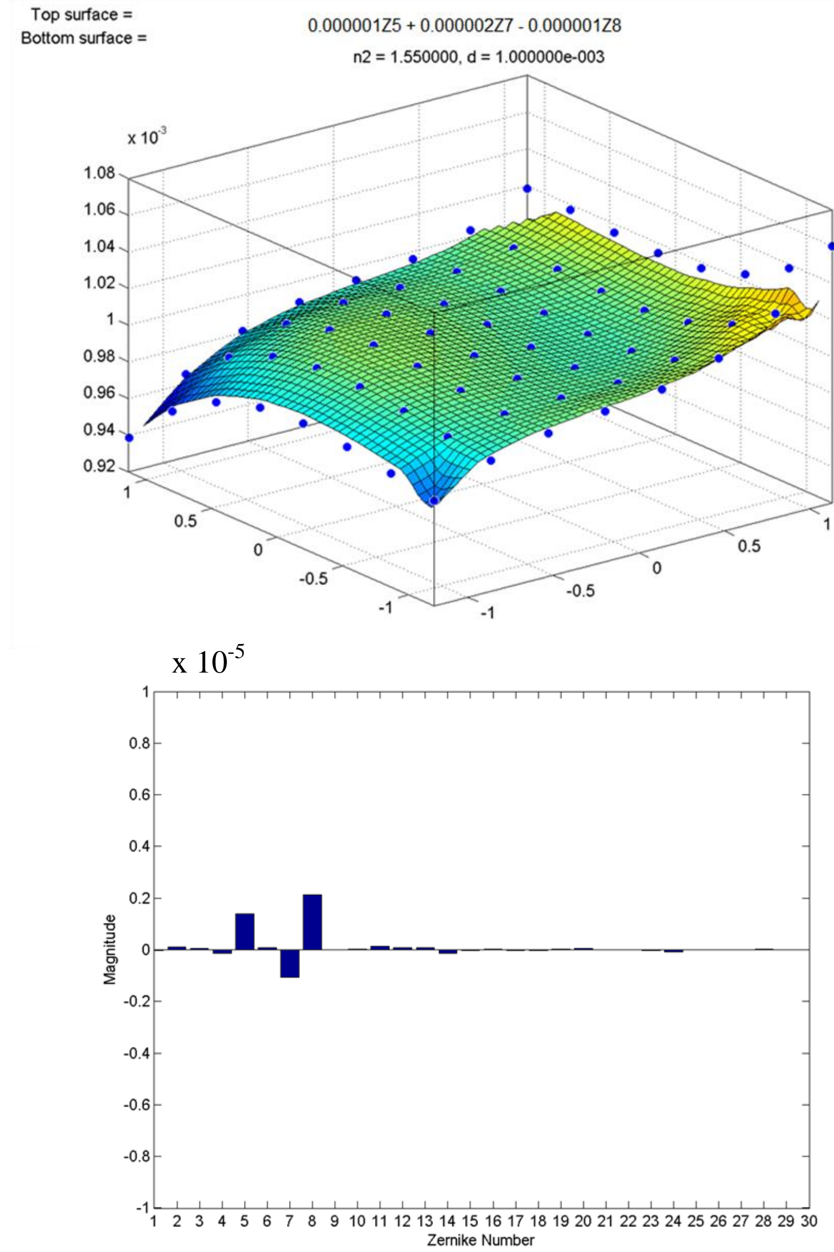

Figure 4.18: Both of the surfaces are $Z_5 + Z_7 + Z_8$ and distance between the surfaces is $1x10^{-3}$.

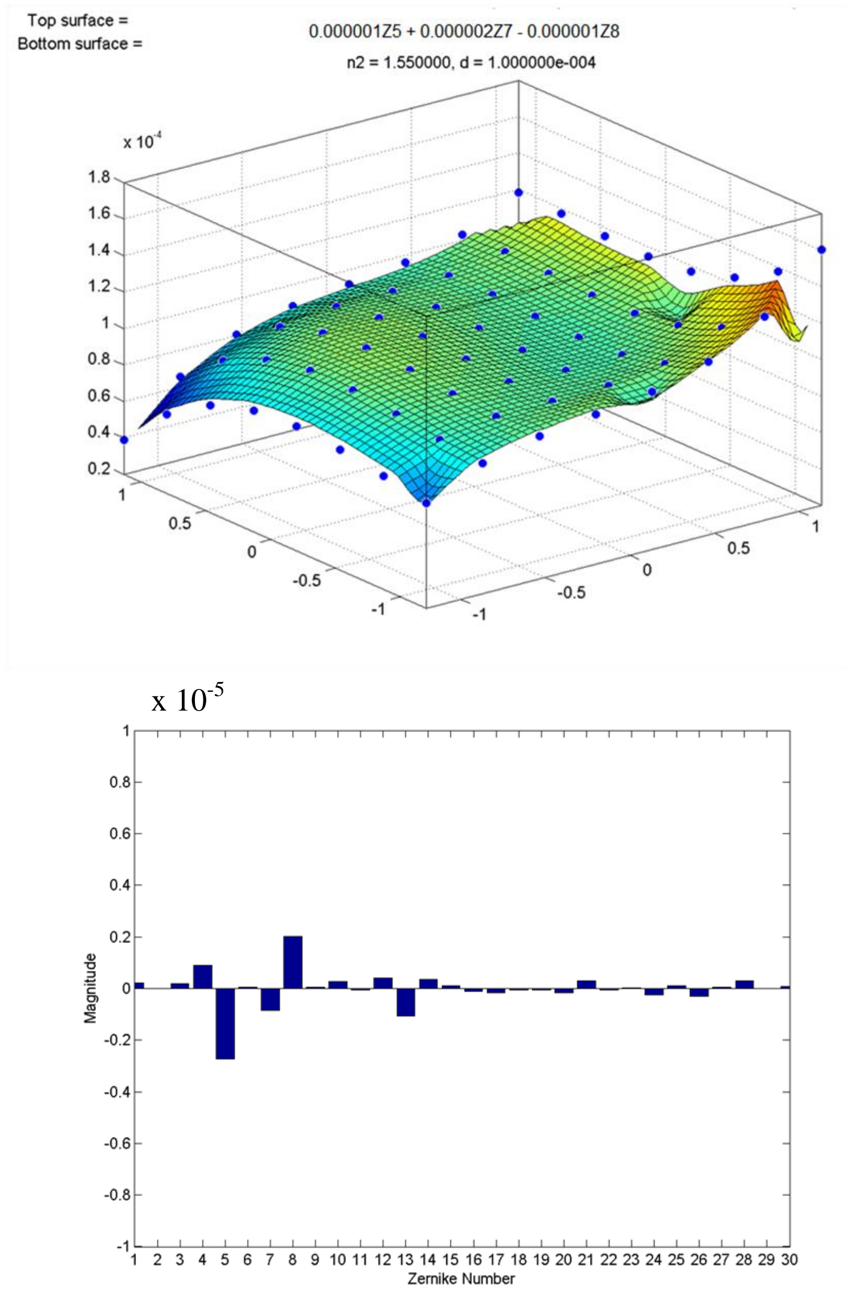

Figure 4.19: Both of the surfaces are $Z_5 + Z_7 + Z_8$ and distance between the surfaces is $1x10^{-4}$.

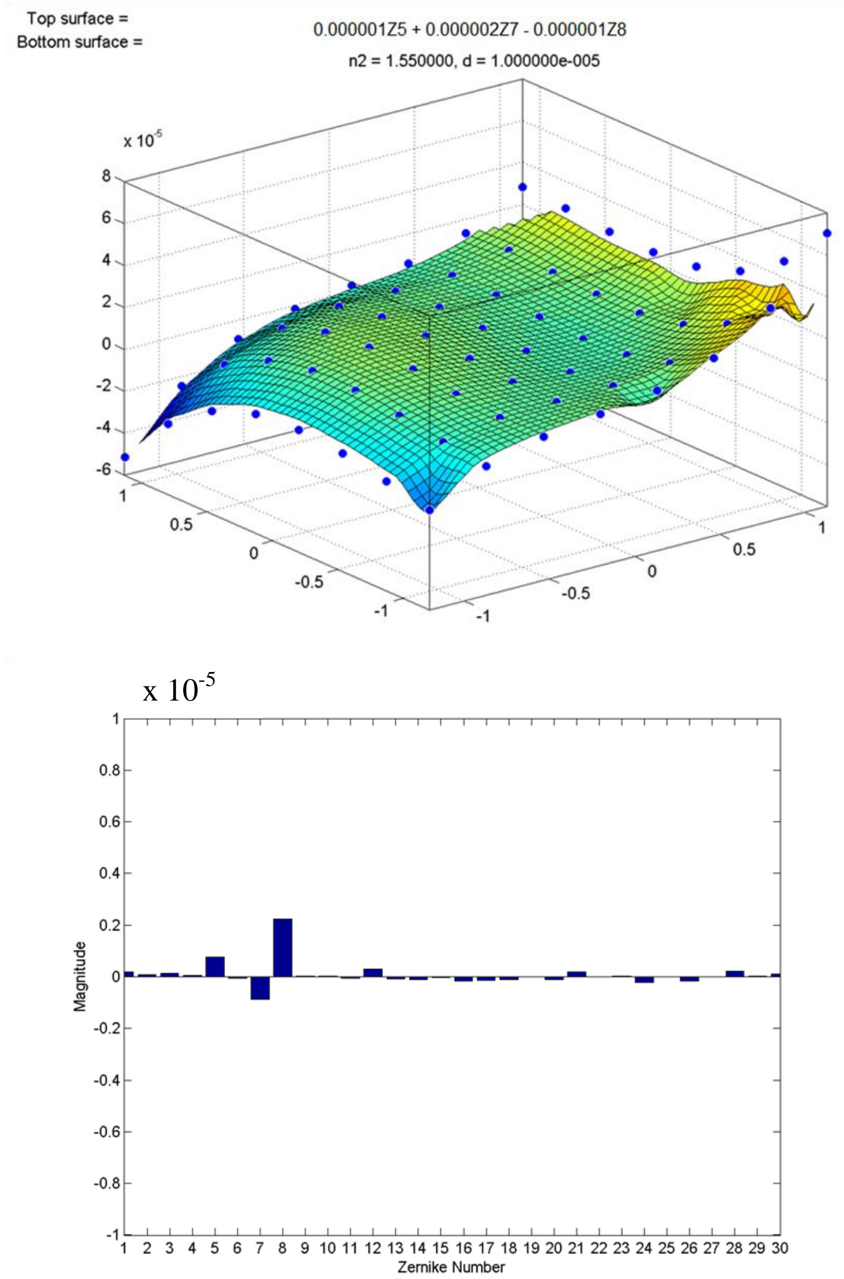

Figure 4.20: Both of the surfaces are $Z_5 + Z_7 + Z_8$ and distance between the surfaces is $1\text{x}10^{-5}$.

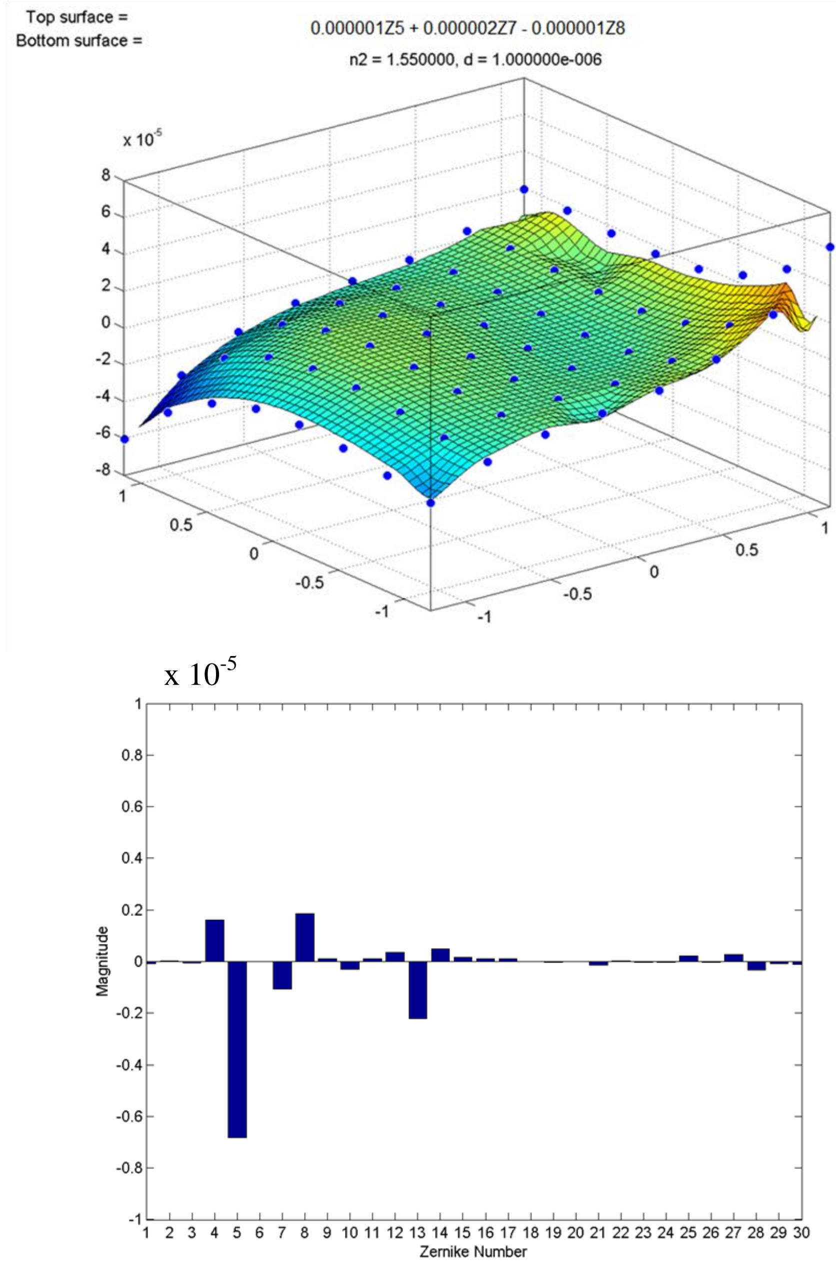

Figure 4.21: Both of the surfaces are $Z_5 + Z_7 + Z_8$ and distance between the surfaces is $1x10^{-6}$.

4.7 Identical surfaces ($Z_5 + Z_7 + Z_8$) with both small coefficients (0.000001), but with varying refractive indexes.

For surfaces of $-0.000001Z_5 + 0.000002Z_7 - 0.0000001Z_8$ in Figure 4.22, changes of refractive indexes only introduces extremely small changes in the Zernike decomposition. This wavefront contains Z_5, Z_7 and Z_8, but with different magnitudes. The Z_7 is negative while Z_8 is positive in the chart. Other lower order Zernikes are found at the vicinities of the three main Zernikes in smaller magnitudes. Also, higher order Zernikes are noticed but these are much smaller than the lower order polynomials.

Due to the more complex surface which is a combination of a few Zernike polynomials, the scattering of the rays are much more noticeable even on very small gradients on surfaces. Hence, more spurious modes are detected in the decomposition.

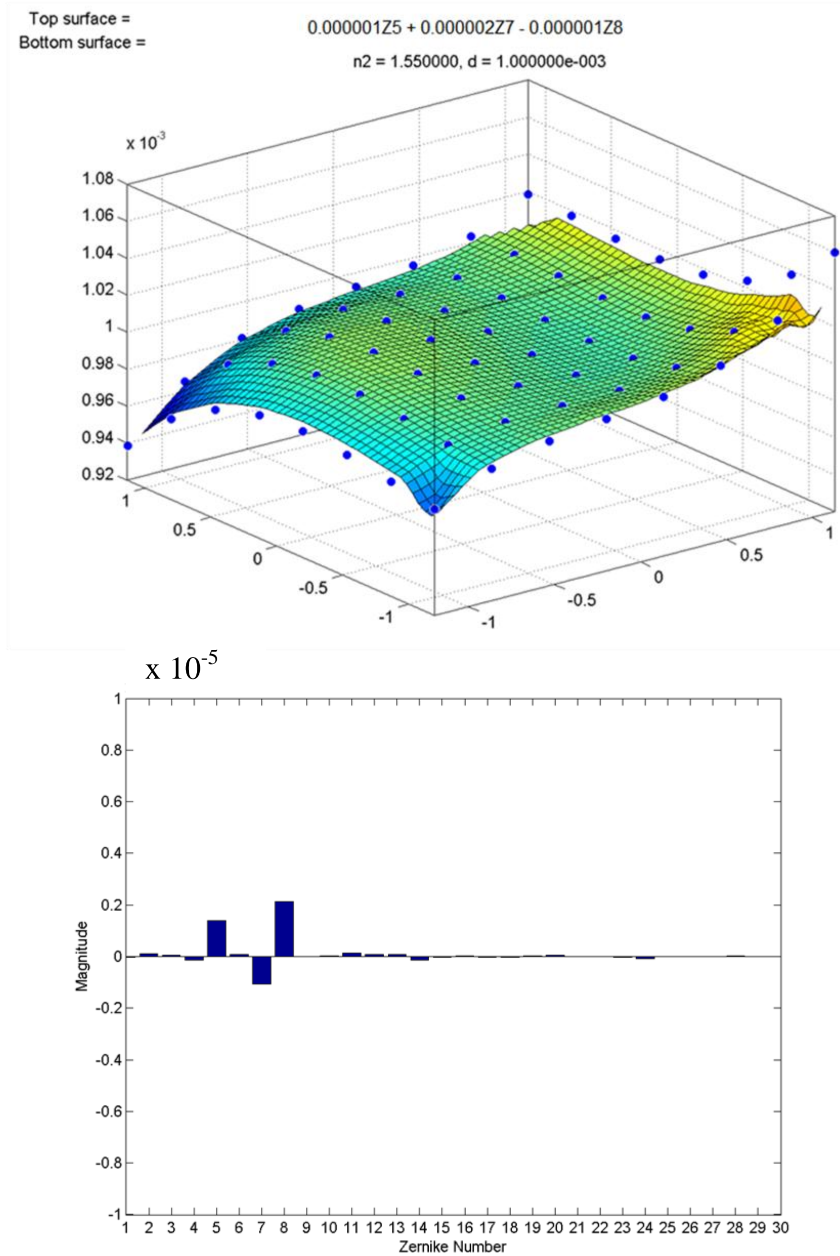

Figure 4.22: Both of the surfaces are $Z_5 + Z_7 + Z_8$ and distance between the surfaces is $1x10^{-3}$.

4.8 Different surfaces and its combinations with small coefficients (0.000001)

On a material with different surfaces, such as Z_3 and Z_6, in Figure 4.23, many other Zernike components are noticed but with very small magnitudes. The Z_3 and Z_5 are predominant in the exit wavefront, while other components such as Z_{13} to Z_{14} are also significant.

With a top surface of Z_6 and the subsurface being Z_{10} which is as shown in Figure 4.24, the reflected and refracted wavefront from the subsurface only resembles Z_6 and other distortions of a relatively lower magnitudes are noticed alongside. Also in the wavefront, some lower order components such as Z_5, Z_7, and Z_9 which the coefficients are less than 0.1×10^{-6}.

In Figure 4.25, a combination of two Zernike surfaces $Z_5 + Z_7$, on both upper and lower surfaces, the quantity of the Z_5 is more noticeable than the Z_7, while higher order components from Z_{16} to Z_{30} exist in small magnitudes.

A mixture of high-order Zernikes alongside with lower magnitude low-order Zernikes forms a rough and a rugged surface, as shown in Figure 4.26. Lower and higher order Zernikes are scattered around the highest peak which belongs to Z_5. Most of the other Zernikes are with the average magnitudes of less than 0.05×10^{-3}.

A decomposition of a surface with a more rugged texture, a combination of more Zernike functions with different values of coefficients are be noticed. For a simpler surface without much of the texture, the decomposition will return only a few coefficients which are 15 or less.

Due to the effects of the curvature of the subsurface and the differences of refractive index between the interfaces, the lower order Zernikes are significant in the outgoing wavefront (Azucena et al., 2010; Kubby, 2013). Not much higher order Zernikes are noticed in the wavefront because the surfaces are without aberrations and only very basic flat surfaces are simulated. Plus, the surfaces in the simulation are in analytical form. Compared to the lower order polynomials, these magnitudes of the Zernikes are much lower.

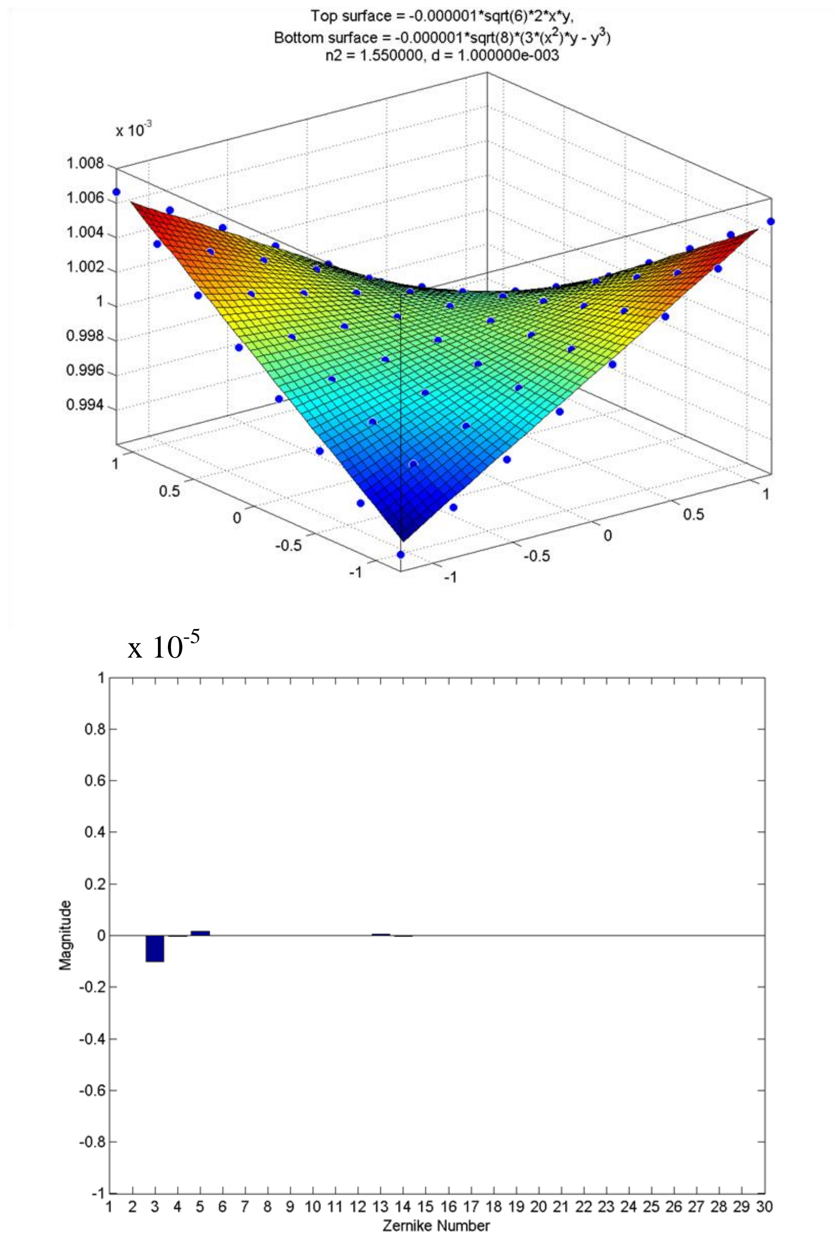

Figure 4.23: Top surface is Z_3 while the bottom surface is Z_6. The refractive index is 1.55 and the distance between the surfaces is $1x10^{-3}$ units.

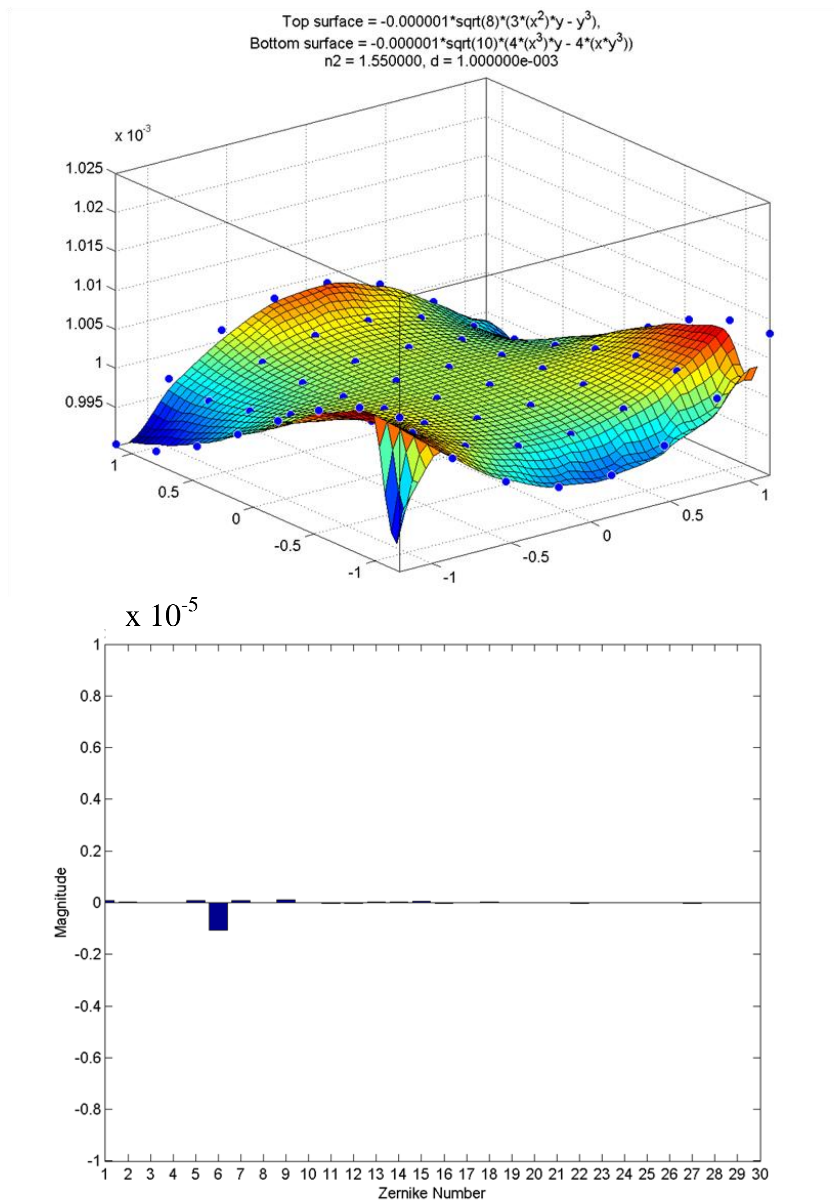

Figure 4.24: Top surface is Z_6 while the bottom surface is Z_{10}. The refractive index is 1.55 and the distance between the surfaces is $1x10^{-3}$ units.

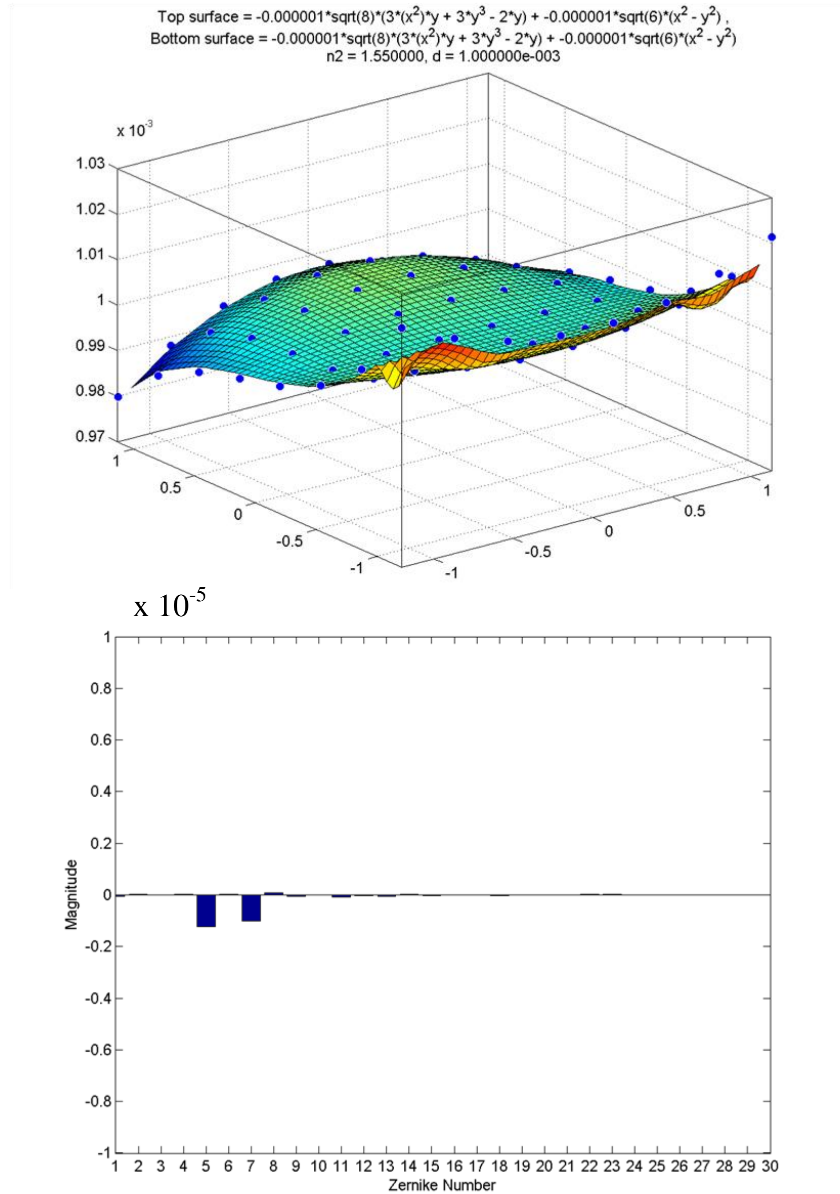

Figure 4.25: Top and bottom surfaces are Z_5 + Z_7 with coefficients of 0.000001. The refractive index is 1.55 and the distance between the surfaces is $1x10^{-3}$ units.

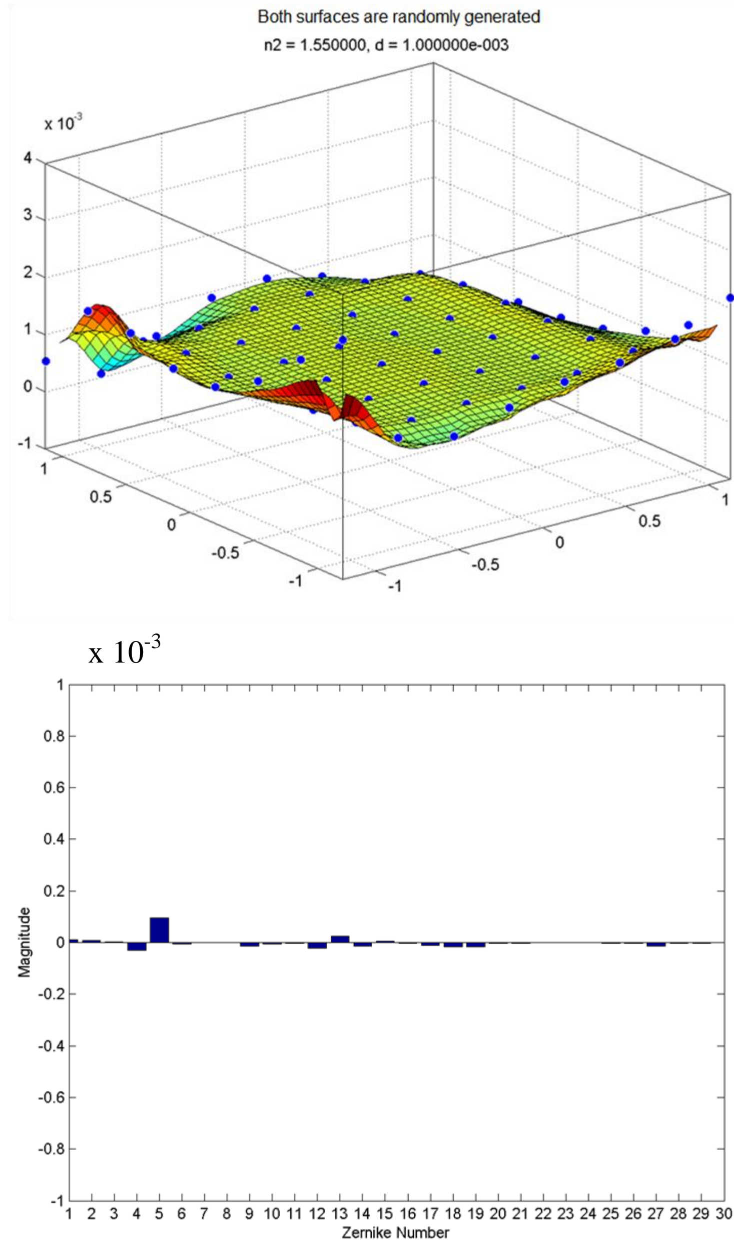

Figure 4.26: Top and bottom surfaces are randomly generated surfaces. Distance between the surfaces is $1x10^{-3}$ units and the refractive index is 1.55.

CHAPTER 5

CONCLUSIONS AND FURTHER WORK

A simulation of a short laser pulse traversing between two interfaces in a material block in three dimensions has been successfully developed by using Matlab. Vector raytracing methods are employed to compute the behaviour of the laser pulse in the simulation. The reflected rays from the subsurface are then interpolated into a wavefront. The Zernike Decomposition is used to analyse the wavefront by breaking down the wavefront into a number of coefficients. The matrices in the decomposition is solved using Singular Value Decomposition (SVD) as the matrices are mainly rank-deficient. From the decomposition, it is known that wavefronts which traverse between two interfaces are known to be deformed due to the reflection from the sub-surface and the different refractive index between the interface of the material. The amount of deformations and aberrations are noticed in the wavefront through the coefficients obtained from the decomposition. From the coefficients, it is known that different refractive indexes, distance between the interfaces and size of gradients on the surfaces do affect the shape of the reflected subsurface wavefront in three dimensions. Larger gradients on the surfaces will severely distort the reflected wavefront due to the large reflection angles on the subsurface. Meanwhile, smaller gradients on the surfaces produce minimal levels of distortions due to the small reflection angles of the subsurface.

Complex surfaces on a material introduce more scattering of the reflected rays in a random manner which produces a mixture of lower and higher order Zernikes in the decomposition.

Further work will include simulation of wavefront traversing between three or more interfaces and the correction of the distorted outgoing wavefront. More sampling points will be used in the simulation and thus increasing the resolution and details of the wavefront. Also, non-analytical surfaces will be simulated as actual wafer surface has varying degrees of roughness in micron levels and aberrations in macro levels. Finally, a combination of Fast Fourier Transform (FFT) and Zernike decomposition will provide more understanding of the deformation and to facilitate the process of correcting the subsurface wavefront. Other methods of Zernike decomposition using different aperture sizes such as rectangle, ellipse and hexagon, are also investigated in the future work.

REFERENCES

Armitage, D. U., I. and Wu, S. T., 2006. *Introduction to Microdisplays*, John Wiley & Sons, Ltd.

Azucena, O. et al., 2010. Wavefront aberration measurements and corrections through thick tissue using fluorescent microsphere reference beacons. *Optics Express*, 18(6), pp. 17521-17532.

Mejía-Barbosa, Y. and Malacara-Hernández, D., 2001. A Review of Methods for Measuring Corneal Topography. *Optometry and Vision Science*, 78(4), pp 240-253.

Bentell, J. et al., 2007. Flip Chipped INGaAs Photodiode Arrays for Gated Imaging with Eye-Safe Lasers. *Solid-State Sensors, Actuators and Microsystems Conference, 2007. TRANSDUCERS 2007*, 10-14 June 2007. Lyon, France, pp. 1103-1106

Blunt, L. and Jiang, X., 2003. Advanced techniques for assessment surface topography: Development of a Basis for 3D Surface Texture Standards "SURFSTAND", Kogan Page Science.

Blunt, R. T. 2006., White Light Interferometry – a production worthy technique for measuring surface roughness on semiconductor wafers, *CS MANTECH Conference,* April 24-27, 2006. Vancouver, British Columbia, Canada, pp. 59-62

Brezinski, M. 2006., *Optical Coherence Tomography: Principles and Applications*, Academic Press.

Campbell, H. I. and Greenaway, A. H., 2006. Wavefront Sensing: From Historical Roots to the State-of-the-Art. *Astronomy with High Contrast Imaging III: Instrumental Techniques, Modeling and Data Processing*, 22, pp. 165-185.

Cessou, A., Meier, U. and Stepowski, D., 2000. Applications of planar laser induced fluorescence in turbulent reacting flows. *Meas. Sci. Technol.,* 11, pp. 887-901.

Chang, S., Mao, Y. and Flueraru, C., 2011. Dual-Source Swept-Source Optical Coherence Tomography Reconstructed on Integrated Spectrum. *International Journal of Optics, 2012*, pp. 1-6.

Chen, C. C., Lee, D. J., Pollock, T. and Whitaker, J. F., 2010. Pulsed-terahertz reflectometry for health monitoring of ceramic thermal barrier coatings. *Optics Express,* 18(4), pp. 3477-3486.

Chen, Y.-F. and Du, Y.-L., 2009. One-Shot Surface Profile Measurement Using Polarized Phase-Shifting. *Proc. of SPIE*, 7511

Choma, M. A., Hsu, K. and Izatt, J. A., 2005. Swept source optical coherence tomography using an all-fiber 1300-nm ring laser source. *Journal of Biomedical Optics,* 10(4), pp. 1-6

Chu, S. T. and Chaudhuri, S. K., 1995. Finite-Difference Time-Domain Method for Optical Waveguide Analysis, *Progress in Electromagnetics Research*, 11, pp. 255-300.

Chua, Y. H. et al., 2011. Using MTF with fixed-zoning method for automated gated imaging system in turbid medium. *Indian Journal of Geo-Marine Science,* 40(2), pp. 236-241.

Dai, G. M., 1994. Modified Hartmann-Shack Wavefront Sensing and Iterative Wavefront Reconstruction. *SPIE Adaptive Optics in Astronomy,* 2201, p. 562

Dai, G. M., 2008. *Wavefront optics for vision correction*, SPIE Press.

Davidson, B. R. and Barton, J. K., 2010. Application of optical coherence tomography to automated contact lens metrology. *Journal of Biomedical Optics* 15(1), pp. 1-9.

Drexler, W. and Fujimoto, J. G., 2008. *Optical Coherence Tomography: Technology and Applications*, Springer.

Fercher, A. F., Drexler, W., Hitzenberger, C.K., Lasser, T., 2003. Optical Coherence Tomography - principles and applications. *Rep. Prog. Phys.,* 66 (2003), pp. 239–303.

Forest, C. R. et al., 2003. Metrology of thin transparent optics using Shack-Hartmann wavefront sensing. *Optical Engineering,* 43, pp. 742-753.

Fujiwara, H., 2005. *Spectroscopic Ellipsometry Principles and Applications*, Wiley.

Fujiwara, H., Kageyama, S., Yuguchi, T. and Kanie, Y., 2012. Photovoltaic thin-film materials characterized using spectroscopic ellipsometry. *19th International Workshop on Active-Matrix Flatpanel Displays and Devices (AM-FPD),* pp. 281-284.

Fukunaga, K. et al. 2011. Investigating the use of terahertz pulsed time domain reflection imaging for the study of fabric layers of an Egyptian mummy. *Journal of the European Optical Society - Rapid Publications*, 6, pp. 1-4.

Gayen, S. K. et al., 2001. Parotid Gland Tissue Investigated by Picosecond Time-Gated and Optical Spectroscopic Imaging Techniques. *IEEE Journal of Selected Topics in Quantum Electronics,* 7(6), pp. 906-911.

Ghatak, A., 2005. *Optics*, Tata McGraw-Hill Education.

Glassner, A. S., 1989. *An Introduction to Ray Tracing*, Morgan Kaufmann.

Gora, M. et al., 2009. Ultra high-speed swept source OCT imaging of the anterior segment of human eye at 200 kHz with adjustable imaging range. *Optics Express*, 17(17), pp. 14880-14894.

Grimsley, T. J. et al., 2008. Picosecond Ultrasonic Microscopy of Semiconductor Nanostructures, *1st International Symposium on Laser Ultrasonics: Science, Technology and Applications*. 16-18 July 2008, Montreal, Canada, pp. 1-6.

Gui, C., Elwenspoek, M., Tas, N. and Gardenier, J. G. E., 1999. The effect of surface roughness on direct wafer bonding. *Journal of Applied Physics,* 85(10), pp. 7448-7454

Hall, C., Tricard, M. and Dumas, P., 2007. Manufacture and Metrology of 300mm Silicon Wafers with Ultra-Low Thickness Variation. *2007 International Conference of Characterization and Metrology*, 931, pp. 105-110.

Hariharan, P. 2007. *Basics of Interferometry*, Academic Press, Burlington.

Hartmann, J. 1904. Bemerkungen über den Bau und die Justirung von Spektrographen. *Zt. Instrumentenkd.* 20, pp. 47-58.

Hattori, T., 1998. *Ultraclean Surface Processing of Silicon Wafers: Secrects of VLSI Manufacturing*, Springer.

He, D. M. and Seet, G. G. L., 2001. Underwater lidar imaging (UWLI) in 3m tank with highly turbid waters. *The 4th Pacific Rim Conference on Lasers and Electro-Optics, 2001*. 15-19 July 2001. Chiba, Japan, pp. 176-177.

Hermann, B. et al., 2004. Adaptive-optics ultrahigh-resolution optical coherence tomography. *Optics Letters,* 29(18), pp. 2142-2144.

Huang, D. et al., 1991. Optical Coherence Tomography. *Science, New Series,* 254(5035), pp. 1178-81

Huang, Z., Wang, L., He, Z. and Chen, J., 2008. Primary study on ellipsometry of large roughness surface, *Proc. SPIE,* 6723, pp. 1-5.

Innovation, M.-P., 2011. *Coherence-gated Wavefront Sensing in Strongly Scattering Samples* [Online].
Available: http://www.max-planck-innovation.de/share/technology/0105-3295-BC-JK_EN.pdf. [Accessed: 18 October 2012]

J., Y., Rao, X. and Rao, C., 2008. Measurement of Corneal Topography through Hartmann-Shack Wave-front Sensor. *Proc. SPIE*, 7160, pp. 1-9.

Jackson, J. B., 2008. *Terahertz Time-Domain Reflectometry of Multilayered Systems.* PhD Thesis, Univesity of Michigan, United States of America.

Jackson, J. B. et al., 2009. Terahertz pulse imaging for tree-ring analysis: a preliminary study for dendrochronology applications. *IOP Measuring Science and Technology,* 20(7), pp. 1-10.

Jansen, M. J., Haitjema, H. and Shellekens, P. H. J., 2004. Development of a scanning wafer thickness and flatness interferometer. *Proc. SPIE,* 5252**,** pp. 334-345.

Kang, H. H., King, J. F., Patterson, O. D. and Herschbein, S. B., 2010. High Volume and Fast Turnaround Automated Inline TEM Sample Preparation for Manufacturing Process Monitoring. *ISTFA 2010, Proceedings from the 36th International Symposium for Testing and Failure Analysis*, pp. 102-107

Kubby, J. A., 2013. *Adaptive Optics for Biological Imaging*, Taylor and Francis.

Kuria, J. M., Schön, R. and Börret, R., 2012. A Flatbed Scanner Based Wavefront Sensing Unit for Optics Quality Control. *18th World Conference on Nondestructive Testing,* 16-20 April 2012, Durban, South Africa, pp. 1-11.

Kwon, T., Joo, K.-N. and Kim, S.-W., 2007. Optical Coherence Tomography of Silicon Wafers using a Femtosecond Pulse Laser. *Asian Symposium for Precision Engineering and Nanotechnology 2007*, pp. 42-45.

Labaune, J. et al., 2010. Terahertz investigation of Egyptian artifacts. *35th International Conference on Infrared Milimeter and Terahertz Waves (IRMMW-THz) 2010*. 5-10 Sept 2010, Rome, Italy, pp. 1-3.

Lamb, D. C. et al., 2000. Sensitivity Enhancement in Fluorescence Correlation Spectroscopy of Multiple Species Using Time-Gated Detection. *Biophysical Journal*. 79(2), pp. 1129-1138.

Lawman, S. and Liang, H., 2009. Fourier domain optical coherence tomography for high-precision profilometry. *Proc. SPIE*, 7391, pp. 1-12.

Leach, R., 2010. *Fundamental Principles of Engineering Metrology*, William Andrew.

Leahy-Hoppa, M. R. et al., 2010. Ultrafast Laser-Based Spectroscopy and Sensing: Applications in LIBS, CARS, and THz Spectroscopy *Sensors 2010,* 10, pp. 4342-4372.

Leitgeb, R., Hitzenberger, C. K. and Fercher, A. F., 2003. Performance of fourier domain vs. time domain optical coherence tomography. *Optics Express*, 11(8), pp. 889-894.

Li, J. et al., 2007. Combining 5-D Microscopy with 3-D Femtosecond Laser Nanoprocessing. *Conference on Lasers and Electro-Optics (CLEO),* 6-11 May 2007, Baltimore, Maryland, United States of America, pp. 1-2.

Li, X., Zhao, L.P., Fang, Z.P., Asundi, A., Yin, X.M., 2008., Surface Measurement with Shack-Hartmann wavefront sensing technology. *Proc. SPIE*, 7155.

Lin, Z. J. et al., 2009. Time-gated optical imaging to detect positive prostate cancer margins. *Proc. SPIE*, 7161, pp. 1-9.

Liu, X. and Gao, Y., 2001. Surface Roughness Profile Measurement Based On Microscopic Shearing Interferometry. *ASPE Proceedings,* November 10 - 15, 2001, Crystal City, Virginia, United States of America, pp. 1-4.

Maddahi, J. et al., 1979. A new technique for assessing right ventricular ejection fraction using rapid multiple-gated equilibrium cardiac blood pool scintigraphy. Description, validation and findings in chronic coronary artery disease. *Circulation,* 60, pp. 581-589.

Malacara, D., 2007. *Optical Shop Testing, Third Edition*, John Wiley and Sons, Inc.

Matsuda, O. and Wright, O. B., 2004. Laser picosecond acoustics in a two-layer structure with oblique probe light incidence. *Elsevier Ultrasonics,* 42(1-9), pp. 653-656.

Matsuda, O., Wright, O.B., 2002. Laser picosecond acoustics in multilayer structures. *Elsevier Ultrasonics*, 40(1-8)*,* pp. 753-756.

Mueller, E. R., Uehara, Y., Uchikawa, K. 2008. *Putting the Squeeze in Optical Microlithography*, Photonics Spectra December 2008, Laurin Publishing.

Mitchell, A. C., Wall, J.E., Murray, J.G., Morgan, C.G., 2002. Measurement of nanosecond time-resolved fluorescence with a directly gated interline CCD camera. *Journal of Microscopy,* 206(3), pp.233-238.

Mittleman, D. M., Jacobsen, R. H. and Nuss, M. C., 1996. T-Ray Imaging. *IEEE Journal of Selected Topics in Quantum Electronics,* 2(3), pp. 679-692.

Neal, D. R., 2004. Shack-Hartmann sensor engineered for commercial measurement applications. *Proceedings of SPIE,* 5162, pp. 1-15.

Neal, D. R., Copland, J. and Neal, D., 2002. Shack-Hartmann wavefront sensor precision and accuracy. *Proceedings of SPIE*, 4779, pp. 148-160.

Nemoto, K. et al., 2007. Impact of Silicon Surface Roughness on Device Performance and Novel Roughness Measurement Method *2007 IEEE/SEMI Advanced Semiconductor Manufacturing Conference*, 11-12 June 2007, Stresa, Italy, pp. 157-160.

Neuschaefer-Rube, U., Holzapfel, W. and Wirth, F., 2003. Surface measurement applying focusing reflection ellipsometry: configurations and error treatment. *Measurement*, 33 (2)**,** pp. 163-171.

Ogita, Y.-I. et al., 1998. Non-contact Silicon Epilayer and Subsurface Characterization with UV/MM Wave Technique. *ASTM Recombination Lifetime Measurements in Silicon,* 1340, pp. 168-182.

Pearce, J., Choi, H. and Mittleman, D. M., 2005. T-Ray Reflection Computed Tomography. *2005 Conference on Lasers and Electro-Optics (CLEO)*, 14 March 2005, Orlando, Florida, United States of America, pp. 2120-2122.

Peth, C., Kranzusch, S., Mann, K. 2003. Metrologie im extrem-ultravioletten Spektralbereich: Abstrahlcharakteristik laserinduzierter Plasmen bei 13 nm, *Physik Journal 2 (2003)*, 7/8, pp. 1-5

Platt, B. C., Shack, R., 2001. History and Principles of Shack-Hartmann Wavefront Sensing. *Journal of Refractive Surgery*, 17, pp. 573-577.

Podjue, N., Kerr, W. and Turner, K. T., 2010. Inspection of Bonded Interfaces using Scanning Infrared Interferometry. *ECS Transcations 2010,* 33(4), pp. 537-541.

Raymond, T. D., Neal, D. R. and Topa, D. M., 2002. High-speed, non-interferometric nanotopographic characterization of Si wafer surfaces. *Proc. SPIE,* 4809, pp. 208-216.

Sagar, R. 2003. *Together with Physics*, 1st ed. Rachna Sagar Pvt. Ltd.

Sampson, D., 2002. *Introduction to Optical Coherence Tomography (OCT)* [Online]. Available: http://obel.ee.uwa.edu.au/research/oct/introduction-to-oct. [Accessed: 30 August 2011]

Schlick, T., 2010. *Molecular Modeling and Simulation: An Interdisciplinary Guide*, Springer.

Schmitt, J. M., 1999. Optical Coherence Tomography (OCT): A review. *IEEE Journal of Selected Topics in Quantum Electronics,* 5(4), 1205-1215.

Schmitz, T. L., Davies, A. and Evans, C. J., 2003. Silicon Wafer Thickness Variation Measurements using Infrared Interferometry. *2003 Winter Topical Meeting*, 28, pp. 98-103

Schwiegerling, J., 2011. *Description of Zernike Polynomials* [Online]. Available: http://www.visualopticslab.com/OPTI515L/Background/Zernike%20Notes%2017Feb2011.pdf [Accessed: 30 August 2013].

Schwiegerling, J. and Neal, D. R., 2005. *Historical Development of the Shack-Hartmann Wavefront Sensor* [Online]. Available: http://www.lumetrics.com/documents/wavefront/Historical%20Development.pdf [Accessed: 30 August 2013].

Serrels, K. A., Renner, M. K. and Reid, D. T., 2010. Optical coherence tomography for non-destructive investigation of silicon integrated circuits. *Microelectronic Engineering,* 87*,* pp. 1785-1791.

Shaw-McMinn, P. G., *How to Provide High-Resolution Vision: An introductory guide to prescribing iZon lenses* [Online]. Available: http://cms.revoptom.com/index.asp?ArticleType=SiteSpec&Page=osc/105418/lesson.htm [Accessed: 30 August 2013].

Sluzek, A. and Tan, C. S., 2004. Visual Detection of 3D Obstacles Using Gated Images. *8th International Conference on Control, Automation, Robotics and Vision*, 6-9 December 2004 Kunming, China, pp. 92-97.

Southwell, W. H., 1980. Wave-front estimation from wave-front slope measurements. *J. Opt. Soc. Am.,* 70(8), pp. 998-1006.

Steinvall, O. et al., 1999. Gated viewing for target detection and target recognition. *Proc. SPIE*, 3707, pp. 1-17.

Su, R. et al., 2012. Optical coherence tomography for quality assessment of embedded microchannels in alumina ceramic. *Optics Express*, 20(4), pp. 4603-4618.

Tan, C. S., Wang, X., Ng, Y.H., Lim, W.K., Chai, T.Y., 2013. Method for distortion correction of multi-layered surface reconstruction using time-gated wavefront approach. *Journal of European Optical Society,* 8, pp. 1-7.

Teare, S. W. and Restaino, S. R., 2006. *Introduction to Image Stabilization*, SPIE Press.

Thorlabs, 2013. *Shack-Hartmann Wavefront Sensors, 1.3 Megapixel Resolution* [Online]. Available: http://www.thorlabs.com/newgrouppage9.cfm?objectgroup_id=2946. [Accessed: 30 August 2013]

Tien, C.-L., Lyu, Y.-R. and Jyu, S.-S., 2008. Surface flatness of optical thin films evaluated by gray level co-occurrence matrix and entropy. *Applied Surface Science,* 254(15), pp. 4762-4767.

Török, P. and Kao, F.-J., 2003. *Optical Imaging and Microscopy: Techniques and Advanced Systems*, Springer.

Tseng, A. A. and Park, J.-S. 2006., Effects of Surface Roughness and Oxide Layer on Wafer Bonding Strength Using Transmission Laser Bonding Technique. *Thermal and Thermomechanical Phenomena in Electronics Systems, 2006. ITHERM '06*, 30 May 2006-2 June 2006, San Diego, United States of America, pp. 1-9.

Tuohy, S. and Podoleanu, A. G., 2010. Depth-resolved wavefront aberrations using a coherence-gated Shack-Hartmann wavefront sensor. *Optics Express,* 18(4), pp. 3458-3476.

Wang, J. et al., 2012. Measuring aberrations in the rat brain by coherence-gated wavefront sensing using a Linnik interferometer *Biomedical Optics Express,* 3(10), pp. 2510-2425.

Wang, J. and Podoleanu, A. G., 2011. Time-domain coherence-gated Shack-Hartmann wavefront sensor. *Proc. SPIE*, 8091, pp.1-6.

Williams, D. B. and Carter, W. C., 2009. *Transmission Electron Microscopy: A Textbook for Materials Science, Second Edition*.

Withayachumnankul, W. et al., 2007. T-Ray Sensing and Imaging. *Proceedings of the IEEE*, 95(8), pp. 1528 - 1558

Wright, O. B., 1995. Laser Picosecond Acoustics in Double-Layer Transparent Films. *Optics Letters,* 20(6), pp. 632-634

Wright, O. B. and Hyoguchi, T., 1991. Ultrafast vibration and laser acoustics in thin transparent films. *Optics Letters*, 16(19), pp. 1529-1531.

Xu, S., Zhang, S. and Tang, S. 2011, Design and Implementation of the Laser Range-gating Imaging Synchronization Control System. *2011 International Conference on Electronics and Optoelectronics (ICEOE 2011)*, 29-31 July 2011, Dalian, China, pp. 237-243.

Yang, J., Zhou, Y., Fan, S. and Wang, X., 2011. Picosecond timing synchronization control signal for 3D range-gated imaging. *Proc. of SPIE*, 8192.

Yanoff, M. and Duker, J. S., 2009. *Ophthalmology*, Elsevier Health Sciences, Maryland Heights.

Yaqoob, Z., Wu, J. and Yang, C., 2005. Spectral domain optical coherence tomography: a better OCT imaging strategy. *BioTechniques,* 39(6), pp. 6-13.

Yurtsever, G. and Baets, R., 2008. Towards Integrated Optical Coherence Tomography System on Silicon on Insulator. *Proceedings Symposium IEEE/LEOS Benelux Chapter, 2008,* 27-28 November 2008, Twente, Netherlands, pp. 163-166.

Zernike, F. 1934. Beugungstheorie des Schneidenverfahrens und seiner verbesserten Form, der Phasenkontrastmethode, *Physica 1*, pp. 689-704.

Zevallos, M. E. et al., 1999. Picosecond Electronic Time-Gated Imaging of Bones in Tissues. *IEEE Journal of Selected Topics in Quantum Electronics,* 5(4), pp. 447-451.

Zorich, R. 1991. *Handbook of Quality Integrated Circuit Manufacturing*, 1st ed. San Diego: Academic Press.

APPENDICES

LIST OF PUBLICATIONS

1. Tan, C.S., Wang, X., Ng, Y.H., Lim, W.K., Chai, T.Y., 2013. Method for distortion correction of multi-layered surface reconstruction using time-gated wavefront approach, *Journal of European Optical Society*, 8, pp. 1-7.

PROGRAM CODE

DistortSurface.m

```
% Reconstruction of distorted surface from one material which
contains
% two interfaces.
% Written by Ng Yong Han.
%
% References:
% 1.) Dai, G. M. 2008. Wavefront optics for vision correction,
SPIE.
% 2.) Glassner, A. S. 1989. An Introduction to Ray Tracing,
Morgan Kaufmann.

clearvars -except count1

tempZernike;                                      % forms the list of
Zernike polynomials, up to 30 th.

width = 3;
width_s = 1;                                      % sampling width.
[X Y] = meshgrid(-1.2:1/width:1.2);
zernike_max_coeff = 30;                           % Maximum Zernike
coefficients.

d = 1e-3;                                         % distance between
two interfaces.
n1 = 1;
n2 = 1.55;                                        % material
refractive index.
W3_X = zeros(size(X,1),size(X,1));
W3_Y = zeros(size(X,1),size(X,1));
W3_Z = zeros(size(X,1),size(X,1));

sf1 = '0.000001*sqrt(6)*(x^2 - y^2)';             % Top surface is
0.0000001*Z5.
sf2 = '0.000001*sqrt(6)*(x^2 - y^2)';             % Subsurface is
0.0000001*Z5.

%-----------------------------------------------------------------
--------------------------------------------
% Raytracing and displaying the picture of the subsurface
%-----------------------------------------------------------------
--------------------------------------------
strDisp = sprintf('d = %d, n2 = %f \n', d, n2);
strDisp1 = sprintf('Top Surface: %s \nBottom Surface: %s \n',
sf1, sf2);
strDisp3 = sprintf('Number of Zernike Coefficients: %d\n',
zernike_max_coeff);
disp(strDisp);
disp(strDisp1);
```

```
for i = 1:size(X,1)*size(X,1)
% Raytrace each point on two surfaces.
    tempExitCoordinate = rayTrace3D(X(i),Y(i), d,n1, n2, sf1, sf2
);
    W3_X(i) = tempExitCoordinate(1);
    W3_Y(i) = tempExitCoordinate(2);
    W3_Z(i) = tempExitCoordinate(3);
end

[W3_X_tmp W3_Y_tmp W3_Z_tmp] = prepareSurfaceData( W3_X, W3_Y,
W3_Z );                  % Perform fitting afterwards to form the
entire subsurface.
fitResult1 = fit([W3_X_tmp W3_Y_tmp], W3_Z_tmp, 'cubicinterp');
% at Cubic interpolation.

h1 = figure;
plot( fitResult1, [W3_X_tmp, W3_Y_tmp], W3_Z_tmp );
title(sprintf('Top surface = %s,\nBottom surface = %s\nn2 = %f, d
= %d', sf1,sf2,n2,d));
grid on;

[X1 Y1] = meshgrid(-1:1/width:1);
Z1 = fitResult1(X1, Y1);

for i = 1:size(Z1,1)*size(Z1,2)

    if isnan(Z1(i))
        Z1(i) = 0;
    end

end

dispStr2 = sprintf('file%d.png', count1);
print(h1, '-dbmp', dispStr2);
saveas(h1, dispStr2);
%-----------------------------------------------------------------
--------------------------------------------


%-----------------------------------------------------------------
--------------------------------------------
% Zernike Decomposition of the surface.
% 1. Differentiate surface.
% 2. Get list of slopes and then put into the
ZernikeDecomposition
%    function.
% 3. Plot the chart.
%-----------------------------------------------------------------
--------------------------------------------
S_Z1 = sqrWfToLinearSlopes(Z1);
Z_C1 = ZernikeDecomposition(S_Z1, zernike_max_coeff);
Z_C1T = Z_C1';

h2 = figure;
% h1_b = subplot(2,1,2);
```

```
bar(Z_C1);
set(gca,'XTick',1:1:zernike_max_coeff);
set(gca,'XLim',[1 zernike_max_coeff]);
xlabel('Zernike Number');
ylabel('Magnitude');
dispStr3 = sprintf('chart%d.png', count1);
saveas(h2, dispStr3);

count1 = count1 + 1;
%-----------------------------------------------------------------
--------------------------------------------
```

RayTrace3D.m

```
% Point to point raytracing on two surfaces.
% Written by Ng Yong Han.
% Reference: Glassner, A. S. 1989. An Introduction to Ray
Tracing, Morgan Kaufmann.

function [W3] = rayTrace3D(x_input, y_input, d, n1, n2,
surface1_input, surface2_input)

syms x y x1 y1 z1 surface1 surface2 surface2solve surface1solve
lambda1 lambda2;

i0 = [0, 0, -1];
xi = x_input;
yi = y_input;

surface1 = sym(surface1_input);
surface2 = sym(surface2_input);
surface1 = surface1 + d;

A = [xi, yi, subs(surface1, [x y], [xi yi])];

delS1delX = diff(surface1, x);
delS1delY = diff(surface1, y);
N0 = [subs(delS1delX, [x y], [A(1) A(2)]), subs(delS1delY, [x y],
[A(1) A(2)]) , -1];

% reflection and transmission at surface 1
% ---------------------------------------------------------------
-----------
r0 = reflect1(i0, -N0);
t0 = refract(i0, N0, n1, n2);

x1 = A(1) + lambda1*t0(1);
y1 = A(2) + lambda1*t0(2);
z1 = A(3) + lambda1*t0(3);

% surface 2 intersection
% ---------------------------------------------------------------
-----------
```

```
surface2solve = subs(surface2, [x y], [x1 y1]);
surface2solve = z1 - surface2solve;
l1 = solve(surface2solve);
[l1_n l1_i] = min(abs(double(l1)));

B = [subs(x1, lambda1, double(l1(l1_i))), subs(y1, lambda1,
double(l1(l1_i))), subs(z1, lambda1, double(l1(l1_i))) ];
% ---------------------------------------------------------------
-----------

% surface 2 reflection
% ---------------------------------------------------------------
-----------
delS2delX = diff(surface2, x);
delS2delY = diff(surface2, y);
N1 = [subs(delS2delX, [x y], [B(1) B(2)]), subs(delS2delY, [x y],
[B(1) B(2)]) , -1];

r1 = reflect1(t0, -N1);

x2 = B(1) + lambda2*r1(1);
y2 = B(2) + lambda2*r1(2);
z2 = B(3) + lambda2*r1(3);

% surface 1 intersection again after reflection from surface 2
% ---------------------------------------------------------------
-----------
surface1solve = subs(surface1, [x y], [x2 y2]);
surface1solve = z2 - surface1solve;
l2 = solve(surface1solve);
[l2_n l2_i] = min(abs(double(l2)));

C = [subs(x2, lambda2, double(l2(l2_i))), subs(y2, lambda2,
double(l2(l2_i))), subs(z2, lambda2, double(l2(l2_i))) ];

% surface 2 refraction
% ---------------------------------------------------------------
-----------
N2 = [subs(delS1delX, [x y], [C(1) C(2)]), subs(delS1delY, [x y],
[C(1) C(2)]) , -1];

t1 = refract(r1, N2, n2, n1);

W3 = C;
```

reflect1.m

```
% Reflection algorithm.
% Reference: Glassner, A. S. 1989. An Introduction to Ray
Tracing, Morgan Kaufmann.

function [r0] = reflect1(incident, normal)

incident = incident/norm(incident);                  % normalized
incident
normal = normal/norm(normal);                        % normalized
surface normal

r0 = incident - 2*(dot(incident,normal)*normal);     % reflection
vector from surface 1;
```

refract.m

```
% Refraction algorithm.
% Reference: Glassner, A. S. 1989. An Introduction to Ray
Tracing, Morgan Kaufmann.

function [transmitted] = refract(incident, normal, n1, n2)

incident = incident/norm(incident);

normal = normal/norm(normal);

cosTheta_i = -dot(incident, normal);

sin2Theta_t = ((n1/n2)^2)*(1-(cosTheta_i^2));

transmitted = (n1/n2)*incident + ((n1/n2)*cosTheta_i - sqrt(1-
sin2Theta_t))*normal;

transmitted = transmitted/norm(transmitted);
```

sqrWfToLinearSlopes.m

```
% Convert a square wavefront matrix into an mx1 slope array.
% Example: [(dZ_dx)_1, (dZ_dx)_2,(dZ_dx)_3,... ,(dZ_dx)_N,
(dZ_dy)_1, (dZ_dy)_2,(dZ_dy)_3,... ,(dZ_dy)_N]'

function [S_Z] = sqrWfToLinearSlopes(Z_Input)

width = (size(Z_Input, 1) - 1)/2;
[dZ_dx dZ_dy] = gradient(Z_Input, 1/(width*2), 1/(width*2));
dZ_dx = reshape(dZ_dx, size(Z_Input,1)^2, 1);
dZ_dy = reshape(dZ_dy, size(Z_Input,1)^2, 1);

dZ = [dZ_dx; dZ_dy];
S_Z = dZ;
```

ZernikeDecomposition.m

```
% Zernike Decomposition Algorithm (up to 30 modes)
% Dai G.M. Wavefront Optics for Vision Correction
% pg. 114
%
% function z_c = ZernikeDecomposition(S_Z, modes)
%
% z_c - zernike coefficients.
%
% S_Z - an array of slopes, example: [ dW_dx1 dW_dx2 ... dW_dxN
dW_dy1
% dW_dy2 ... dW_dyN]'
%
% modes - number of modes, up to 30.
%

function z_c = ZernikeDecomposition(S_Z, modes)

array_width = sqrt(size(S_Z,1)/2);
width = (array_width - 1)/2;
xx = -1:1/(width):1;
[X Y] = meshgrid(xx);

max_modes = modes;
E = zeros((size(xx,2)^2)*2,1);

Z_modes = { @(X,Y) 2.*Y;                                    %
mode 1
            @(X,Y) 2.*X;                                    %
mode 2
            @(X,Y) sqrt(6).*2.*X.*Y;                        %
mode 3
            @(X,Y) sqrt(3).*(2.*X.^2 + 2.*Y.^2 - 1);        %
mode 4
            @(X,Y) sqrt(6).*(X.^2 - Y.^2);                  %
mode 5
```

```
            @(X,Y) sqrt(8).*(3.*(X.^2).*Y - (Y.^3));          %
mode 6
            @(X,Y) sqrt(8).*(3.*(X.^2).*Y + 3.*Y.^3 - 2.*Y); %
mode 7
            @(X,Y) sqrt(8).*(3.*X.^3 + 3.*X.*Y.^2 - 2.*X);   %
mode 8
            @(X,Y) sqrt(8).*(X.^3 - 3.*X.*(Y.^2));            %
mode 9
            @(X,Y) sqrt(10).*(4.*(X.^3).*Y - 4.*(X.*Y.^3));  %
mode 10
            @(X,Y) sqrt(10).*(8.*(X.^3).*Y + 8.*X.*(Y.^3) -
6.*X.*Y);    % mode 11
            @(X,Y) sqrt(5).*(6.*X.^4 + 12.*(X.^2).*(Y.^2) +
6.*Y.^4 - 6.*X.^2 - 6.*Y.^2 + 1); % mode 12
            @(X,Y) sqrt(10).*(4.*X.^4 - 4.*Y.^4 - 3.*X.^2 +
3.*Y.^2);    % mode 13
            @(X,Y) sqrt(10).*(X.^4 - 6.*(X.^2).*(Y.^2) + Y.^4);
% mode 14
            @(X,Y) sqrt(12).*(5.*(X.^4).*Y - 10.*(X.^2).*(Y.^3) +
Y.^5); % mode 15
            @(X,Y) sqrt(12).*(15.*(X.^4).*Y + 10.*(X.^2).*(Y.^3)
- 5.*(Y.^5) - 12.*(X.^2).*Y + 4.*(Y.^3)); % mode 16
            @(X,Y) sqrt(12).*(10.*(X.^4).*Y + 20.*(X.^2).*(Y.^3)
+ 10.*(Y.^5) - 12.*(X.^2).*Y - 12.*(Y.^3) + 3.*Y); % mode 17
            @(X,Y) sqrt(12).*(10.*(X.^5) + 20.*(X.^3).*(Y.^2) +
10.*X.*(Y.^4) - 12.*X.^3 - 12.*X.*Y.^2 + 3.*X) % mode 18
            @(X,Y) sqrt(12).*(5.*(X.^5) - 10.*(X.^3).*(Y.^2) -
15.*X.*(Y.^4) - 4.*X.^3 + 12.*X.*Y.^2) % mode 19
            @(X,Y) sqrt(12).*(X.^5 - 10.*(X.^3).*(Y.^2) +
5.*X.*Y.^4);                    % mode 20
            @(X,Y) sqrt(14).*(6.*(X.^5).*Y - 20.*(X.^3).*(Y.^3) +
6.*X.*Y.^5);            % mode 21
            @(X,Y) sqrt(14).*(24.*(X.^5).*Y - 24.*X.*Y.^5 -
20.*(X.^3).*Y + 20.*X.*Y.^3); % mode 22
            @(X,Y) sqrt(14).*(30.*(X.^5).*Y + 60.*(X.^3).*(Y.^3)
+ 30.*X.*Y.^5 - 40.*(X.^3).*Y - 40.*X.*Y.^3 + 12.*X.*Y) % mode 23
            @(X,Y) sqrt(7).*(20.*(X.^6) + 60.*(X.^4).*(Y.^2) +
60.*(X.^2).*(Y.^4) + 20.*(Y.^6) - 30.*X.^4 - 60.*(X.^2).*(Y.^2) -
30.*Y.^4 + 12.*X.^2 + 12.*Y.^2 - 1); % mode 24
            @(X,Y) sqrt(14).*(15.*(X.^6) + 15.*(X.^4).*(Y.^2) -
15.*(X.^2).*(Y.^4) - 15.*(Y.^6) - 20.*Y.^4 + 6.*(X.^2) -
6.*(Y.^2)); % mode 25
            @(X,Y) sqrt(14).*(6.*X.^6 - 30.*(X.^4).*(Y.^2) -
30.*(X.^2).*(Y.^4) + 6.*Y.^6 - 5.*X.^4 + 30.*(X.^2).*(Y.^2) -
5.*Y.^4); % mode 26
            @(X,Y) sqrt(14).*(X.^6 - 15.*(X.^4).*(Y.^2) +
15.*(X.^2).*(Y.^4) - Y.^6);     % mode 27
            @(X,Y) 4.*(7.*(X.^6).*Y - 35.*(X.^4).*(Y.^3) +
21.*(X.^2).*(Y.^5) - Y.^7);     % mode 28
            @(X,Y) 4.*(35.*(X.^6).*Y - 35.*(X.^4).*(Y.^3) -
63.*(X.^2).*(Y.^5) + 7.*Y.^7 - 30.*(X.^4).*Y + 60.*(X.^2).*(Y.^3)
- 6.*Y.^5); %mode 29
            @(X,Y) 4.*(63.*(X.^6).*Y + 105.*(X.^4).*(Y.^3) +
21.*(X.^2).*(Y.^5) - 21.*Y.^7 - 90.*(X.^4).*Y -
60.*(X.^2).*(Y.^3) + 30.*Y.^5 + 30.*(X.^2).*Y - 10.*Y.^3); % mode
30
```

```
         };

        for n = 1:1:max_modes

            [dZ_dx dZ_dy] = gradient(Z_modes{n}(X,Y),
1/(width*2), 1/(width*2));
            dZ_dx = reshape(dZ_dx, size(X,1)^2, 1);
            dZ_dy = reshape(dZ_dy, size(X,1)^2, 1);
            dZ = [dZ_dx; dZ_dy];
            E = [E dZ];
        end

        E(:,1) = []; % remove first dummy column

        % Singular value decomposition on E matrix due to rank
deficiency:
        [U, D, V] = svd(E, 0);
        D = pinv(D);
        z_c = V*D*U'*S_Z;

        clearvars -except E S_Z z_c;
```